Signatures of the Absence of Thermalisation in Electronic Systems

by

George McArdle

A thesis submitted to the
University of Birmingham
for the degree of
DOCTOR OF PHILOSOPHY

School of Physics and Astronomy
College of Engineering and Physical Sciences
University of Birmingham
July 28, 2023

UNIVERSITY OF
BIRMINGHAM

University of Birmingham Research Archive

e-theses repository

This unpublished thesis/dissertation is copyright of the author and/or third parties. The intellectual property rights of the author or third parties in respect of this work are as defined by The Copyright Designs and Patents Act 1988 or as modified by any successor legislation.

Any use made of information contained in this thesis/dissertation must be in accordance with that legislation and must be properly acknowledged. Further distribution or reproduction in any format is prohibited without the permission of the copyright holder.

ABSTRACT

Many-body localisation is a phenomenon in interacting, disordered systems and is a robust way of avoiding thermalisation. It has a number of interesting physical properties including giving rise to a finite-temperature insulating state as well as logarithmic entanglement growth with time. Although experimental progress has been made in systems of ultracold atoms due to isolation from the environment being possible, there have been limited developments in solid-state systems where the presence of phonons restores transport and destroys localisation. This work focuses on identifying signatures of (i) electron-phonon decoupling in suspended thin films and (ii) the absence of thermalisation in quantum dots. Both tasks will allow for experimental progress in identifying electronic systems that are suitable for trying to observe many-body localisation.

DEDICATION

For Mum and Dad.

ACKNOWLEDGEMENTS

I would like to thank a number of people for their support during this PhD. First, I thank Igor Lerner for supervising me for the last four years, without whom this would not have been possible. I additionally thank Igor Yurkevich and Rose Davies of Aston University, whose support during the second half of my PhD has proven invaluable.

I would also like to thank all my friends and colleagues that I have had the pleasure of spending time with - special mention must go to James Pallister, David Reid, Lewis Madden, Tom Young, Kerr Maxwell, and Chris Oliver.

Lastly and most importantly I would like to thank my family and girlfriend for all their support. To my parents and Harry, Lucy, Scruffy, Ruby, and Barney I thank you for continued encouragement over, not just the last 4 years but many before that too, I would not be at this point without you all. Grace, I would like to thank you for making my life significantly better over the last year and helping me through the end of this PhD.

CONTENTS

LIST OF FIGURES

CHAPTER 1

INTRODUCTION

Quantum transport and mesoscopics, the latter of which lies between the more familiar areas of microscopic and macroscopic physics, both contain many interesting physical transport phenomena such as the integer and fractional quantum Hall effects (see for example [1, 2]), universal conductance fluctuations [3–5], the zero bias anomaly [6, 7] and the related Coulomb blockade [8–10], and localisation [11–17]. The Coulomb blockade and localisation will be discussed in this thesis. The understanding of quantum transport in mesoscopic devices has led to developments in a variety of applications, most notably transistors [18, 19] which are used in most modern technologies. This particular work focuses on many-body localisation (MBL), where an interacting system can fail to thermalise even at a finite temperature [20], leading to the vanishing of transport as well as many other properties that are unique to this state (see reviews [15–17]). MBL is of interest for various reasons, from studying fundamental physics and the way that systems thermalise (which is true in most instances), to applications in quantum computers as they retain details of the initial state, so can be used to overcome problems of decoherence and the loss of information due to noise (see for example [21] and the references therein). Despite the significant theoretical interest in MBL, the experimental progress has had mixed success. In particular, the observation in disordered electronic systems, where MBL was initially predicted [20, 22], has been difficult to achieve due to

the presence of phonons which lead to thermalisation with the lattice. In order to assist the experimental developments, this work explores the conditions for observing MBL in solid-state systems, namely the electron-phonon decoupling requirement alongside other signatures of the absence of thermalisation. Although the presence of these signatures is not a guarantee of MBL, which has a number of other properties associated with it, they are still important for identifying systems where MBL may be observed experimentally.

1.1 Thesis Overview

This thesis consists of two main research topics, linked by the aim of making progress towards the experimental observation of MBL in electronic systems. Before looking at these in detail however, a background in both mesoscopics and some of the associated experiments and transport phenomena will be discussed in this chapter, laying the foundations for a more in depth discussion of Anderson (single-particle) localisation and many-body localisation in Chapter 2. Here, consideration will be given to both theoretical and experimental aspects and the limitations for observing MBL in electronic systems will be made clear, most notably the coupling to the lattice. This problem will be addressed following the introduction of the theoretical framework of the Keldysh formalism in Chapter 3. This method is particularly well-suited for non-equilibrium physics, of which MBL is an example. Chapter 4 applies the techniques from Chapter 3 to address the requirement of electron-phonon decoupling in solid-state systems. First, the background to the electron-phonon interaction will be presented and following this, the signatures of decoupling will be identified and further discussed in the manuscript *Electron-Phonon Decoupling in Two Dimensions* [23]. In this work, it will be emphasised that should such a decoupling be observed it is not a signature of MBL itself, merely a requirement for it and other methods of identifying MBL should be found. Quantum dots present a viable system for initially studying these signatures, as they undergo a localisation-delocalisation transition in Fock space [24], similar to that which occurs in MBL systems. Therefore, in Chapter 5, the

effect of the absence of thermalisation in a dot asymmetrically coupled to the leads will be explored in the manuscript *Coulomb staircase in an asymmetrically coupled quantum dot* [25] after the background on the Coulomb blockade regime and the concept of localisation in quantum dots has been provided. A similar setup for a dot symmetrically coupled to the leads will be explored in Chapter 6, where the manuscript *Coulomb blockade in a non-thermalized quantum dot* [26] is included. In this work a clear signature of the absence of thermalisation in the differential conductance is identified. After this, possible directions of future research will be discussed with an emphasis on calculating the electronic noise and higher moments of current fluctuations. These can be used as a signature of MBL [27] because they are expected to diverge as the localisation-delocalisation transition is approached. Finally, conclusions will be drawn in Chapter 7.

1.2 Mesoscopics and Transport Regimes

As briefly outlined in the introduction to this thesis, mesoscopic systems exhibit a multitude of different transport phenomena. One of the primary reasons for this is the importance of phase coherence in these systems. To characterise this in a system, there exists a length scale known as the phase coherence length, L_φ, which is the length scale over which the motion of electrons stays coherent. In mesoscopic systems this length is comparable to or greater than the system size, $L \lesssim L_\varphi$, so that coherence is important across the system and that interference effects play a key role [14, 18, 28, 29]. Such a scenario arises in small conductors and semiconductors which can have a size of the order of tens of nanometres up to microns [18, 29–31]. This is in contrast to classical systems which have much larger system sizes, so that the electrons decohere across the sample and interference effects are therefore no longer important. It is in this way that the phase coherence length can determine the dimensionality of a mesoscopic system.

In addition to the size of the system and the phase coherence length, there are a number of other length scales involved and it is the interplay between these which determines

the transport properties. First, there is the de Broglie wavelength of the electrons, λ, although it is the Fermi wavelength, $\lambda_{\mathrm{F}} = 2\pi/k_{\mathrm{F}}$ (k_{F} being the Fermi wavenumber), that is often the relevant quantity as the electrons involved in transport are those near the Fermi surface. This length determines whether the wave nature of the electrons is relevant and is typically a microscopic scale of the order of nanometers [18, 29, 31]. An important length scale when discussing transport in mesoscopic systems is the mean free path, $l = v_{\mathrm{F}}\tau$, where v_{F} is the Fermi velocity and τ is the elastic scattering time. This is the typical distance before an electron scatters elastically, for example from an impurity in the sample, and hence it is important in determining whether the transport across a regime is ballistic or diffusive. In a similar manner to how the mean free path is related to the elastic scattering time, the phase coherence length can be related to a timescale. This time is the phase-breaking time, τ_φ, and is the time between scattering events that destroy coherence[1]. There are a variety of processes that can destroy phase coherence including the scattering of electrons off dynamical impurities (for example magnetic impurities) [32], electron-electron interactions [33], and temperature fluctuations, with the latter having a dependence $\tau_\varphi \sim T^{-p}$ with $p > 0$ [14].

The timescale, τ_φ, is not related to the elastic scattering time, τ, as elastic scattering events do not change the phase relationship between different electrons. Therefore, comparing the two timescales can give insight into the transport properties of the system. If $\tau \gtrsim \tau_\varphi$, then across a phase coherent region the motion is ballistic and $L_\varphi = v_{\mathrm{F}}\tau_\varphi$. On the other hand, if $\tau_\varphi \gg \tau$, then there are many scattering events within a phase coherent region and so the motion is diffusive across the region, leading to $L_\varphi^2 = D\tau_\varphi$, with the diffusion constant $D = v_{\mathrm{F}}^2\tau/d$, where d is the dimensionality of the system. This regime is of particular importance in this work due to the presence of disorder, necessary for localisation, which results in a small mean free path, so that the motion is typically diffusive. The final length scale that is relevant for this work is the localisation length and this will be introduced in more detail in the coming sections.

[1]This time is closely related to the inelastic scattering time although there can be some differences when low-energy scattering processes become important [30].

1.3 Two-Dimensional Electron Gas

The interest in mesoscopic physics increased drastically as experimental methods advanced, meaning that these effects could be studied. One of the major platforms for studying mesoscopic physics is a two-dimensional electron gas (2DEG) - see [29, 34] for reviews. This is typically formed using a semiconductor heterojunction where semiconductors with different band gaps and Fermi energies are brought together, forming an electron gas at the interface. This occurs as electrons flow from the material with the higher Femi energy to that with the lower until equilibrium is reached when the Fermi levels are equal. This flow of electrons leaves behind positively charged ions, establishing an electric field which causes the bands to bend in both materials and a potential well is formed at the interface - this is the 2DEG - see Fig. 1.1.

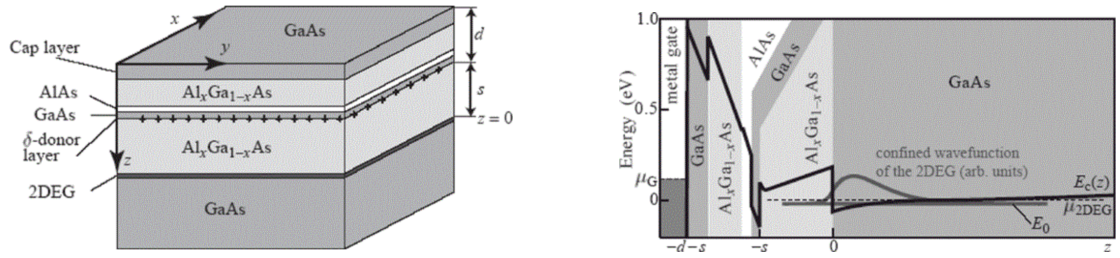

(a) **(b)**

Figure 1.1: The two-dimensional electron gas (2DEG). **(a)**: The semiconductor heterostructure made using GaAs and AlGaAs. **(b)**: The bending of the bands at the interface between the two semiconductors. The 2DEG sits in the well that is formed at the interface, as shown by the confined wave function. Figure taken from [31].

One of the most common ways to form a 2DEG structure is to build it layer-by-layer using molecular-beam epitaxy (MBE) with the two semiconductors being GaAs and AlGaAs due to the ability to form a 2DEG that is clean (has a large mean free path) and has a high mobility [35], though disordered samples can also be made. The 2DEG can be manipulated further using a variety of gate voltages which are applied by patterning gold wires onto the sample in the desired configuration, allowing alterations to the electron density and even the dimensionality of the sample. This allows the formation of quantum wires, quantum point contacts (1d), and quantum dots (0d) [36–38]. This versatility and

access to many different regimes makes a 2DEG extremely useful for studying mesoscopic physics in solid-state systems.

1.4 Transport in a Clean Metal

Transport properties of a mesoscopic system are often of interest theoretically and experimentally (see [29] for a review) and therefore a very common quantity to deal with is the conductance, G of the system, which relates the current, I, to an applied bias, V. This is done either through $G = I/V$, typically used in a linear regime, or the differential conductance $G = \mathrm{d}I/\mathrm{d}V$ in the nonlinear regime. The conductance depends on the dimensions of the system,

$$G = \sigma \frac{A}{L} \implies G \approx \sigma L^{d-2}, \tag{1.1}$$

where A is the cross-sectional area, L is the length of the sample, d is the dimensionality and σ is the conductivity. The conductivity can often be a more useful quantity as it does not depend on the dimensions of the sample, though both the conductivity and conductance are measured in transport experiments. The simplest model of the conductivity is the Drude model, which treats the electrons of mass m and charge e as an ideal gas with electron density n. This leads to

$$\sigma_0 = \frac{ne^2\tau}{m}, \tag{1.2}$$

where τ will depend on the amount of disorder in the system. This is a reasonable model for clean, macroscopic metals.

1.4.1 Fermi Liquid Theory

A more accurate model for describing a metal is Fermi liquid theory [28, 39, 40], which uses quasiparticles (electron-hole pairs) to describe the system. This model acknowledges the electrons as fermions that obey Fermi-Dirac statistics and therefore the excitations (the quasiparticles) have an energy, ε, and momentum, $\mathbf{p}$, that should be measured with

respect to the Fermi surface. The 'electron'-like excitation has an energy

$$\xi = \varepsilon - \varepsilon_{\mathrm{F}} \approx v_{\mathrm{F}}(p - p_{\mathrm{F}}), \tag{1.3}$$

where $\varepsilon_{\mathrm{F}}, v_{\mathrm{F}}, p_{\mathrm{F}}$ are the Fermi energy, velocity and momentum respectively and $p = |\mathbf{p}|$. In the approximate equality, the energy has been linearised around the Fermi surface, which is valid for small quasiparticle energies. This region of small quasiparticle energies is in fact the region of validity of Fermi liquid theory, as the quasiparticles are only well-defined if their width (inverse of their lifetime) is significantly smaller than their energy, $\gamma \ll \xi$, with [28, 39, 40]

$$\gamma \approx \frac{\xi^2}{\varepsilon_{\mathrm{F}}}. \tag{1.4}$$

Therefore, if the system is in equilibrium but has a finite temperature, then $\xi \sim T$ and the low quasiparticle energy corresponds to low temperatures, $T \ll \varepsilon_{\mathrm{F}}$. This framework is a relatively simple way of incorporating electron-electron interactions into the model of a metal and its consequences of excitations being located near the Fermi surface can be used in many instances, including in quantum field theory (QFT) - see Chapter 3. QFT is a powerful formalism that allows for the incorporation of interactions and disorder when calculating physical properties, for example the conductance.

1.4.2 Disorder

The result for the conductance in Eq. (1.1) is for a clean, macroscopic metal. The amount of disorder in a system is characterised by the parameter $k_{\mathrm{F}}l$ and in a clean metal $k_{\mathrm{F}}l \gg 1$. As the amount of disorder is increased, the mean free path is made shorter, reducing this parameter. When it becomes comparable to one, the mean free path is comparable to the Fermi wavelength of the electrons. At this point, the electrons can no longer be treated as classical particles and the quantum nature of them must be included. This is known as the Ioffe-Regel criterion [14, 41] and in the case of transport it represents the point at which Drude conductivity breaks down and the effects of localisation become important.

In the next chapter, the strongly disordered regime ($k_{\mathrm{F}}l \ll 1$) will be considered through a discussion of Anderson localisation, however before that, it is worth noting that even in the case of a good metal there are still quantum corrections to the conductivity in the presence of weak disorder.

1.5 Weak Localisation

The presence of disorder in the system causes electrons to scatter and can lead to diffusive motion across a sample. Additionally, if the phase coherence length is larger than the mean free path, then the transport is diffusive and electrons can scatter multiple times across a phase coherent region and therefore interfere with each other [14, 28, 42]. To see the effect this has on the conductivity across a phase-coherent region, consider an electron going from x_1 to x_2. The probability, P, of such a motion is given by the sum over paths between the two points with amplitudes, $A_i = |A_i|\mathrm{e}^{iS_i}$,

$$P(x_1 \to x_2) = \Big| \sum_i A_i \Big|^2 = \sum_i |A_i|^2 + \sum_{i \neq j} |A_i||A_j|\mathrm{e}^{i(S_i - S_j)}, \tag{1.5}$$

where S_i is the action of path i. The final term above has its origins in quantum mechanics as it represents the interference between different paths. Generally, the difference in length between two paths is large enough that they have different phases. Therefore, when the sum over all paths is performed, this interference term averages to zero due to its oscillatory nature. However, paths that return to the same point and are time-reversible (i.e. $i = j$) create a loop and cannot be neglected in the same way. This is because going along the loop forwards and backwards gives the same phase, so the paths are coherent and the interference term now contributes. Through the use of Eq. (1.5), it can be seen that the return probability is twice that of moving to a different point. Therefore, the electron is less likely to diffuse away than the classical case and so the conductivity drops. The correction to the conductivity due to this coherent backscattering is determined by the probability of having trajectories where the electrons return to the same point and

can be calculated more rigorously using QFT[2], though here a simple argument is outlined that produces the correct behaviour [14, 28, 42].

As an electron has a linear spatial extent of $\lambda \approx \lambda_{\mathrm{F}}$, the cross-sectional area of a path in d-dimensions is $\sim \lambda_{\mathrm{F}}^{d-1}$. The infinitesimal length of a path is then given by $v_{\mathrm{F}}\mathrm{d}t$, so that the volume element of a single path is $v_{\mathrm{F}}\lambda_{\mathrm{F}}^{d-1}\mathrm{d}t$. After a time t the total volume available to the electron diffusing through the system with diffusion constant, D, is $\sim (Dt)^{d/2}$, so the probability of returning in a time frame t to $t + \mathrm{d}t$ is $\sim v_{\mathrm{F}}\lambda_{\mathrm{F}}^{d-1}\mathrm{d}t/(Dt)^{d/2}$. This gives the correction to the conductivity

$$\frac{\sigma - \sigma_0}{\sigma_0} = \frac{\Delta\sigma}{\sigma_0} \sim -\int_{\tau}^{\tau_\varphi} \frac{v_{\mathrm{F}}\lambda_{\mathrm{F}}^{d-1}\mathrm{d}t}{(Dt)^{d/2}}. \tag{1.6}$$

The integral goes from τ as diffusion occurs for $t > \tau$ to τ_φ as this is where the breakdown of phase coherence occurs. The integration in Eq. (1.6) can then be performed for $d = 1, 2, 3$ and after expressing the times in terms of the relevant length scales, the correction to the conductivity is given by

$$\frac{\Delta\sigma}{\sigma_0} \sim \begin{cases} -\left(\frac{\lambda_{\mathrm{F}}}{l}\right)^2 + \frac{\lambda_{\mathrm{F}}^2}{lL_\varphi}, & d = 3, \\ -\frac{\lambda_{\mathrm{F}}}{l}\ln\left(\frac{L_\varphi}{l}\right), & d = 2, \\ -\left(\frac{L_\varphi}{l} - 1\right), & d = 1. \end{cases} \tag{1.7}$$

In the 3d case, the first term is significantly larger than the second though the smaller term is retained as it contains L_φ and therefore the temperature dependence. As T is decreased, the coherence length grows until it becomes larger than the system size. At this point the entire system is phase coherent and the upper integration limit should be replaced by the time to diffuse across the system, which has the consequence of making the replacement $L_\varphi \to L$ in the correction to the conductivity, Eq. (1.7).

The weak localisation corrections are small for $k_{\mathrm{F}}l \gg 1$, however these corrections are not guaranteed to be small in strongly disordered systems and once the corrections

[2]The derivation can be found in many textbooks on QFT, for example, [43, 44].

begin to become large, it is more appropriate to consider the system moving towards the strongly localised regime, which will be discussed in more detail in the next chapter. The length scale at which this occurs is the localisation length, ξ, and can be estimated from Eq. (1.7) by demanding that $|\Delta\sigma/\sigma_0| \sim 1$ when the phase coherence length or the system size (depending on which is involved in the conductivity correction) is approximately equal to the localisation length [28]. The existence of a localisation length has the following consequence; if $L_\varphi \ll \xi$, the system is in the weak localisation regime, given by Eq. (1.7), where the interference correction to the conductivity is small. Strong localisation cannot occur as it requires phase coherence across the entire localised region. However, in the opposite limit, $L_\varphi \gg \xi$, strong localisation is able to occur before the phase coherence is lost and the system is in the strongly localised regime, which will be discussed more in the following chapter. In the case where the phase coherence length is much larger than the system size (as can occur at very low temperatures), then the same arguments apply but for L instead of L_φ.

CHAPTER 2

LOCALISATION

In this chapter, the concept of localisation in electronic systems will be explored. Previously, it was shown that quantum corrections can reduce the conductivity in disordered systems by increasing the probability of return and therefore reducing the probability of diffusing away. This weak localisation correction is valid in weakly disordered materials where $k_{\mathrm{F}}l \gg 1$. In systems where the disorder is increased, such that $k_{\mathrm{F}}l \lesssim 1$, then the quantum corrections are no longer small and the regime of Anderson localisation is entered. This chapter will explain this regime and explore how finite temperatures and phonons can destroy localisation. The role of electron-electron interactions will then be discussed and how this is not necessarily sufficient to destroy localisation, leading to a finite-temperature insulating state, this phenomenon is many-body localisation (MBL). A discussion of the phenomena associated with MBL will follow this in addition to some of the experimental signatures and the problems with observing MBL in solid-state systems.

2.1 Anderson Localisation

Anderson localisation is a single-particle phenomenon in disordered materials, where the conductivity vanishes at $T = 0$, due to a wave function,

$$|\psi(x)|^2 \sim \mathrm{e}^{-|x|/\xi}, \tag{2.1}$$

that decays exponentially with a natural length, ξ, known as the localisation length.

Localisation was initially predicted in 1958 when P. W. Anderson studied a hopping model on a disordered lattice at $T = 0$ [45]. He considered a tight-binding model with the Hamiltonian

$$H = \sum_i \varepsilon_i c_i^\dagger c_i + \sum_{\langle ij \rangle} \left(V_{ij} c_i^\dagger c_j + \text{h.c.} \right), \tag{2.2}$$

where $c_i^\dagger (c_i)$ are the creation (annihilation) operators for electrons on a site i and $\langle ij \rangle$ indicates the sum is over the nearest neighbour pairs. Either (or both) the onsite energy, ε_i, or the hopping amplitude, V_{ij}, can be random to represent contributions to diagonal and off-diagonal disorder respectively. If the disorder is taken to be diagonal then $V_{ij} = V$ and the onsite energies are randomly drawn from the interval $\varepsilon_i \in [-W, W]$, with the parameter W/V describing the amount of disorder in the system. For vanishing disorder $W/V \to 0$, the electrons are free to hop (with some weak scattering) so are delocalised across the lattice. In the opposite limit where disorder dominates the system, $W/V \to \infty$, the electrons are strongly localised to a single site and therefore, as Anderson found, there is a localisation-delocalisation transition at a critical amount of disorder $(W/V)_{\text{cr}}$. This localised regime results in an absence of transport across the system.

Anderson localisation has been the subject of numerous studies since (see reviews [11–14]) and one of the most useful theories that captures the key results is the scaling theory of localisation.

2.2 Scaling Theory of Localisation

The scaling theory of localisation was originally introduced in 1979 [46] and aims to capture all the ideas discussed so far in this thesis with regards to the conductance. In particular, it explores the effect of the system size, L, on the conductance. To achieve this, it interpolates between the known macroscopic regimes of Ohmic conductance ($g \gg 1$) and localisation ($g \ll 1$), where $g = G/(e^2/h)$ is the dimensionless conductance. In the Ohmic regime, the conductance is given by Eq. (1.1) and can be written as $g(L) \approx (h/e^2)\sigma_0 L^{d-2}$

and for the localised regime $g(L) \approx g_0 \mathrm{e}^{-(L/\xi)}$. Here σ_0 is defined via Eq. (1.2) and g_0 is a constant.

The scaling hypothesis revolves around being able to write $g(\alpha L)$ as a function of $g(L)$. Defining $\alpha = 1 + \epsilon$ ($\epsilon \ll 1$), the scaling hypothesis can be expressed via a scaling function $\beta(g)$,

$$g(\alpha L) \approx g(L)[1 + \epsilon\beta(g(L))], \tag{2.3}$$

where the scaling function is monotonic and defined by

$$\beta(g) = \frac{\mathrm{d}\ln g}{\mathrm{d}\ln L}. \tag{2.4}$$

This definition can be used in conjunction with the results above for large and small g to give

$$\beta(g) \approx \begin{cases} d - 2 - \frac{C_d}{g}, & g \gg 1, \\ \ln(g/g_0), & g \ll 1, \end{cases} \tag{2.5}$$

with $C_d \sim 1$. In the large g limit, a small correction in $1/g$ has also been included and this corresponds to the weak localisation correction calculated in the previous chapter (with L rather than L_φ). From Eq. (2.4), it can be observed that for positive $\beta(g)$, the conductance increases with increasing system size and for negative $\beta(g)$, g decreases with increasing system size. In combination with the results in Eq. (2.5), this can be used to sketch the RG-flow (renormalisation group flow[1]) in Fig.2.1. The conductance can then be obtained by integrating the scaling function, Eq. (2.4).

[1]Scaling theory and RG-flows are more general concepts than mentioned here. They will not be reviewed in detail here but see [47] for an introduction.

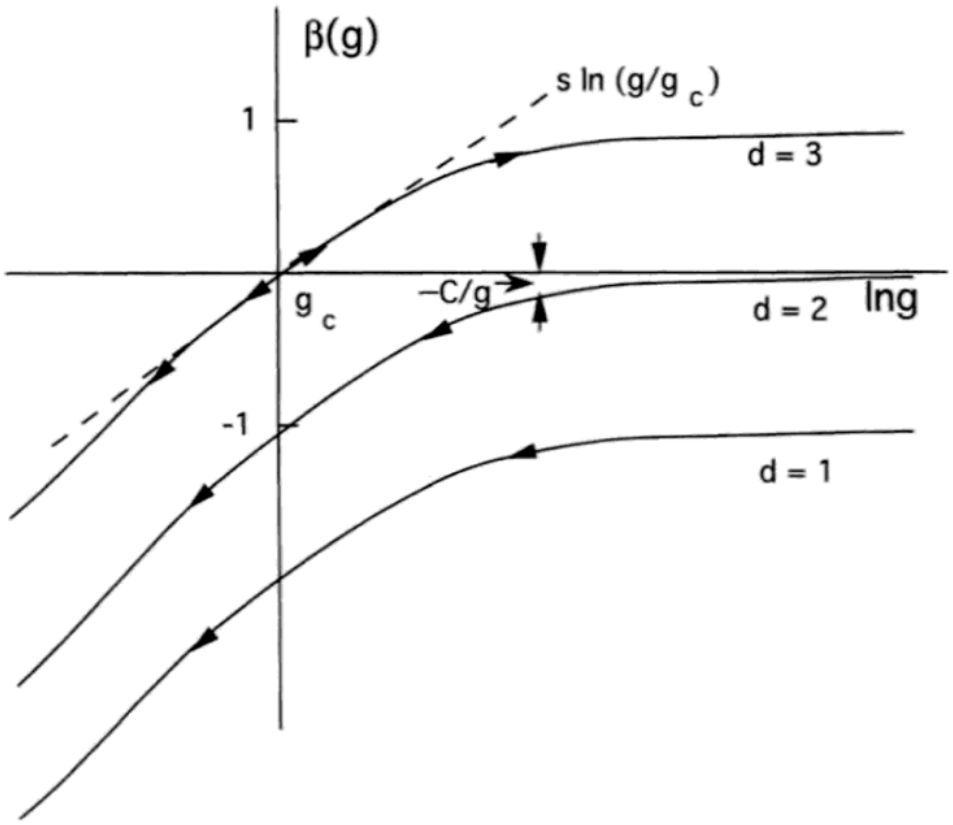

Figure 2.1: The scaling function, $\beta(g)$ in $d = 1, 2, 3$. The arrows represent how β changes as L is increased. For $d = 1, 2$ the flow is always towards the localised insulating state but for $d = 3$ there is a metal-insulator transition. Figure taken from [14].

2.2.1 One Dimension

In one dimension, it is clear from both Eq. (2.5) and Fig. 2.1 that $\beta(g) < 0$ for all g and therefore as $L \to \infty$, the conductance approaches the localised regime. Therefore, for an arbitrary amount of disorder all states in 1d are localised. As seen in Chapter 1, the localisation length is defined when the corrections to the Ohmic regime become non-negligible. In order to obtain this, the large g limit of Eq. (2.5) is integrated between $L = l$ (which is the smallest scale under consideration in the diffusive regime) where $g = g_l$ and $L = \xi$, where $g \sim 1$. After performing the integration and using that the conductivity is Ohmic across a mean free path and interference effects are not important so $g_l = (h/e^2)\sigma_0/l$, it is found that $\xi \sim l$, which is expected as there is no way to move

around the disorder in 1d.

2.2.2 Two Dimensions

In two dimensions, despite it being the edge case[2], the weak localisation correction again means that $\beta(g)$ is always negative and all states are localised for an arbitrary amount of disorder. The localisation length can be calculated in the same way as the 1d case, giving

$$\xi \sim l\mathrm{e}^{g_l} \sim l\mathrm{e}^{k_\mathrm{F} l}. \tag{2.6}$$

This exponential dependence has important consequences experimentally as it is important to remember that for localisation to occur $\xi \ll L, L_\varphi$ is required. This means that realistically $k_\mathrm{F} l \sim 1$ is required to ensure the localisation length is not exponentially large. This gives the Ioffe-Regel criterion mentioned in the previous chapter.

2.2.3 Three Dimensions

In three dimensions (and higher), $\beta(g)$ is no longer always negative and so not all states are localised for an arbitrary amount of disorder. Instead, there is a value of conductance, g_cr, below which the system tends towards the localised regime as $L \to \infty$ and above it, tends to the Ohmic regime. Therefore, a metal-insulator transition exists which is not present in lower dimensions. The critical conductance for the transition corresponds to the zero in the scaling function, $\beta(g_\mathrm{cr}) = 0$, and is given by $g_\mathrm{cr} \sim 1 \Rightarrow G \sim e^2/h$ [46]. Around this point, the β-function is linear in g,

$$\beta(g) = \frac{\mathrm{d}\ln g}{\mathrm{d}\ln L} = \gamma\left(\frac{g - g_\mathrm{cr}}{g_\mathrm{cr}}\right). \tag{2.7}$$

[2]Without the weak localisation correction $\beta(g) = 0$ in the $g \gg 1$ limit, so it is not clear whether the behaviour is metallic or insulating in the macroscopic limit.

This can be integrated from the mean free path, l, (which is the microscopic length scale in the system) to L, which gives the conductivity around the transition,

$$\frac{g - g_{\rm cr}}{g_{\rm cr}} = \left(\frac{g_l - g_{\rm cr}}{g_{\rm cr}}\right)\left(\frac{L}{l}\right)^{\gamma}, \tag{2.8}$$

which is valid providing that $|g - g_{\rm cr}|/g_{\rm cr} \ll 1$. As for lower dimensions, the localisation length is defined as the point at which the corrections become significant on the insulating side of the transition. When the ratio defined by Eq. (2.8) is approximately one, the length scale that arises is

$$\xi \sim l \left|\frac{g_l - g_{\rm cr}}{g_{\rm cr}}\right|^{-\frac{1}{\gamma}}, \tag{2.9}$$

where $1/\gamma$ is the critical exponent (often referred to as ν in the literature) and has a value of approximately 1.5 [12, 48]. For the insulating side of the transition this corresponds to the localisation length as seen in the lower dimensions, however, on the metallic side of the transition, this simply corresponds to the length above which Ohmic conductance is seen. In this limit, the conductivity, σ_ξ is a constant and it is found that in the metallic regime for $L \gg \xi$, σ scales as

$$\sigma_\xi \approx \frac{g_\xi}{\xi} \sim \frac{g_{\rm cr}}{l}\left|\frac{g_l - g_{\rm cr}}{g_{\rm cr}}\right|^{\frac{1}{\gamma}}, \tag{2.10}$$

where in the final expression, Eq. (2.9) has been used in conjunction with the fact that $g \sim g_{\rm cr}$ on all scales near the transition. Therefore, as the metal-insulator transition is approached, the conductivity vanishes with the same critical exponent as that involved with the localisation length divergence. This contradicts the idea of Mott's minimum metallic conductivity which suggested that no metals could exist with a conductivity less than $(e^2/h)k_{\rm F}$ [14, 49] and instead this should just be used as an estimate as to when quantum effects become important.

On the scales $L \gg \xi$, there is a clear distinction between the insulating and metallic states, however for $L \ll \xi$, both the metallic and insulating states behave the same. The

conductivity in this regime, σ_L, can be estimated by using the fact that g is approximately a constant near the transition. Therefore,

$$\sigma_L = \sigma_\xi \left(\frac{\xi}{L} \right), \tag{2.11}$$

which leads to a diffusive regime that is now scale-dependent [14, 50, 51].

2.3 Hopping Conductivity

Up until now, this thesis has focused on the concept of localisation at zero-temperature ($T = 0$) where inelastic processes, for example the electron-phonon interaction, are absent. However, at finite temperature, these must be considered and can result in numerous hopping processes that can restore transport.

First, the effects of temperature will be considered in the absence of the electron-phonon interaction. In the previous section, it was shown that for $d \leq 2$ all states are localised for any finite amount of disorder, resulting in vanishing conductivity for all T. However, in higher dimensions, this is only true above a critical threshold and for an intermediate amount of disorder, the mobility edge becomes relevant. The mobility edge separates delocalised (or extended) states located in the middle of the energy band from localised states which are at the edge, where the electrons have a lower kinetic energy. These states cannot coexist at the same energy as any mixing simply results in extended states [52], hence the appearance of the mobility edge. As the disorder of the system is increased, the mobility edge moves until all states become localised at sufficiently high disorder. Finite temperatures allow for activation of the electrons across the mobility edge, ε_m, giving a conductivity proportional to the probability of excitation

$$\sigma(T) \sim \mathrm{e}^{-\beta(\varepsilon_\mathrm{m} - \varepsilon_\mathrm{F})}, \tag{2.12}$$

where $\beta = 1/k_\mathrm{B}T$ and ε_m is the mobility edge.

2.3.1 Mott's Variable Range Hopping

When the electron-phonon interaction is also included, inelastic hopping processes can occur between different localised states. This bypasses the need for electrons to be activated above the mobility edge and therefore can destroy localisation at all non-zero temperatures even in the lower dimensions. For instance, a phonon may have the energy to cause electrons to hop to the nearest localised state a distance ξ away. For a constant density of states, ν_0, the energy separation between the two neighbouring localised states is given by $\Delta_\xi \sim 1/(\nu_0 \xi^d)$, leading to the hopping conductivity [14]

$$\sigma(T) \sim \mathrm{e}^{-\beta\Delta_\xi}. \tag{2.13}$$

However, it may be more energetically favourable to hop further than the neighbouring localised state via a process known as Mott's variable range hopping (VRH) [53–55]. In this instance, a balance is found between states that are close in space but may be far apart in energy and those that are further away in space but may be closer in energy as illustrated in Fig. 2.2.

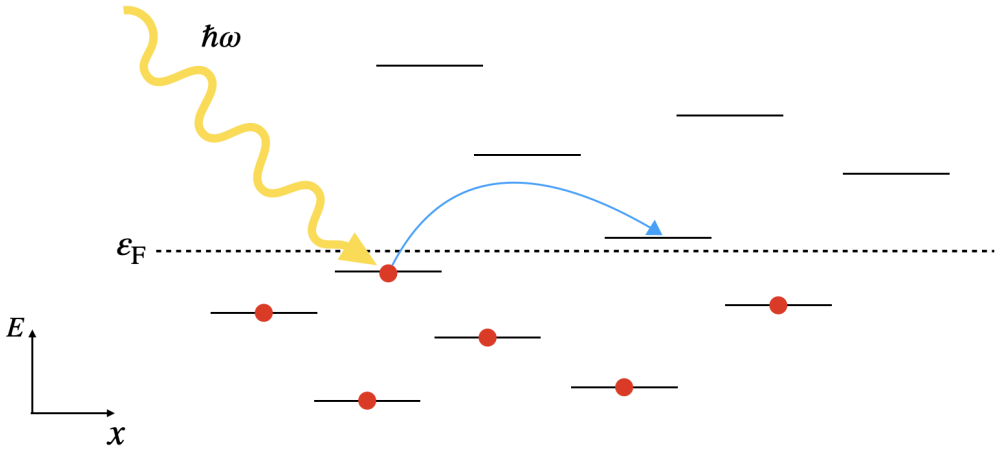

Figure 2.2: Phonon-induced variable range hopping. An electron is able to hop to another localised state that may be further away in space but closer energetically, via a phonon of energy $\hbar\omega$.

The probability of hopping over a distance $x \gg \xi$ is given by

$$P_{\text{tot}} \sim \mathrm{e}^{-(\beta\Delta_x + \frac{2x}{\xi})}, \tag{2.14}$$

where $\Delta_x \sim 1/(\nu_0 x^d)$ is the mean spacing between energy levels separated by a distance x. The first term in the exponent is due to the energetic difference between the two levels and the second is due to the square of the matrix elements decaying with distance on a scale ξ [14]. Maximising this probability, which corresponds to minimising the exponent, leads to a form of the conductivity

$$\sigma(T) \sim \mathrm{e}^{-\left(\frac{T_0}{T}\right)^{\frac{1}{d+1}}}, \tag{2.15}$$

where T_0 is the temperature below which VRH becomes the dominant mechanism and is given by $k_{\text{B}}T_0 \sim \Delta_\xi$. At higher temperatures, either the nearest neighbour hopping or the activation to the mobility edge are the relevant mechanisms, with the dominant one being that with the larger probability [14].

2.3.2 Efros-Shkolvskii Hopping

Mott's VRH is still a single-electron phenomenon, that is it doesn't incorporate electron-electron interactions. This is usually an appropriate approximation in metals when the long-range Coulomb interaction is screened, however if the screening isn't as prominent then this must be considered. Electron-electron interactions are known to modify the density of states (DoS) in other situations, for example in the zero-bias anomaly [6, 7], and so in the instance of VRH (which assumes a constant DoS), it is natural to explore how the density of states is affected and the effect this has on transport. Whilst there exists no microscopic theory, Efros and Shklovskii [56] were able to show that the Coulomb interaction results in a gap opening up in the density of states which changes the power in the exponent of VRH conductivity (Eq. (2.15)) to one that is independent of the

dimensionality

$$\sigma(T) \sim \mathrm{e}^{-\left(\frac{T_{\mathrm{ES}}}{T}\right)^{\frac{1}{2}}}, \tag{2.16}$$

where T_{ES} is the temperature below which Efros-Shklovskii hopping becomes relevant.

2.4 Many-Body Localisation

A natural question to ask after the introduction of Anderson localisation is how does this generalise to interacting systems? The previous section showed how the presence of phonons (both with and without electron-electron interactions) destroys localisation by providing the electrons with energy to hop between different localised states. The work of Fleishman and Anderson [57] suggested that short-range electron-electron interactions on their own in the presence of strong disorder may not do the same. This result was expanded on when the scaling theory of localisation was extended to include interactions [58]. However, localisation at finite temperatures was first introduced in the case of quantum dots where it was found that below a certain energy, excitations would be localised in many-body (Fock) space [24] (see Chapter 5 for a more detailed discussion on this). A similar regime was later identified in higher dimensions [20, 22], with this being what is now recognised as many-body localisation (MBL).

In their seminal work Basko, Aleiner, and Altshuler (BAA) [20], were able to show to all orders in perturbation theory that localisation was robust to the electron-electron interaction providing that it is sufficiently weak (the coupling constant $\lambda \ll 1$) and short-range and that the temperature of the system is below a critical temperature defined in terms of the mean level spacing, Δ_ξ,

$$T_{\mathrm{c}} = \frac{\Delta_\xi}{\lambda \ln(1/\lambda)}. \tag{2.17}$$

This survival of localisation leads to a finite-temperature insulating state as shown in Fig. 2.3. The onset of metallic behaviour occurs at temperatures above T_{c}, with a crossover

to a hopping regime at $T = \Delta_\xi/\lambda$. Unlike the regimes of Mott's variable range hopping and Efros-Shklovskii hopping the conductivity in this case is power-law rather than exponential. At higher temperatures ($T > \Delta_\xi/\lambda^2$), the discrete levels of the system become smeared and Drude conductivity, Eq. (1.2), is restored [20]. The physics of the transition to this metallic regime is an active area of research and a discussion of this and other areas of current interest in MBL will be presented towards the end of this chapter.

As was the case with quantum dots, BAA demonstrated a localisation in Fock space. By starting in the case where all single-particle states are localised, they considered how the electron-electron interaction can cause a high-energy single-particle state to decay into lower-energy many-body states. If the single particle state decays into all possible many-body states, there is delocalisation in Fock space. However, at lower temperatures, the single particle state may remain (potentially coupled to just a few many-particle states) - this is localisation in Fock space. During the decay, the single particle state should be broadened according to the finite lifetime of the state. If this broadening, characterised by the decay rate, Γ, goes to zero then localisation survives. Therefore, by studying the statistics of Γ, BAA were able to distinguish the metallic from the insulating state. On the metallic side of the transition, the excitation decays indefinitely into all many-body states so Γ is a smooth function of energy and the probability distribution for Γ is a Gaussian centred around some mean. This is different from the insulating side of the transition, where Γ as a function of energy is a collection of δ-function peaks and so the probability of finding a non-zero Γ vanishes for arbitrary energy.

Since the initial developments in MBL, there have been numerous studies extending the research in this area - for example see reviews [15–17]. The remainder of this chapter is dedicated to understanding some of the key results regarding MBL, both theoretically and experimentally.

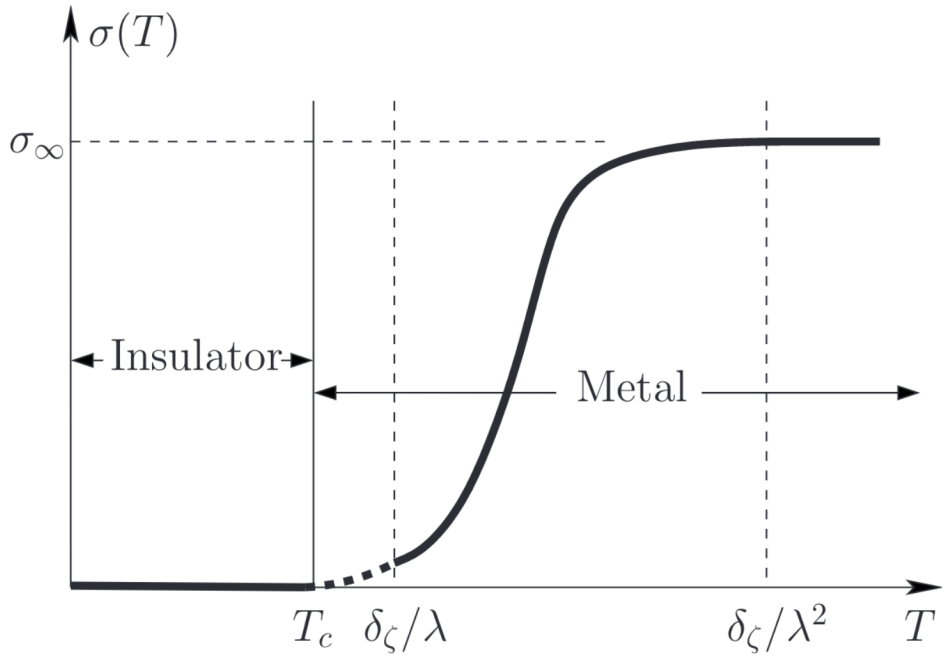

Figure 2.3: The conductivity as a function of temperature for MBL systems. Here δ_ζ is the mean level spacing and λ is the electron-electron coupling constant. Below the critical temperature, T_c, the state is insulating with zero conductivity. At high temperatures ($T > \delta_\zeta/\lambda^2$), the conductivity has a Drude form, σ_∞ (see Eq. (1.2)), A power-law hopping regime occurs for intermediate temperatures. Figure taken from [27].

2.4.1 Eigenstate Thermalisation Hypothesis

One reason for the major interest in MBL in recent years is that systems which are localised fail to thermalise. Most systems are expected to act as their own thermal bath and therefore thermalise, thus having a class of systems that fails to do so is of theoretical and experimental interest. Intuitively, for thermalising systems to act as their own bath they require transport in order for energy to be transferred between different parts of the system (or different subsystems). Therefore systems exhibiting MBL where there is an absence of transport, do not thermalise. This idea can be put onto a firmer footing through the eigenstate thermalisation hypothesis (ETH) [59–62], which is the standard way of defining thermalising (or equivalently ergodic) systems in quantum mechanics.

In thermalised systems with a well-defined energy E, the long-time average of a local

observable, $\langle O\rangle_\infty$, should be equal to the microcanonical average at the energy E,

$$\langle O\rangle_{mc}(E) = \frac{1}{N_{\Delta E}} \sum_{E_n \in E \pm \Delta E} \langle n|O|n\rangle \tag{2.18}$$

where $N_{\Delta E}$ is the number of states summed over in the energy window $E - \Delta E < E_n < E + \Delta E$ ($\Delta E \ll E$) and $|n\rangle$ are the many-body eigenstates of the Hamiltonian, H, with an energy E_n. Now, to define the long-time average consider a generic state, $|\psi(t)\rangle$, evolving under this Hamiltonian,

$$|\psi(0)\rangle = \sum_n A_n|n\rangle \implies |\psi(t)\rangle = \mathrm{e}^{-iHt}|\psi(0)\rangle = \sum_n A_n \mathrm{e}^{-iE_n t}|n\rangle, \tag{2.19}$$

which leads to the long-time average of a local observable, O,

$$\langle O\rangle_\infty = \lim_{T\to\infty} \frac{1}{T} \int_0^T \langle\psi(t)|O|\psi(t)\rangle \mathrm{d}t = \sum_n |A_n|^2 \langle n|O|n\rangle. \tag{2.20}$$

There is a clear issue when trying to equate the expression in Eq. (2.18) with that in Eq. (2.20) and this refers to how the latter expression depends on the initial state via the coefficients $|A_n|^2$, whereas the microcanonical average does not depend on the initial state. The ETH resolves this apparent issue by saying that thermalisation occurs on the level of individual eigenstates and this ensures the thermalisation of local operators, as the long-time average defined by Eq. (2.20) becomes equivalent to the thermal value defined by the microcanonical ensemble. More rigorously it states that the expectation value of an operator in an eigenstate, $|n\rangle$, is equal to the microcanonical average defined at that energy, $\langle n|O|n\rangle = \langle O\rangle_{mc}(E_n)$. As this is a smooth function of energy, providing that the coefficients $|A_n|^2$ are peaked around the energy of the system, E, then Eq. (2.20) and Eq. (2.18) give the same result and the system is thermalised. In MBL systems, the value of an observable retains information of the initial state even at long times and therefore is non-thermal.

Although most systems are known to thermalise, not all systems do and a particular

class that violates the ETH are integrable systems. Due to the interchangeability between thermalisation and ergodicity in regards to the ETH, thermalisation can be viewed as exploring all of phase space whilst obeying all globally conserved quantities. In integrable systems this does not occur as the extensive set of conserved quantities they possess strongly limits the dynamics of the system and hence there is an absence of thermalisation. Systems that exhibit MBL have a similar property with the emergence of local integrals of motion (LIOMs or l-bits) that lead to non-ergodic and non-thermal behaviour, meaning MBL systems are termed quasi-integrable. The key difference between this quasi-integrability and normal integrability is that these conserved quantities are quasi-local and robust. When an integrable system is perturbed it tends to become non-integrable and this will restore ergodicity. In contrast to this, if an MBL system is perturbed it will remain many-body localised and therefore non-ergodic. It is the only known robust way of violating thermalisation [15, 16].

The l-bits proposed to describe MBL lead to explanations of a variety of different phenomena associated with MBL that will shortly be discussed. They additionally describe the spatial structure of MBL. As was previously mentioned, the original works of MBL identified localisation in Fock space. The development of l-bits extended this to localisation in real space as the l-bits can be written as operators localised around certain sites with the exponential decay being characterised by the localisation length, ξ [15–17].

2.4.2 Entanglement in MBL

In addition to the absence of transport and thermalisation, there are many other properties of MBL, for example the absence of level repulsion which causes the level statistics to adopt a Poisson distribution. Many of these properties are not discussed in this work and instead the reviews [15–17] and references within should be consulted. Perhaps the most significant of the signatures of MBL is discussed though, this being the behaviour of the entanglement entropy, as this is where a key difference between MBL, Anderson localisation, and thermalisation lies.

To begin, consider preparing the system in an eigenstate of the generic MBL Hamiltonian [16, 63, 64]

$$H = \sum_i h_i \tau_i^z + \sum_{i>j} J_{ij} \tau_i^z \tau_j^z + \sum_{i,j,k} J_{ijk} \tau_i^z \tau_j^z \tau_k^z + \ldots, \tag{2.21}$$

where τ_i^z are the l-bit operators that decay on a distance ξ and behave like $\sigma^{(z)}$ (the z-component of the Pauli matrices) to leading order, h_i is an onsite field and the J's are the coupling between the l-bits, with

$$J_{ij} \sim J_0 \mathrm{e}^{-|i-j|/\xi_{\mathrm{dyn}}} \quad \text{and} \quad J_{ijk} \sim J_0 \mathrm{e}^{-|i-k|/\xi_{\mathrm{dyn}}} \quad \text{etc.}, \tag{2.22}$$

where ξ_{dyn} is a length scale representing the dephasing dynamics of the system. Then entanglement is defined by partitioning the system. Consider a system divided into two subsystems A and B. As the coupling between them simply occurs across the boundary between the two (due to the exponential decay in Eq. (2.22)), then the entanglement between the two subsystems is proportional to the size of the boundary[3]. Therefore, as the size of the system is increased, the entanglement scales with the size of this boundary and therefore the eigenstates have area law scaling (see Fig. 2.4). This is also true of Anderson localised systems, however in contrast to this, thermal systems have volume law scaling where the entanglement entropy scales with the subsystem size as there is no such restriction on the coupling in this instance.

[3]The entanglement entropy is typically characterised by the von Neumann entropy though others can be used, for example the Rényi entropies. These will not be discussed in detail in this thesis, but see [65].

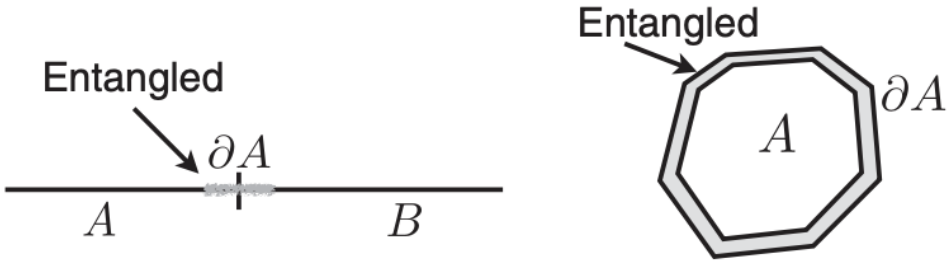

Figure 2.4: Area law entanglement for MBL eigenstates. This is because the coupling between subsystems occurs across a small region across the boundary only due to the exponential decay of the coupling between l-bits. Figure taken from [16].

The area law scaling is able to distinguish between localised and thermal systems however it cannot distinguish between Anderson localisation and MBL. One way to do this is to consider the dynamics of the system. If the system is prepared in a product state and allowed to evolve then in the case of Anderson localisation there will be no change in the entanglement entropy as there are no interactions between l-bits. However, in the case of MBL, it can be shown that the entanglement grows logarithmically with time [66]. Consider two spins separated by a distance x, these will become (almost) maximally entangled due to the couplings given by Eq. (2.22), over a time that is inversely proportional to the coupling strength

$$t \sim \frac{\hbar}{J_0} \mathrm{e}^{x/\xi_{\mathrm{dyn}}}. \tag{2.23}$$

This can be inverted so that after a time t, spins separated by a distance $x(t)$ become entangled, leading to logarithmic entanglement growth as a function of time

$$S(t) \sim \xi_{\mathrm{dyn}} \ln\left(\frac{J_0 t}{\hbar}\right), \tag{2.24}$$

which is now seen as one of the defining features of MBL [15–17].

2.4.3 The Stability of MBL

One of the key areas of current research in the field of MBL is to understand if a stable MBL regime exists and the nature of the transition between the metallic and insulating regimes (for a review see [67]). The initial work into MBL suggested a transition to a finite-temperature insulating state in arbitrary dimension and was found to be true to all orders in perturbation theory. This finite-temperature transition arises as a consequence of a proposed many-body mobility edge which occurs at an energy proportional to the systems volume, such that it occurs at a finite energy density in the thermodynamic limit [20]. This idea was originally supported by numerics [68], which found a many-body mobility edge separating localised and extended states. However, it was later suggested that this arose due to finite-size effects and actually the many-body mobility edge doesn't survive in the thermodynamic limit due to the mobility of a thermal bubble[4] which delocalises the entire system [69].

Another point of active research is the existence of MBL in dimensions higher than $d = 1$. Again, the initial work into MBL [20] suggests that MBL occurs in arbitrary dimensions and in $d = 1$ this existence has been supported by a more rigorous approach which also takes into account non-perturbative effects [70]. Despite this, there has been no such confirmation for $d > 1$ and it has been suggested that the presence of ergodic bubbles due to disorder fluctuations can again destroy the MBL regime [71]. However, once again this is not conclusive and has led to studies (for example [72]) of a finite-size (or finite-time) MBL regime, where the system may still behave as if it is many-body localised in experimentally accessible systems, as well as a prethermal regime where again localised physics may appear [73].

It is worth noting that in both of these discussions, MBL is defined via the existence of an extensive set of local integrals of motion (the l-bits) and using this framework various other aspects of MBL and the transition have been studied. For example, an RG approach

[4]These have a higher temperature than the rest of the sample and are ergodic. Additionally, they always exist at finite-T in the thermodynamic limit.

has been developed (see, for example, [74–76]), similar to that in Anderson localisation and Griffiths effects (the presence of rare insulating regions) have been explored on the metallic side of the transition [77], which lead to subdiffusive transport regimes. The transition will be discussed in more detail in Chapters 5 and 6, where the Fock space structure and the temperature-induced transition will be explored in greater detail.

Although this definition of MBL in terms of the local integrals of motion has clearly led to progress and puts MBL on a more 'rigorous' mathematical footing, it is also what causes such an in-depth discussion of the stability of any MBL phase. Whilst this discussion has its merits, it is not definitive and does not necessarily mean that the original perturbative work of Basko, Aleiner and Altshuler [20] is no longer applicable. First, many of the aforementioned works are numerical in nature and this has limitations based on the size of the system that is available [78]. Therefore, when drawing conclusions about the thermodynamic limit additional care should be taken. Furthermore, and more relevant to this work, are the implications for experiments. Although there is a possibility that a stable MBL phase may not exist in higher dimensions or at finite temperatures in the thermodynamic limit, this does not mean that it is not experimentally observable because of the finite scales involved. Both a finite system size and experimental timescale may allow for the observation of MBL physics and this will be seen in the following section.

2.5 Experimental Progress in MBL

The degree of success in observing MBL in experiments has been largely dictated by the types of systems which are considered. The most fruitful setup has been that of ultracold atoms where there is a great deal of control over the system and its isolation from any external environment or thermal bath. By preparing the system in a state where only the even sites of an optical lattice were occupied and studying the imbalance

$$I = \frac{N_{\mathrm{E}} - N_{\mathrm{O}}}{N_{\mathrm{E}} + N_{\mathrm{O}}}, \tag{2.25}$$

between the number of electrons on odd, N_{O}, and even sites, N_{E}, the authors of [79] were able to identify signatures associated with non-ergodicity and MBL. For sufficiently large disorder the imbalance would retain information of the initial state and fail to relax towards zero which would be characteristic of a thermal state, see Fig. 2.5. Other signatures were also found such as the logarithmic growth of entanglement.

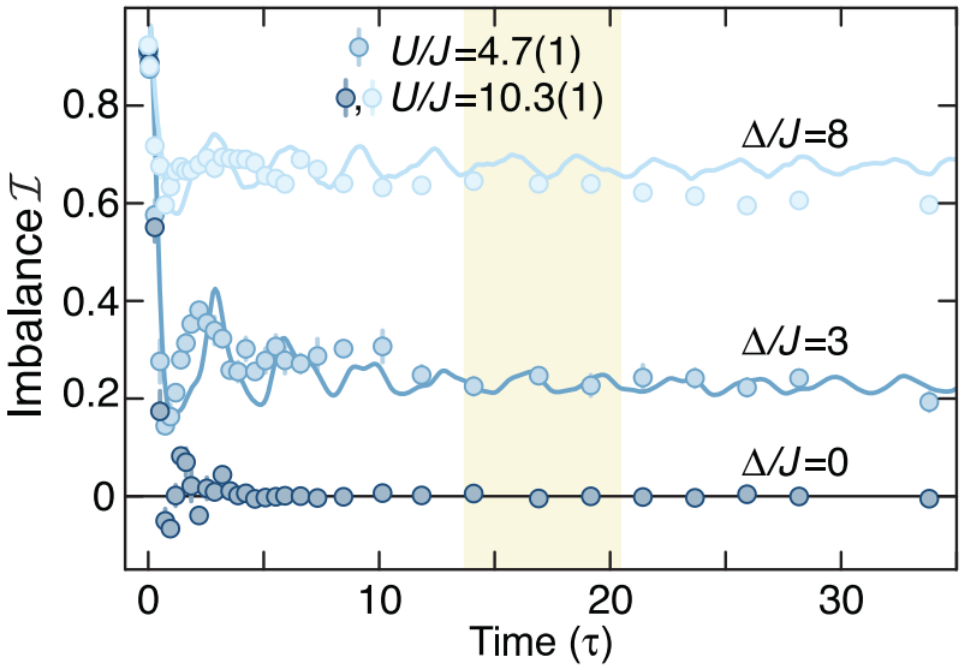

Figure 2.5: The imbalance as a function of time. As the disorder strength, Δ, is increased the system fails to thermalise, which is signified by the lack of relaxation to zero imbalance. Figure taken from [79].

Further experiments have explored other aspects of MBL, such as controlling the amount of dissipation in the system [80] and MBL in higher dimensions ($d = 2$) [81]. In these latter studies the imbalance was also used to identify a localised regime.

In contrast to these successes in ultracold atoms, there has been limited experimental success in more traditional solid-state systems, where MBL was initially predicted to manifest. Although there are limitations on detecting it in these systems, for example not being able to directly access entanglement entropy, the main restriction in these systems is the coupling to the environment. The presence of phonons is unavoidable and so decoupling between the electron and phonon subsystems must occur; this is one of the

key focuses of this work and will be built on in Chapter 4. Other experimental factors regarding electronic systems (including how MBL can be detected) will also be explored over the course of this thesis.

2.6 Summary

This chapter has provided an introduction to many-body localisation. Initially exploring the theory of single-particle localisation, it was seen how this is destroyed via hopping conductivity through the presence of phonons. Many-body localisation is a phenomenon characterised by inelastic electron-electron interactions failing to restore transport in the same way, leading to a non-ergodic regime. Since its inception, various aspects have been the subject of both theoretical and experimental interest, though many open questions still remain. The ideas outlined in this chapter will be drawn on throughout this thesis as they motivate the study of non-thermalising systems and the challenges in doing so.

CHAPTER 3

NON-EQUILIBRIUM FIELD THEORY

One of the most common analytical techniques in many-body physics is quantum field theory. The main topic of this thesis, many-body localisation, is an inherently non-equilibrium problem. Therefore, techniques suited to the non-equilibrium regime must be used and as a result the Keldysh formalism of quantum field theory becomes a viable option. There are various equivalent ways to approach this formalism, one of which is via path integrals (see [82, 83]), although here a different approach will be taken, more in line with that presented in [43, 84, 85]. In this chapter the formalism will be introduced and the various techniques required for the calculations in the rest of this work will be outlined.

3.1 Introduction to Green's Functions

Central to quantum field theory is the presence of correlation functions and in particular Green's functions, as these form the basis upon which physical observables can be calculated. For fermions, the single-particle Green's function (or propagator) can be defined

as[1] [40, 86]

$$G(\mathbf{r}, t; \mathbf{r}', t') = -\frac{i}{\hbar}\langle T\psi_{\mathrm{H}}(\mathbf{r}, t)\psi^{\dagger}_{\mathrm{H}}(\mathbf{r}', t')\rangle, \tag{3.1}$$

where $\psi^{\dagger}_{\mathrm{H}}(\psi_{\mathrm{H}})$ are the creation (annihilation) field operators for a fermion in the Heisenberg picture (see the next section for more details on this) and T is the time-ordering operator which puts the operators that act at a later time to the left. In doing so it should be noted that if two fermionic operators are interchanged a minus sign is acquired. Due to the presence of this time-ordering operator, this particular Green's function is sometimes called a time-ordered or causal Green's function. There are a variety of other Green's functions that can be defined (and will be over the course of this chapter) that have different meanings and uses.

The field operators introduced above are an alternative way of utilising second quantisation and represent the creation ($\psi^{\dagger}$) or annihilation (ψ) of a fermion at a given position and time. This means that the Green's function defined in Eq. (3.1) creates a particle at $(\mathbf{r}', t')$ and annihilates one at $(\mathbf{r}, t)$, hence why the Green's function may be described as the propagator of a particle from $(\mathbf{r}, t)$ to $(\mathbf{r}', t')$. In the case of free electrons in a metal, the Green's function can be calculated. These electrons are described by the Hamiltonian,

$$H = \sum_{\mathbf{k}} = \xi_{\mathbf{k}} c^{\dagger}_{\mathbf{k}} c_{\mathbf{k}}, \tag{3.2}$$

where $\xi_{\mathbf{k}} = \varepsilon_{\mathbf{k}} - \varepsilon_{\mathrm{F}}$ is the electron energy measured from the Fermi surface and $c^{\dagger}_{\mathbf{k}}(c_{\mathbf{k}})$ are the creation (annihilation) operators for an electron with momentum $\mathbf{k}$. In this instance, the field operators in a system of volume V can be expressed as [40]

$$\psi_{\mathrm{H}}(\mathbf{r}, t) = \frac{1}{\sqrt{V}} \sum_{\mathbf{k}} c_{\mathbf{k}} \mathrm{e}^{i(\mathbf{k}\cdot\mathbf{r} - \xi_{\mathrm{k}} t)}. \tag{3.3}$$

After substitution of this result and its conjugate into Eq. (3.1) and defining the occupation number at $T = 0$ to be $n_{\mathbf{k}} = \langle c^{\dagger}_{\mathbf{k}} c_{\mathbf{k}}\rangle = \Theta(k_{\mathrm{F}} - k)$ the Green's function can be

[1] Although, $\hbar$ has been explicitly included in this definition, $\hbar = 1$ will be used going forward in order to simplify the notation.

expressed as

$$G_0(\mathbf{r},t;\mathbf{r}',t') = -\frac{i}{V}\sum_{\mathbf{k}} \mathrm{e}^{i\mathbf{k}\cdot(\mathbf{r}-\mathbf{r}')-i\xi_{\mathbf{k}}(t-t')}\left[(1-n_{\mathbf{k}})\Theta(t-t') - n_{\mathbf{k}}\Theta(t'-t)\right], \tag{3.4}$$

where $\Theta(t)$ is the standard Heaviside step function. Performing a Fourier transform then gives the standard result [40, 86]

$$G_0(\mathbf{k},\varepsilon) = \frac{1}{\varepsilon - \xi_{\mathbf{k}} + i\delta\mathrm{sgn}(\xi_{\mathbf{k}})}, \tag{3.5}$$

with $\delta \to 0$. A similar analysis can be used to derive the Green's function for phonons. Phonons with momentum $\mathbf{q}$ are created and annihilated via the bosonic operators, $a^{\dagger}_{\mathbf{q}}$ and $a_{\mathbf{q}}$ respectively and have an energy $\omega_{\mathbf{q}}$, leading to them being described by the Hamiltonian $H = \sum_{\mathbf{q}} \omega_{\mathbf{q}}(a^{\dagger}_{\mathbf{q}}a_{\mathbf{q}} + \frac{1}{2})$. The phonon propagator, $D(\mathbf{r},t;\mathbf{r}',t') = -i\langle T\phi_{\mathrm{H}}(\mathbf{r},t)\phi_{\mathrm{H}}(\mathbf{r}',t')\rangle$,, which is defined in terms of a scalar field in the Heisenberg picture, ϕ_{H}, [40, 86], after Fourier transforming is given by,

$$D_0(\mathbf{q},\omega) = \frac{\omega^2_{\mathbf{q}}}{\omega^2 - \omega^2_{\mathbf{q}} + i\delta}. \tag{3.6}$$

The importance of these Green's functions to the method of quantum field theory stems from the fact that they can be used to calculate various physical properties of a system for example, the particle density or density of states. As will be seen in this chapter, this is achievable via the construction of perturbative schemes, so that the effects of interactions and disorder can be added to the free particle Green's functions introduced above, allowing for the study of a wide variety of systems which contain these effects. Further to this, it will be seen how these perturbative calculations are performed and the different types of Green's functions will be introduced and their relevance discussed.

3.2 Equilibrium Field Theory

Although the Keldysh formalism is a non-equilibrium technique, the developments of the equilibrium theory (see [40, 86]) are foundational and relevant aspects will be introduced first.

3.2.1 The Pictures of Quantum Mechanics

There are three ways of representing quantum mechanics. The first of these is perhaps the most familiar - the Schrödinger representation. In this picture, the wave functions, ψ, are time-dependent and their evolution is governed by the Schrödinger equation $i\partial_t\psi(t) = H\psi(t)$, where H is the Hamiltonian for the system. The operators, O, in this picture are time-independent.

The second picture is the Heisenberg picture, which shifts the time dependence from the wave functions, which become time-independent in this picture, to the operators which then evolve with the Hamiltonian, H, and are determined using the equation $O_H(t) = \mathrm{e}^{iHt}O(t=0)\mathrm{e}^{-iHt}$. In both of these instances, the expectation value of an operator O can be expressed as

$$\langle O\rangle = \langle\psi(0)|\mathrm{e}^{iHt}O(0)\mathrm{e}^{-iHt}|\psi(0)\rangle, \tag{3.7}$$

demonstrating the equivalence of the two pictures. The third picture of quantum mechanics is the interaction picture which combines aspects of both the Schrödinger and Heisenberg pictures. The Hamiltonian of the system is divided into two parts,

$$H = H_0 + V, \tag{3.8}$$

where H_0 is the quadratic or unperturbed Hamiltonian, which can be solved exactly (in other words, its eigenstates can be found) and V is the interacting part of the Hamiltonian.

Then the operators evolve with the 'easy' part of the Hamiltonian,

$$O_{H_0}(t) = \mathrm{e}^{iH_0 t} O(0) \mathrm{e}^{-iH_0 t}, \tag{3.9}$$

and in order to obtain the necessary expectation value of an operator O, given by Eq. (3.7), the states must evolve as

$$\psi(t) = U(t)\psi(0) = \mathrm{e}^{iH_0 t}\mathrm{e}^{-iHt}\psi(0). \tag{3.10}$$

The time evolution operator, $U(t) = \mathrm{e}^{iH_0 t}\mathrm{e}^{-iHt}$, obeys the differential equation,

$$\frac{\partial U(t)}{\partial t} = -iV_{H_0}(t)U(t), \tag{3.11}$$

with the boundary condition that $U(0) = 1$, where $V_{H_0}(t)$ is the evolution of the perturbation part of the Hamiltonian according to the quadratic part, given by Eq. (3.9). By solving this differential equation iteratively, the time evolution operator can also be expressed as [40, 86]

$$U(t) = T\mathrm{e}^{-i\int_0^t \mathrm{d}t' V_{H_0}(t')}. \tag{3.12}$$

3.2.2 S-matrix and Equilibrium Green's Function

In the interaction picture a state evolves from $t = 0$ up until some other time, according to Eq. (3.10). In general, a state evolves from t' to t via the S-matrix, $\psi(t) = S(t, t')\psi(t')$, where

$$S(t, t') = U(t)U^\dagger(t') = T\mathrm{e}^{-i\int_{t'}^t \mathrm{d}t_1 V_{H_0}(t_1)}. \tag{3.13}$$

The S-matrix can be used to calculate the Green's function [40, 86]

$$G(x, x') = -i\frac{\langle\varphi_0|TS(\infty, -\infty)\psi(x)\psi^\dagger(x')|\varphi_0\rangle}{\langle\varphi_0|S(\infty, -\infty)|\varphi_0\rangle}, \tag{3.14}$$

where $x = (\mathbf{r}, t)$ and $|\varphi_0\rangle$ is the ground state of H_0. It is this result that allows the construction of perturbation theory through the expansion of the S-matrix, after which a number of techniques can be used to calculate the Green's function such as Wick's theorem and the associated Feynman diagrams which will be discussed in more detail later in the chapter.

The Green's function in Eq. (3.14) is the causal or time-ordered Green's function. In equilibrium, it can be used to express the retarded and advanced Green's functions, as well as the greater and lesser Green's functions. The latter are directly related to physical observables and the former are useful for calculating a physical response. These will be discussed in more detail in the context of the non-equilibrium formalism but it is important to note that the calculation of the Green's function is important for calculating physical quantities such as currents.

The final thing to note is that the above discussion is applicable at zero temperature and in order to consider the effects of temperature in equilibrium, the Boltzmann factor, $\mathrm{e}^{-\beta(H-\mu N)}$ (with $\beta = 1/k_{\mathrm{B}}T$), must be incorporated into the Green's functions (and any other expectation value). This complicates the problem as now it is not only the S-matrix that needs to be perturbatively expanded but also this thermal weighting. Rather than performing this double expansion, a Wick rotation is performed by defining an imaginary time, τ, via $it = \tau$. The calculation of the Green's function is then performed using the Matsubara formalism, which won't be discussed in this thesis, but rather [40,82,86] should be consulted. Instead, this work focuses on dealing with finite temperature through the Keldysh formalism.

3.3 The Keldysh Formalism

Although many problems in mesoscopic physics can be dealt with through equilibrium field theory due to the desire to understand the linear response of a system, it is not always suitable. For instance, the absence of thermalisation in localised systems immediately

results in non-equilibrium phenomena and therefore an appropriate theory is required. Such a theory that is structurally equivalent to its equilibrium counterpart was initially introduced by Schwinger in 1961 [87] before being utilised further by Keldysh in 1964 [88] (see [43, 84, 85] for more recent treatments). In this section, this theory will be outlined and the associated techniques needed to perform calculations will be explored. Consider first the non-equilibrium Hamiltonian,

$$H(t) = H_0 + V + V'(t), \tag{3.15}$$

where, again H_0 is the solvable part of the Hamiltonian, V contains time-independent interactions and $V'(t)$ contains all the time dependence and is only non-zero for $t > t_0$. Therefore, up until the time t_0, the system evolves with a Hamiltonian $\tilde{H} = H_0 + V$ and can be dealt with using the above equilibrium theory. For $t > t_0$, the system then evolves under the action of the full Hamiltonian and so the expectation value of an operator $O(t)$ can be expressed in the interaction picture as,

$$\langle O(t)\rangle = \langle\psi_{t_0}|O_H(t)|\psi_{t_0}\rangle = \langle\psi_{t_0}|U^\dagger(t,t_0)O_{H_0}(t)U(t,t_0)|\psi_{t_0}\rangle, \tag{3.16}$$

where $|\psi_{t_0}\rangle$ is the state at $t = t_0$ and $O_{H_0}(t) = \mathrm{e}^{iH_0(t-t_0)}O(t_0)\mathrm{e}^{-iH_0(t-t_0)}$ is the evolution of an operator under the quadratic Hamiltonian H_0. The time evolution operator can be expressed in two equivalent forms, with the relation between them known as Dyson's formula [43, 85],

$$U(t,t_0) = \mathrm{e}^{iH_0(t-t_0)}T\mathrm{e}^{-i\int_{t_0}^{t}\mathrm{d}t' H(t')} = T\mathrm{e}^{-i\int_{t_0}^{t}\mathrm{d}t'\tilde{V}_{H_0}(t')}, \tag{3.17}$$

where $\tilde{V}_{H_0}(t) = V_{H_0}(t) + V'_{H_0}(t)$ and the operators with the subscript H_0 are defined as evolving under the quadratic Hamiltonian as above. Through comparison of the Heisenberg and interaction pictures (Eq. (3.16)), the expectation value of an operator at time t evolving under the full Hamiltonian, $\langle O_H(t)\rangle$ can be thought of as evolving the state from

t_0 to t using $U(t, t_0)$ and then acting the operator evolved under the quadratic Hamiltonian, $O_{H_0}(t)$ before evolving the state back to t_0 using $U^\dagger(t, t_0)$. This naturally leads to the definition of the operator on the double (or closed) time contour, C (see Fig.3.1),

$$O_H(t) = T_C \left(\mathrm{e}^{-i \int_C \mathrm{d}\tau \tilde{V}_{H_0}(\tau)} O_{H_0}(t) \right) \tag{3.18}$$

where the variable τ moves along the contour and T_C is the contour ordering operator so that operators acting at earlier points on the contour are on the right.

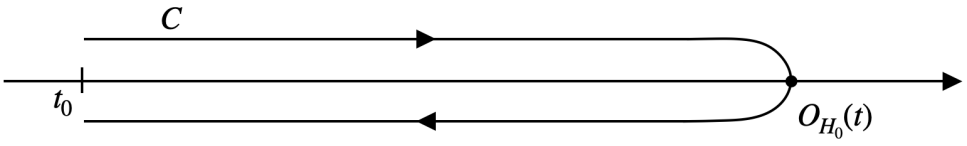

Figure 3.1: The double time contour, C. A state is evolved up to a time t where the operator evolved under the easy part of the Hamiltonian acts on it before being evolved back.

It is also necessary to see how the effect of finite temperature manifests itself in this formalism. The expectation value of an operator can be expressed as a trace, $\langle O(t) \rangle = \mathrm{Tr}\left(\rho_0 O_H(t)\right)$, via the density matrix, ρ_0, at the time t_0. At this time the system is in equilibrium, with the density matrix being given by the standard Gibbs state [43, 85]

$$\rho_0 = \frac{\mathrm{e}^{-\beta(H_0+V)}}{Z}, \quad Z = \mathrm{Tr}\left(\mathrm{e}^{-\beta(H_0+V)}\right), \tag{3.19}$$

where Z is the partition function. In order to see how this affects the contour structure, Dyson's formula (Eq. (3.17)) can be used on this thermal weighting factor, with the result amounting to that in Eq. (3.18), except along the contour C_K depicted in Fig. 3.2 and with the inclusion of the density matrix $\rho_{H_0} = \mathrm{e}^{-\beta H_0} / \mathrm{Tr}\left(\mathrm{e}^{-\beta H_0}\right)$ in the expectation value.

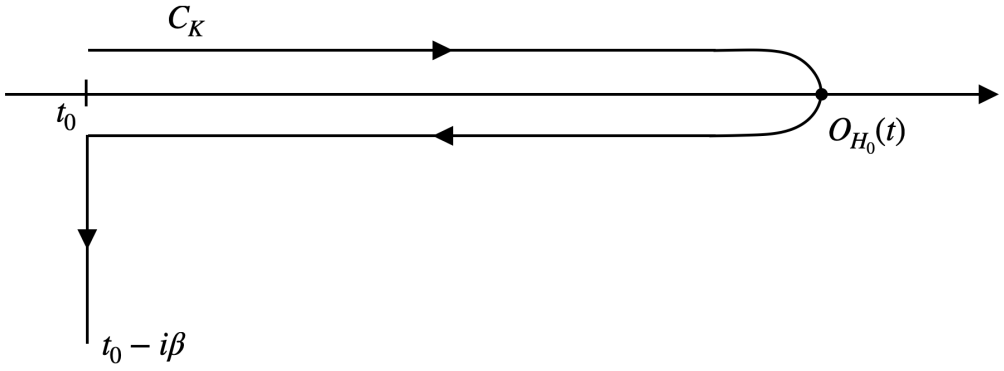

Figure 3.2: The complete Keldysh contour, C_K. The vertical part of the contour represents initial correlations and can be disregarded in many situations.

As the vertical part of the contour depends on the state for times less than t_0, it corresponds to the initial conditions and can often be neglected by taking t_0 to negative infinity. For instance, often the steady-state response is of interest and the information on the initial conditions will in many instances, have been lost when the steady-state has been reached and this vertical part of the contour can be neglected. Additionally, at higher temperatures, the length of this vertical segment becomes shorter and can be neglected as thermal fluctuations again smear out the effect of the initial conditions. If the initial correlations can be neglected then the evolution is simply over the contour C with the density matrix ρ_{H_0}.

3.4 Perturbation Theory - Feynman Diagrams and Wick's Theorem

In the previous section, it was seen how the Keldysh formalism can be used to describe the expectation value of a generic operator. Examples of such expectation values are the Green's functions which can subsequently be used to calculate the physical properties of the system. The contour-ordered Green's function is defined as

$$G(x, x') = -i\langle T_C \psi_H(x) \psi_H^\dagger(x') \rangle, \tag{3.20}$$

with $x = (\mathbf{r}, t)$. In the presence of interactions and disorder, this can be expressed as (using Eq. (3.18) and therefore ignoring the initial correlations)

$$G(x, x') = -i\langle T_C(S\psi_{H_0}(x)\psi^\dagger_{H_0}(x'))\rangle, \quad S = T_C \mathrm{e}^{-i\int_C \mathrm{d}\tau \tilde{V}_{H_0}(\tau)}. \tag{3.21}$$

Through comparison of this contour-ordered Green's function with its time-ordered counterpart in the equilibrium field theory Eq. (3.14), it can be seen that the formalisms are structurally equivalent. One key difference is that in this contour picture, the denominator which represents the partition function, Z, is equal to one due to contributions along the forward and backward contours cancelling out. As is the case in the equilibrium theory, the 'S-matrix' in Eq. (3.21) can be expanded, allowing a perturbative approach to interactions to be taken. The techniques that will be outlined here to achieve this are also found in equilibrium field theory [40, 86].

3.4.1 Coupling to a Scalar Field

In this section, electrons coupling to a scalar field, $\tilde{V}_{H_0}(\mathbf{r}, t) = \int \mathrm{d}\mathbf{r} U(\mathbf{r}, t)\psi^\dagger_{H_0}(\mathbf{r}, t)\psi_{H_0}(\mathbf{r}, t)$ will be considered. This could, for example, represent the scattering of electrons from impurities and this particular case will be dealt with further shortly. Here, rather, some of the generic techniques of perturbation theory will be introduced. Expanding the S-matrix to leading order in the interaction gives

$$\begin{aligned} G(\mathbf{r}, \mathbf{r}', t, t') &= G_0(\mathbf{r}, \mathbf{r}', t, t') \\ &\quad - \int_C \mathrm{d}\tau_1 \int \mathrm{d}\mathbf{r}_1 \langle U(\mathbf{r}, \tau_1)\rangle \langle T_C \psi^\dagger_{H_0}(\mathbf{r}_1, \tau_1)\psi_{H_0}(\mathbf{r}_1, \tau_1)\psi_{H_0}(\mathbf{r}, t)\psi^\dagger_{H_0}(\mathbf{r}', t')\rangle, \end{aligned} \tag{3.22}$$

where $G_0(\mathbf{r}, \mathbf{r}', t, t') = -i\langle T_C \psi_{H_0}(\mathbf{r}, t)\psi^\dagger_{H_0}(\mathbf{r}', t')\rangle$. The final average above contains four operators and in order to deal with this, Wick's theorem is used to split the average into averages of pairs of operators. The formal expression of Wick's theorem can be found in various texts introducing quantum field theory, for example see [40, 86], however here how

it works in practice will be briefly described. To use Wick's theorem, it must be noted that fermionic operators anti-commute and that for a quadratic Hamiltonian, an average must contain the same number of creation and annihilation operators and following this, all possible pairings of the operators are then found. To illustrate this, the four operators above can initially be paired as

$$\langle T_C \psi^\dagger_{H_0}(\mathbf{r}_1, \tau_1)\psi_{H_0}(\mathbf{r}_1, \tau_1)\rangle \quad \text{and} \quad \langle T_C \psi_{H_0}(\mathbf{r}, t)\psi^\dagger_{H_0}(\mathbf{r}', t')\rangle, \tag{3.23}$$

but, additionally, the middle two operators can swap positions (at the cost of a minus sign) to give the pairing

$$\langle T_C \psi^\dagger_{H_0}(\mathbf{r}_1, \tau_1)\psi_{H_0}(\mathbf{r}, t)\rangle \quad \text{and} \quad \langle T_C \psi_{H_0}(\mathbf{r}_1, \tau_1)\psi^\dagger_{H_0}(\mathbf{r}', t')\rangle. \tag{3.24}$$

There are no other unique pairings that contain one creation and one annihilation operator as the reordering of operators within these pairs is dealt with (up to a minus sign) by the contour-ordering operator. Therefore, after using Wick's theorem on Eq. (3.25), the Green's function can be written as

$$\begin{aligned} &G(\mathbf{r}, \mathbf{r}', t, t') = G_0(\mathbf{r}, \mathbf{r}', t, t') \\ &+ \int_C \mathrm{d}\tau_1 \int \mathrm{d}\mathbf{r}_1 \langle U(\mathbf{r}_1, \tau_1)\rangle \Big[G_0(\mathbf{r}, \mathbf{r}_1, t, \tau_1)G_0(\mathbf{r}_1, \mathbf{r}', \tau_1, t') - G_0(\mathbf{r}, \mathbf{r}', t, t')G_0(\mathbf{r}_1, \mathbf{r}_1, \tau_1, \tau_1)\Big]. \end{aligned} \tag{3.25}$$

The expression can then be represented using Feynman diagrams[2]. A bold line is used to denote a full Green's function, G, a thin line for the free Green's function, G_0 and a cross indicates the average of the potential. The integration then occurs over all internal indices. Using this notation, the second term in Eq. (3.25) leads to two diagrams as shown in Fig. 3.3. The first of these diagrams is a connected diagram as everything is connected to the two external vertices (the $(\mathbf{r}, t)$ and $(\mathbf{r}', t')$). On the other hand, the second is

[2]Various, well-established rules already exist for writing down the diagrams [40, 86], many of which will be explored in this chapter.

a disconnected diagram with a vacuum contribution (no external 'legs'). This second diagram and disconnected diagrams in general give zero contribution to the full Green's function as the integral along the upper and lower branches of the Keldysh contour cancel each other out. Therefore, going forwards disconnected diagrams can be disregarded.

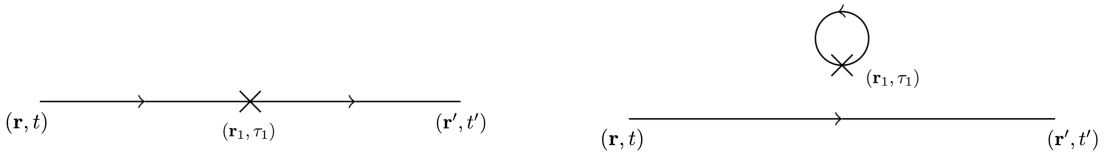

(a) **(b)**

Figure 3.3: The Feynman diagrams representing the first order correction to the electronic Green's function due to coupling to a scalar field. **(a)**: A connected diagram that contributes to the full Green's function. **(b)**: A disconnected diagram whose contribution vanishes due to a difference in sign between integrals on the upper and lower branches of the double time contour.

3.5 Interaction with a Bosonic Field and the Two-Body Interaction

Before looking at the higher-order terms in the interaction with a scalar field in the context of disorder averaging, it is worth exploring the interaction with a bosonic field, which physically could correspond to the electron-phonon interaction. In this instance, the simplest interaction Hamiltonian appearing in the S-matrix in Eq. (3.18) is,

$$\tilde{V}_{H_0}(\mathbf{r}, t) = \lambda \int \mathrm{d}\mathbf{r} \phi_{H_0}(\mathbf{r}, t) \psi^\dagger_{H_0}(\mathbf{r}, t) \psi_{H_0}(\mathbf{r}, t), \tag{3.26}$$

where λ is the coupling strength and the bosonic field, $\phi_{H_0}(\mathbf{r}, t)$ (which is a real scalar field in this case), has the additional property that $\langle \phi_{H_0}(\mathbf{r}, t) \rangle = 0$, so that the leading

order correction to the free Green's function is

$$\frac{i}{2}\lambda^2 \int_C \mathrm{d}\tau_1 \mathrm{d}\tau_2 \int \mathrm{d}\mathbf{r}_1 \mathrm{d}\mathbf{r}_2 \langle T_C \phi_{H_0}(\mathbf{r}_1,\tau_1)\phi_{H_0}(\mathbf{r}_2,\tau_2)\rangle \\ \times \langle T_C \psi^\dagger_{H_0}(\mathbf{r}_1,\tau_1)\psi_{H_0}(\mathbf{r}_1,\tau_1)\psi^\dagger_{H_0}(\mathbf{r}_2,\tau_2)\psi_{H_0}(\mathbf{r}_2,\tau_2)\psi_{H_0}(\mathbf{r},t)\psi^\dagger_{H_0}(\mathbf{r}',t')\rangle. \quad (3.27)$$

After performing Wick's theorem and expressing the averages in terms of the free fermionic and bosonic propagators

$$G_0(\mathbf{r},\mathbf{r}',t,t') = -i\langle T_C \psi_{H_0}(\mathbf{r},t)\psi^\dagger_{H_0}(\mathbf{r}',t')\rangle, \quad (3.28)$$

$$D_0(\mathbf{r},\mathbf{r}',t,t') = -i\langle T_C \phi_{H_0}(\mathbf{r},t)\phi_{H_0}(\mathbf{r}',t')\rangle, \quad (3.29)$$

the diagrams (ignoring disconnected diagrams) in Fig. 3.4 can be obtained for the leading order correction to the electronic Green's function (denoting the bosonic propagator with a wavy line). These are the Hartree-Fock diagrams and can be used to highlight a few of the additional rules when dealing with Feynman diagrams. First, each vertex has a factor of λ associated with it and secondly, each of these diagrams has an associated factor of two which cancels the factor of $1/2$ from the expansion of the exponential. This additional factor arises as it is possible to swap the internal vertices and obtain the same diagram. This argument holds at all orders of perturbation theory, so topologically distinct diagrams can be used without worrying about these additional factors [40, 43, 86]. The remaining thing to note about these diagrams is that the tadpole diagram in Fig. 3.4(a) can often be ignored, although not for as simple a reason as a cancellation between the upper and lower branches of the contour. For example, in the case of the electron-phonon interaction this occurs as the diagram corresponds to a translation of the entire lattice which is unphysical [86].

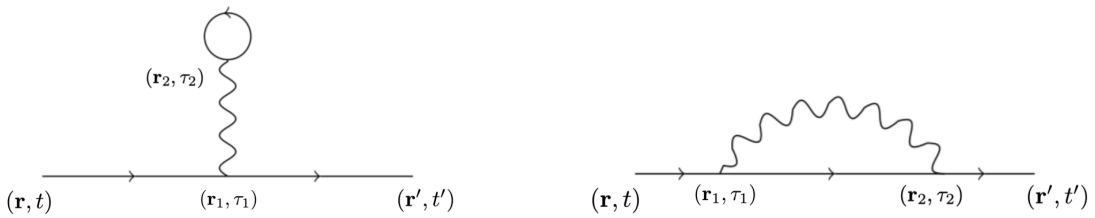

(a) **(b)**

Figure 3.4: The Hartree-Fock diagrams due to interaction with a bosonic field: **(a)** is the Hartree contribution (in this case it is also known as a tadpole diagram) and **(b)** is the Fock contribution.

Before looking at higher-order terms in this expansion, it is worth noting that due to the vanishing of expectation values with an odd number of bosonic operators, the diagrammatic expansion for a two-body interaction (for example the electron-electron Coulomb interaction) is the same. This interaction has the form,

$$\tilde{V}_{H_0}(\mathbf{r}, \mathbf{r}', t, t') = \int \mathrm{d}\mathbf{r} \int \mathrm{d}\mathbf{r}' \, \psi^\dagger_{H_0}(\mathbf{r}, t)\psi^\dagger_{H_0}(\mathbf{r}', t)V(\mathbf{r}, \mathbf{r}', t, t')\psi_{H_0}(\mathbf{r}', t)\psi_{H_0}(\mathbf{r}, t), \tag{3.30}$$

and the corresponding S-matrix contains integrals over two contour variables and upon expansion of this, the same diagrammatic expansion as that for coupling to a bosonic field is obtained except that the wavy line represents the interaction, $V(\mathbf{r}, t)$, rather than the bosonic propagator. Again in this instance, the Hartree digram vanishes in a metallic system due to the cancellation of the diagram with a corresponding one caused by the interaction with the background charge, in other words, it vanishes due to electroneutrality [43, 82].

3.5.1 Self-Energy, the Polarisation Operator and Dyson's Equation

The diagrammatic rules obtained so far can be used to expand the electronic Green's function to higher and higher orders. Calculating these diagrams, however, becomes more and more cumbersome and so a way to incorporate these higher order diagrams is

important. One way to achieve this is via an iterative equation known as Dyson's equation

$$G = G_0 + G_0 \circ \Sigma \circ G, \tag{3.31}$$

where Σ is the self-energy and $\circ$ represents convolution (which is simply the integration over internal vertices). The physical importance of the self-energy will be discussed more in the context of disorder averaging, but often the real part of the self-energy represents a renormalisation of the chemical potential in the system and the imaginary part is related to the decay or scattering of quasiparticles. The challenge of constructing a valid perturbative approach to a problem then resides in constructing the self-energy. For the electron-phonon or electron-electron interactions discussed above, a common way of approximating the self-energy diagrammatically is shown in Fig. 3.5. Upon insertion of this into the Dyson equation, Eq. (3.31), a diagrammatic expansion in terms of one-particle reducible (those that can be cut in two by cutting a single internal fermionic line) and one-particle irreducible diagrams is produced. This approximation made in Fig. 3.5 is sometimes known as the non-crossing approximation [82] due to it not including diagrams with crossing bosonic or interaction lines. These can be incorporated via vertex corrections if necessary [40, 86].

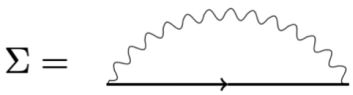

Figure 3.5: The self-energy in the non-crossing approximation. The bold straight line represents the full Green's function.

Further to the expansion of the electronic Green's function, the bosonic propagator or interaction line also has a similar expansion

$$D = D_0 + D_0 \circ \Pi \circ D, \tag{3.32}$$

where the self-energy, Π, in this case, is known as the polarisation operator. This al-

lows for the inclusion of fermion loops (or bubbles) into the interaction and can lead to screening in metals for example. In a weakly interacting metal (relative to the kinetic energy)[3], an appropriate approximation for the polarisation operator is the random phase approximation (RPA), which is displayed in Fig. 3.6.

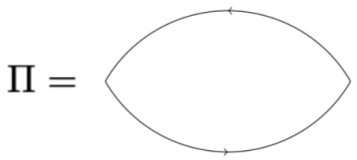

Figure 3.6: The polarisation operator in the RPA for a weakly interacting metal.

By including the full interaction or bosonic propagator (denoted by a bold wavy line) into the electronic self-energy or the full electronic Green's function (denoted by a bold line) into the polarisation operator, better models can be obtained. However, this comes at the cost of further complexity as more terms are included in the diagrammatic expansions and the problem may need to be solved self-consistently.

So far everything has been constructed making use of the contour-ordered Green's function, however this is not the most useful form. In the following section, a transformation to real-time will be carried out which allows the calculation of physical properties.

3.6 Green's Functions

The definition of the contour-ordered Green's function in Eq. (3.20) can lead to different Green's functions depending on whether the time arguments lie on the upper or lower branch of the contour - leading to four possibilities, which can be expressed as a matrix

[3]This is equivalent to a high electron density as by comparing the interaction to kinetic energies, the density parameter, $r_s = \lambda_F/a_B$ is defined where a_B is the Bohr radius. Then, $r_s \ll 1$ in the weakly interacting limit, corresponding to high density.

[43, 82–84],

$$G(x,x') = \begin{pmatrix} G^T(x,x') & G^<(x,x') \\ G^>(x,x') & G^{\tilde{T}}(x,x') \end{pmatrix} = \begin{pmatrix} -i\langle T\psi_H(x)\psi_H^\dagger(x')\rangle & i\langle \psi_H^\dagger(x')\psi(x)\rangle \\ -i\langle \psi_H(x)\psi_H^\dagger(x')\rangle & -i\langle \tilde{T}\psi_H(x)\psi_H^\dagger(x')\rangle \end{pmatrix}, \tag{3.33}$$

where $x = (\mathbf{r}, t)$. Here, G^T is the time-ordered Green's function, where both time arguments lie on the upper branch of the contour so contour ordering becomes equivalent to time-ordering. Similarly, if both time arguments are on the lower branch of the contour, then the anti-time-ordered Green's function, $G^{\tilde{T}}$ can be defined. In contrast to this, if the time arguments are on different branches of the contour, then the contour ordering of operators becomes clear, leading to the greater, $G^>$, and lesser, $G^<$, Green's functions. These latter two Green's functions are often utilised as physical observables can be easily expressed in terms of them. For instance, the average electron density is given by [85]

$$\langle n(\mathbf{r})\rangle = -iG^<(x,x). \tag{3.34}$$

This description of the Green's functions is not always the most appropriate, however and it should be noted that because $G^T + G^{\tilde{T}} = G^> + G^<$, there are actually only three linearly independent Green's functions. A transformation, originally introduced by Larkin and Ovchinnikov [89] can be performed such that Eq. (3.33) becomes[4],

$$\tilde{G}(x,x') = \begin{pmatrix} G^R(x,x') & G^K(x,x') \\ 0 & G^A(x,x') \end{pmatrix}, \tag{3.35}$$

where $G^R = G^T - G^<, G^A = G^T - G^>$ and $G^K = G^< + G^> = G^T + G^{\tilde{T}}$ are the retarded, advanced and Keldysh Green's functions respectively [84]. The retarded and advanced Green's functions can be viewed as describing the response of a particle (or hole for the advanced Green's function) to an applied perturbation. They addition-

[4]The tilde notation is not related to the Fourier transform but is simply used here to distinguish between the two different representations of the Green's function matrix.

ally contain information about the density of states, $\nu(\varepsilon)$, via the spectral function $A(\mathbf{k},\varepsilon) = i(G^R(\mathbf{k},\varepsilon) - G^A(\mathbf{k},\varepsilon)) = i(G^>(\mathbf{k},\varepsilon) - G^<(\mathbf{k},\varepsilon))$ [85],

$$\nu(\varepsilon) = \int \frac{\mathrm{d}^d\mathbf{k}}{(2\pi)^d} A(\mathbf{k},\varepsilon). \tag{3.36}$$

The remaining Green's function above, G^K is the Keldysh Green's function and contains information about the distribution function of the system and in equilibrium can be expressed as [43]

$$G^K(\mathbf{k},\varepsilon) = -iA(\mathbf{k},\varepsilon)(1 - 2f(\varepsilon)), \tag{3.37}$$

where $f(\varepsilon)$ is the standard Fermi function. It is this Keldysh Green's function that becomes particularly relevant in non-equilibrium physics as the distribution function is not guaranteed to be a Fermi function and may also depend on the initial conditions.

3.6.1 Diagrams in Real Time

The diagrammatic approach developed earlier in the chapter was done for a contour-ordered Green's function and it is important to understand how this is altered in real time. Whilst the diagrams themselves remain the same, being able to express them in terms of the real time Green's functions is not a trivial task and for the details Appendix A or [43] should be consulted. Here the main results will be summarised.

In the case of coupling to a scalar potential - see Fig. 3.3 and Eq. (3.25), the analysis is fairly simple. First, the integral along the contour in Eq. (3.25) can be split into a real time integral along the top branch (from $-\infty$ to ∞) and a real time integral along the bottom branch (from ∞ to $-\infty$). If care is taken over whether the temporal arguments are on the upper or lower branches then the result for the first order correction in Eq. (3.25) can be expressed as

$$\int \mathrm{d}x_1 G_0(x,x_1)V(x_1)G_0(x_1,x') \tag{3.38}$$

where the integration is over both the spatial and temporal variables. In this equation,

the variables in the integrand are matrices, with the G's being the free Green's function variant of Eq. (3.33) and $V(x_1) = \langle U(x_1)\rangle\sigma^{(z)}$, where $\sigma^{(z)}$ is the standard Pauli-z matrix. In general, this leads to the Dyson equation [43]

$$G = G_0 + G_0 \circ VG. \tag{3.39}$$

This can be simplified further by performing the Keldysh rotation which leads to the equation

$$\tilde{G} = \tilde{G}_0 + \tilde{G}_0 \circ U\tilde{G}, \tag{3.40}$$

where $U = \langle U\rangle\mathbb{1}$ ($\mathbb{1}$ is the identity matrix). In this instance, the transition to real-time is relatively simple, but in the case of the electron-electron or electron-phonon interactions, this is no longer true.

To illustrate how this works, the diagram in Fig. 3.4(b) will be considered. The first step is to use go from contour-ordering to time ordering, with the intention of writing the equation in a matrix (or tensor) form similar to that in Eq. (3.38). This leads to, after making use of index notation and not explicitly writing the spatial variables,

$$\delta G^{(1)}_{ij} = (G_0)_{im} \circ \Sigma_{mm'} \circ (G_0)_{m'j}, \quad \Sigma_{mm'} = i\gamma^k_{mn}(G_0)_{nn'}(D_0)_{kk'}\gamma^{k'}_{n'm'}, \tag{3.41}$$

where the $\delta G^{(1)}_{ij}$ represents the first order correction to the full Green's function. The self-energy term contains two vertices, one for the emission and one for the absorption of the phonon and these contain the coupling constant λ. In this representation, both vertices have the same matrix structure, given by $\gamma^k_{mn} = \lambda\delta_{mn}\sigma^{(z)}_{nk}$. However, if the Keldysh rotation is performed, this is no longer the case and the two vertices are given by

$$\tilde{\gamma}^1_{mn} = \frac{\lambda}{\sqrt{2}}\delta_{mn}, \qquad \tilde{\gamma}^2_{mn} = \frac{\lambda}{\sqrt{2}}\sigma^{(x)}_{mn} \tag{3.42}$$

$$\bar{\gamma}^1_{mn} = \frac{\lambda}{\sqrt{2}}\sigma^{(x)}_{mn}, \qquad \bar{\gamma}^2_{mn} = \frac{\lambda}{\sqrt{2}}\delta_{mn}, \tag{3.43}$$

where $\tilde{\gamma}^k_{mn}$ is the vertex associated with the emission of a phonon and $\bar{\gamma}^k_{mn}$ is associated with the absorption of a phonon. Each index corresponds to a different line, the k is for the bosonic propagator, the m is for the electronic Green's function entering the vertex, and the n is for the outgoing Green's function and using this allows the diagrams to be calculated without having to expand the S-matrix explicitly. This will be demonstrated in the next section. Although the vertices above become more complicated compared to when absorption and emission had the same form, the advantage of working with the matrix $\tilde{G}$ is that it preserves the form of the Dyson equation [43], given by Eq. (3.31), with the convolution involving integration over the spatial and real temporal variables.

3.6.2 The Polarisation Operator for the Coulomb Interaction

In order to demonstrate how this works in practice, the 3d polarisation operator will be calculated for the Coulomb interaction in the RPA limit where it is approximated to have the form in Fig. 3.6. Remembering that the left-hand side of the diagram is linked to an incoming interaction line and the opposite is true on the right-hand side, the diagram can be expressed as

$$\Pi_{ij} = -i\bar{\gamma}^i_{mn}(\tilde{G}_0)_{nn'}\tilde{\gamma}^j_{n'm'}(\tilde{G}_0)_{m'm} \tag{3.44}$$

where the minus sign arises due to another rule of diagrammatics - that is a fermion loop contributes a minus sign. Calculation of the retarded component of the polarisation operator, $\Pi^R = \Pi_{11}$ (which is relevant for the renormalisation of the interaction) gives

$$\Pi^R(x,x') = -\frac{i}{2}\left[G^R_0(x,x')G^K_0(x',x) + G^K_0(x,x')G^A_0(x',x)\right]. \tag{3.45}$$

This can be easier dealt with in Fourier space[5], giving

$$\Pi^R(\mathbf{q},\omega) = -\frac{i}{2}\sum_{\mathbf{k}}\int\frac{\mathrm{d}\varepsilon}{2\pi}\left[G_0^R(\mathbf{q}+\mathbf{k},\omega+\varepsilon)G_0^K(\mathbf{k},\varepsilon)+G_0^K(\mathbf{q}+\mathbf{k},\omega+\varepsilon)G_0^A(\mathbf{k},\varepsilon)\right] \tag{3.46}$$

$$= -\sum_{\mathbf{k}}\frac{f(\varepsilon_{\mathbf{k}+\mathbf{q}})-f(\varepsilon_{\mathbf{k}})}{\omega-(\varepsilon_{\mathbf{k}+\mathbf{q}}-\varepsilon_{\mathbf{k}})+i\delta}. \tag{3.47}$$

The final summation above can be performed using the fact that for small q ($q \ll k_\mathrm{F}$) the relevant electrons are those close to the Fermi surface due to the difference of the Fermi functions. This leads to the Lindhard function

$$\Pi^R(\mathbf{q},\omega) = -\nu\left(1-\frac{\omega}{2v_\mathrm{F}q}\ln\left|\frac{v_\mathrm{F}q+\omega}{v_\mathrm{F}q-\omega}\right|\right) - i\pi\nu\frac{\omega}{2v_\mathrm{F}q}\Theta(v_\mathrm{F}q-|\omega|), \tag{3.48}$$

where ν is the density of states near the Fermi surface, v_F is the Fermi velocity and $\Theta(x)$ is the standard Heaviside step function. Using the Dyson equation, the renormalised interaction,

$$V(\mathbf{q},\omega) = \frac{1}{V_0^{-1}(\mathbf{q},\omega)-\Pi^R(\mathbf{q},\omega)}, \tag{3.49}$$

is defined in terms of the normal interaction, $V_0(\mathbf{q},\omega) = 4\pi e^2/q^2$ and has two interesting limits. The first is at low frequency, $v_\mathrm{F}q \gg \omega$, where the electrons have time to adjust to any fluctuations. In this instance, the polarisation operator is equal to $-\nu$, giving an interaction

$$V = \frac{4\pi e^2}{q^2+4\pi e^2\nu}, \tag{3.50}$$

which is simply the screening of Coulomb interaction due to the other electrons in the metal, with the screening length being $(4\pi e^2\nu)^{-(1/2)}$. On the other hand, when the frequency is large so that the electrons don't have time to adjust, the interaction becomes

$$V = \frac{4\pi e^2}{q^2}\left(\frac{1}{1-\frac{\omega_\mathrm{p}^2}{\omega^2}}\right), \tag{3.51}$$

[5]A translationally invariant system in thermal equilibrium is assumed. This will be discussed more when disorder averaging is introduced.

where $\omega_{\mathrm{p}}^2 = 4\pi ne^2/m$ is the plasmon frequency. Therefore, at higher frequencies, a new excitation emerges - the plasmon, which is the oscillation of the electron gas with frequency ω_{p}.

In this section, it has been shown how the tools developed using Keldysh field theory can be applied to a physical problem - that is the renormalisation of the Coulomb interaction in a metal.

3.7 Disorder Averaging

The final major topic that will be discussed in regards to perturbation theory here is that of disorder averaging. This is of particular importance in this work because the presence of disorder is crucial in the physics of localisation as was seen in the previous chapter. There are various models of disorder, for example the Anderson tight-binding model in Eq. (2.2). Another common way to explore disorder is with a random potential, $U(\mathbf{r})$ such that $\langle U(\mathbf{r})\rangle = 0$ and $\langle U(\mathbf{r})U(\mathbf{r}')\rangle = K(|\mathbf{r}-\mathbf{r}'|)$, where $K(x)$ is the correlation function related to the fluctuations in the potential [14]. A form of this correlation function that shall be used in this work is the white noise model where the impurities are uncorrelated s-wave scatterers, such that [40]

$$\langle U(\mathbf{r})U(\mathbf{r}')\rangle = \frac{1}{2\pi\nu\tau}\delta(\mathbf{r}-\mathbf{r}'), \tag{3.52}$$

where ν is the density of states at the Fermi surface and τ is the time between collisions. By making use of the perturbative techniques developed above, the effect of disorder on the electronic Green's function can be ascertained, however before exploring the diagrammatics the form of Dyson's equation will be discussed. Recall that Dyson's equation is given by Eq. (3.31), which can be expressed as

$$G(x,x') = G_0(x,x') + \int \mathrm{d}x_1\mathrm{d}x_2 G_0(x,x_1)\Sigma(x_1,x_2)G(x_2,x'). \tag{3.53}$$

In thermal equilibrium, all functions here depend only on the difference of the two time arguments and after disorder averaging (that is averaging over all configurations of disorder), the system becomes translationally invariant, so that the functions additionally become dependent on the difference between the two spatial arguments. Therefore, after Fourier transforming Eq. (3.53), the Dyson equation takes on a simple form

$$G(\mathbf{p},\varepsilon) = G_0(\mathbf{p},\varepsilon) + G_0(\mathbf{p},\varepsilon)\Sigma(\mathbf{p},\varepsilon)G(\mathbf{p},\varepsilon). \tag{3.54}$$

Whilst the Dyson equation holds for the different types of Green's function as shown in the previous section, here the free time-ordered Green's function defined by Eq. (3.5) will be used. The self-energy then consists of the sum of irreducible diagrams, although some don't contribute leading to the first order correction being shown in Fig 3.7(a) and the full self-energy being shown in Fig 3.7(b). Consider the first order correction in Fig 3.7(a),then after disorder averaging, the self-energy can be expressed as

$$\Sigma(\mathbf{r}-\mathbf{r}', t-t') = G_0(\mathbf{r}-\mathbf{r}', t-t')\langle U(\mathbf{r})U(\mathbf{r}')\rangle. \tag{3.55}$$

Upon Fourier transforming and using Eq. (3.52) the self-energy becomes

$$\Sigma(\mathbf{p},\varepsilon) = \frac{1}{2\pi\nu\tau}\int \frac{\mathrm{d}^d\mathbf{p}'}{(2\pi)^d} G_0(\mathbf{p}',\varepsilon) = \frac{1}{2\pi\nu\tau}\int \frac{\mathrm{d}^d\mathbf{p}'}{(2\pi)^d}\frac{1}{\varepsilon - \xi_{\mathbf{p}'} + i\delta\mathrm{sgn}(\xi_{\mathbf{p}'})}, \tag{3.56}$$

where d is the dimensionality. The integration can be performed and taking into account that the relevant electrons exist near the Fermi surface, then

$$\Sigma(\mathbf{p},\varepsilon) = -\frac{i}{2\tau}\mathrm{sgn}(\varepsilon) \implies G(\mathbf{p},\varepsilon) = \frac{1}{\varepsilon - \xi_{\mathbf{p}} + \frac{i}{2\tau}\mathrm{sgn}(\varepsilon)}. \tag{3.57}$$

It turns out that this result also holds after summing relevant diagrams at all orders of perturbation theory. Through consideration of the diagram in Fig 3.7(b), the self-energy

can be expressed as

$$\Sigma(\mathbf{p},\varepsilon) = \frac{1}{2\pi\nu\tau}\int \frac{\mathrm{d}^d\mathbf{p}'}{(2\pi)^d}\frac{1}{\varepsilon - \xi_{\mathbf{p}'} - \Sigma(\mathbf{p}',\varepsilon)}. \tag{3.58}$$

This includes all 'rainbow' diagrams such as that in Fig. 3.8(a), although it does not include a variety of diagrams that are shown in Figs 3.8(b),(c). The reason why will be discussed shortly. In Eq. (3.58) the self-energy is momentum independent (as momentum is integrated over) and so the integration can be performed in the same way as before after making the ansatz that the self-energy is purely imaginary [40]. This leads to the same results as in Eq. (3.57). The ansatz of the self-energy being complex is a suitable one as the real part can simply be absorbed into a renormalised chemical potential so will be ignored throughout this work. The imaginary part provides the lifetime of quasiparticles, or equivalently the scattering time, τ. This is confirmed by Fourier transforming the result in Eq. (3.57) back to real space [40].

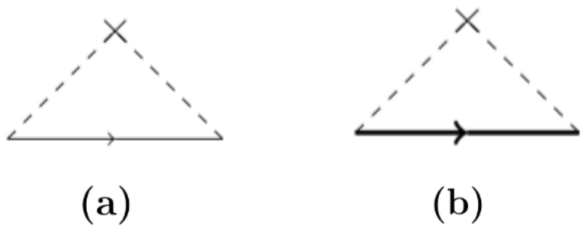

Figure 3.7: The self-energy in the presence of disorder. The thin (thick) solid line represents the free (full) electronic Green's function and the dashed line represents the impurity potential, U. The cross represents that the scattering occurs from the same atom in this model. **(a)**: The first order term in the self-energy. **(b)**: The full self-energy.

Now attention will be turned to the discussion of the diagrams that aren't included (for example, see Figs 3.8(b),(c)) as they provide a significantly smaller contribution to the self-energy. The first diagram to consider is where the electrons just scatter once from a single atom. This just provides a correction to the Fermi energy [40, 44, 86] and so can be set to zero, hence the zero average in the model for disorder. This diagram along with the case where the electrons scatter more than twice from the same atom are

shown in Fig. 3.8(b). The latter diagrams can be included in the self-energy, however, they are much smaller than the ones considered when the Born approximation is used, which is where the scattering potential is considered to be weak. Ignoring these diagrams corresponds to the model of disorder defined by Eq. (3.52).

The only remaining diagrams that haven't been included are the diagrams with crossing impurity lines, such as that in Fig. 3.8(c). In order to see why they can be neglected, it is important to compare the diagrams shown in Fig. 3.8(a) and (c). In both situations, all momenta of the Green's functions must be close to the Fermi surface (within a shell of width $\sim 1/l$). In the first diagram, this can be achieved independently for each momenta meaning that the phase space available is $(4\pi k_{\mathrm{F}}^2/l)^2$. However, in the second diagram, the additional constraint that $\mathbf{p}_2 - (\mathbf{p}_1 - \mathbf{p})$ must be close to the Fermi surface restricts the phase space to a volume, $(4\pi k_{\mathrm{F}}^2/l)(2\pi k_{\mathrm{F}}/l^2)$ - see Fig 3.9. Therefore, the available phase space for the crossing diagram is $\sim k_{\mathrm{F}} l$ smaller than that for those without crossing. In the limit of weak disorder $k_{\mathrm{F}} l \gg 1$, the crossing diagrams can be neglected [40, 44].

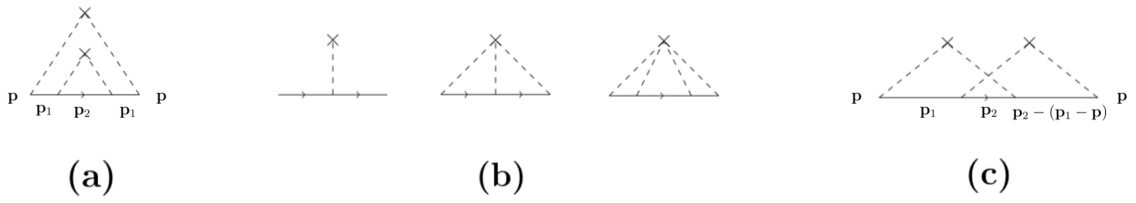

Figure 3.8: A collection of diagrams that can be included in the self-energy with some of the associated momentum arguments in the Green's functions. **(a)**: An example of a 'rainbow' diagram. **(b)**: These diagrams are not included in the self-energy. The first represents a normalisation of the Fermi energy and the remaining two can be neglected in the Born approximation. **(c)**: An example of a diagram with crossing impurity lines. These can be neglected in the limit of weak disorder due to a smaller phase space being accessible.

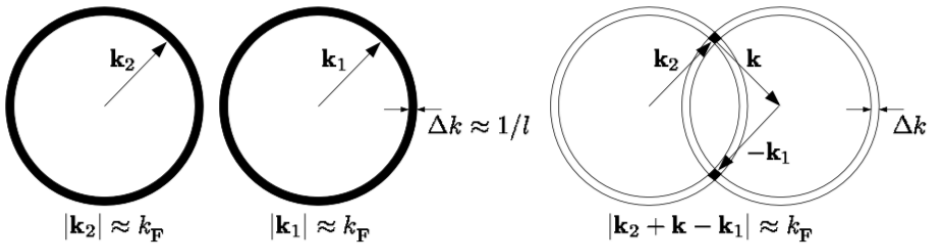

Figure 3.9: Constraints on the momenta in disordered systems. The left corresponds to diagrams with non-crossing impurity lines. Here the condition that momenta are close to the Fermi surface can be satisfied individually for each momenta. When there are crossing impurity lines this is no longer the case, as is shown in the right diagram. Figure taken from [44].

3.7.1 Diffuson and Cooperon

The final objects related to disorder that will be discussed in this chapter are the diffuson and Cooperon. There are two effects in disordered systems that have not yet been considered, the first is diffusion and the second is the interference effects that cause backscattering as was seen during the discussion of weak localisation. The first of these is particularly relevant for this work and is characterised by a particle-hole propagation through the material and the interference between these two channels [82]. In terms of Feynman diagrams, this is shown in Fig. 3.10.

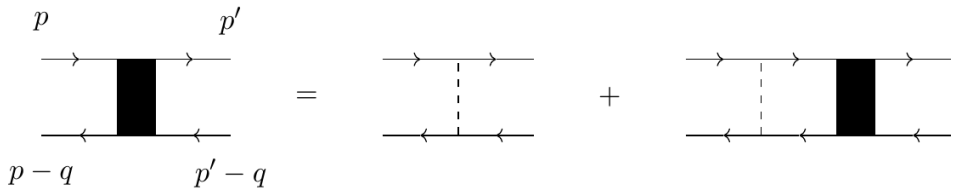

Figure 3.10: The diffuson diagram. The labels represent 4-momenta, for example $p = (\mathbf{p}, E)$.

By making the assumption that the top line in Fig. 3.10 is the retarded Green's function and the lower line is the advanced Green's function (as this will be relevant in the calculations in the next chapter), then after Fourier transforming, the diffuson can be written as

$$\Gamma(\mathbf{q},\omega) = \frac{1}{2\pi\nu\tau} + \frac{1}{(2\pi\nu\tau)^2}\frac{1}{\mathcal{V}}\sum_{\mathbf{p_1}} G^R(\mathbf{p_1},E)G^A(\mathbf{p_1}-\mathbf{q},E-\omega)$$
$$+ \frac{1}{(2\pi\nu\tau)^3}\frac{1}{\mathcal{V}}\sum_{\mathbf{p_1}} G^R(\mathbf{p_1},E)G^A(\mathbf{p_1}-\mathbf{q},E-\omega)\frac{1}{\mathcal{V}}\sum_{\mathbf{p_2}} G^R(\mathbf{p_2},E)G^A(\mathbf{p_2}-\mathbf{q},E-\omega)+\ldots, \tag{3.59}$$

where $\mathcal{V}$ is the d-dimensional volume of the system. The above expression is a geometric series, so that when the integral is performed around the Fermi surface, the result is

$$\Gamma(\mathbf{q},\omega) = \frac{1}{2\pi\nu\tau^2}\frac{1}{-i\omega + Dq^2} \tag{3.60}$$

where $D = v_{\mathrm{F}}^2\tau/d$ is the diffusion constant. This result is valid when multiple scattering events have occurred or in other words, the diffusive limit which corresponds to $ql \ll 1$ and $\omega\tau \ll 1$.

The Cooperon has a similar structure to the diffuson except it has maximally-crossed impurity lines, but if, for example, the bottom line were to be 'reversed' then the same structure as in Fig. 3.10 would arise, except with the bottom line reversed. In other words, this describes the interference in disordered systems for a particle-particle propagator and as a result the Cooperon is crucial in the calculation of the weak localisation correction [43, 90]. However, this will not be considered in any detail here as it is not needed for this work.

3.8 QKE

One way of calculating various quantities using the Keldysh formalism is to use a quantum kinetic equation (QKE). In non-equilibrium situations, there is a difference between the

left and right Dyson's equations, which can be written as

$$G \circ \left(G_0^{-1} - \Sigma\right) = \mathbb{1}, \tag{3.61}$$

$$\left(G_0^{-1} - \Sigma\right) \circ G = \mathbb{1}. \tag{3.62}$$

The reason for this difference in non-equilibrium is that the functions are no longer just dependent on the difference of time arguments, so the order of multiplication matters even after Fourier transforming [43]. These two equations can be used to derive a form of the QKE that resembles the semiclassical Boltzmann equation which is common in condensed matter physics and is used to describe the changing of the distribution function under various conditions. The QKE, which is a generalisation of the Boltzmann equation, can be expressed in many different forms that will be explored in the following chapters.

3.9 Summary

This chapter introduced the Keldysh formalism of non-equilibrium field theory. This makes use of electronic Green's functions that propagate the electron from one point to another. These Green's functions come in various forms, with each one having a different use. Multiple associated techniques were discussed, with a focus on constructing a perturbative approach to understand the effects of interactions and disorder on the Green's function. This is of particular interest in the context of MBL where both effects are important. In the next chapter these techniques will be used to analyse the electron-phonon coupling in disordered systems.

CHAPTER 4

ELECTRON-PHONON DECOUPLING

One of the essential conditions for MBL is the presence of electron-phonon decoupling because without it the system will equilibrate and therefore be in a thermalised state. This electron-phonon interaction is inherent to solid-state systems meaning that the observation of MBL in such systems is difficult and is yet to be achieved. In contrast to this, systems of ultracold atoms have greater control over the isolation of the system from the environment and signatures of MBL have been identified in these systems as was discussed in Chapter 2. However, this doesn't mean there has been no progress towards observing MBL in solid-state systems and in this chapter, this will be demonstrated.

Both the theoretical and experimental aspects of identifying electron-phonon decoupling will be discussed as this phenomenon has been observed on a few occasions. The theoretical aspect of this work will focus on the conditions that are required to observe the decoupling as well as building up a general understanding of the electron-phonon interaction in disordered materials. In addition to this, the link to MBL will be emphasised, in particular how the presence of electron-phonon decoupling is a necessary but not sufficient condition for MBL.

In order to develop further progress in this field, two-dimensional materials will be

explored as the focus of this work. The electron-phonon cooling rate in suspended films will be analysed in detail, making use of the techniques developed in the previous chapter. This analysis forms part of the work that went into the manuscript *Electron-Phonon Decoupling in Two Dimensions* [23], authored by myself and Igor V. Lerner. This manuscript is presented towards the end of this chapter before summarising the key results, the consequences that these have, and how this work can be built on to make progress going forwards.

4.1 Electron-Phonon Decoupling in Thin Films

Various materials have been observed to exhibit jumps of several orders of magnitude in the current-voltage (I-V) characteristics [91–97]. These systems jump between a low resistive state and a high resistive state, leading original explanations to suggest the existence of a superinsulating state [93, 98] - akin to that of a superconducting state. However, this was contested in [99,100] and in 2009 theoretical [101] and experimental [97] evidence suggested an alternative explanation in which an overheated electronic state, where the electrons are decoupled from the phonons, was responsible for the jumps in the I-V characteristics. Previous work suggested that this could be relevant but not the sole explanation, however disorder had not been properly accounted for when coming to this conclusion [92, 101].

In the overheating work of [101], a phenomenological model was developed in which the heat balance equation for the system was considered. The heat into the system is provided by an applied voltage, V, which heats the electronic subsystem but not that of the phonons. The heat from the electrons is then dissipated into the lattice via interactions with phonons and it is assumed that both the electronic and phonon subsystems thermalise individually to a well-defined temperature (T_{el} and T_{ph} for the electrons and phonons respectively). These do not need to be the same however, due to a sufficiently weak electron-phonon interaction. Under these assumptions, the heat balance equation can be

expressed as the power into the system is equal to the power out, giving

$$\frac{V^2}{R(T_{\rm el})} = \dot{\mathcal{E}}, \tag{4.1}$$

where $R(T)$ is the equilibrium resistance and $\dot{\mathcal{E}}$ is the cooling rate due to the electron-phonon interaction. For 3d electronic and phonon subsystems, which is applicable for films on a substrate, it is given by [102–104]

$$\dot{\mathcal{E}} = \frac{4\pi^4}{315}\frac{k_{\rm F} l n_{\rm el}\mathcal{V}}{\hbar^4\Delta_0^4}\left(T_{\rm el}^6 - T_{\rm ph}^6\right). \tag{4.2}$$

In the above equation, $n_{\rm el} = k_{\rm F}^3/3\pi^2$ is the three-dimensional electronic density and $\Delta_0^4 = \hbar^3\rho c_s^5$, with ρ being the material density and c_s is the transverse speed of sound. Substituting the result for the cooling rate in Eq. (4.2) into the heat balance equation, Eq. (4.1), it was subsequently found that the I-V characteristics would exhibit a bistability providing that the resistance had an exponential form,

$$R(T) = R_0 \mathrm{e}^{(T_0/T)^\gamma} \tag{4.3}$$

where R_0 is a temperature-independent constant, $T_0 \sim 1 - 5$K and $\gamma = 1$ gives an Arrhenius resistance [101]. Through a careful analysis of the heat balance equation, Eq. (4.1), the authors of [101] were able to predict a number of phenomena that agreed with the experimental observations, particularly those of the authors in [97] whose results obtained from InO_x films (driven into an insulating state by a magnetic field) are displayed in Fig. 4.1.

First, it was found that below a critical lattice temperature $T_{\rm ph}^{\rm cr} \sim 0.1T_0$, there exists a bistability in the electron temperature for a certain range of applied voltages, see the inset of Fig. 4.1(a). Whilst there are three solutions to the heat balance equation in this region, one of them is unstable as it requires the temperature of the electrons to decrease with increasing applied bias - which is unphysical. The first of the two stable states is

found to be the cold electron state where the electrons are still coupled to the lattice and have approximately the same temperature. The second state is massively overheated compared to the phonon bath, which is indicative of the decoupling that has occurred due to insufficient cooling. By making use of Eq. (4.3) at a temperature T_{el}, the two different temperature states lead to high and low resistive states, and the jumps between the two explain the observed jumps in the I-V characteristics, which are shown in Fig. 4.1(b). Other additional effects that were captured theoretically and experimentally include the variation of the bistability boundaries with the lattice temperature (Fig. 4.1(a)) that leads to the hysteretic jumps in the I-V characteristics, as well as an excluded region of electron temperatures that corresponds to the unstable electron states. The independence of the boundary of the hot electron state on the lattice temperature clearly indicates the system is in a transport regime that does not depend on the phonons.

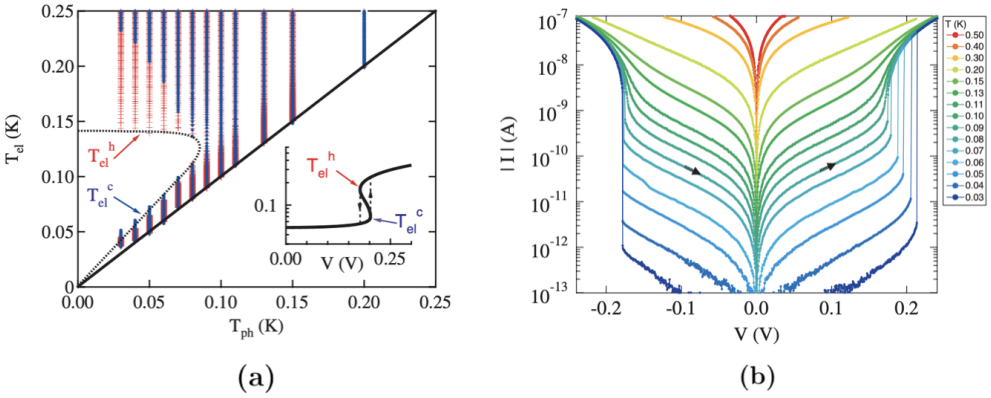

Figure 4.1: The bistability results obtained using InO_x. In **(a)** the bistability is shown in the inset and the main figure shows how the electron temperature varies with the lattice temperature for increasing (blue) and decreasing (red) V. The large jumps in the I-V characteristics are shown in **(b)**. Figure taken from [97].

It is worth noting that whilst this theory and experiment were in good agreement and there has been further work to support the existence of an overheated state [94], this theory did not capture everything and further work has been done. More recent analysis involves the inclusion of localisation, where the effects of a multifractal wave function near

the Anderson transition [105] and the presence of Mott's resonant pairs[1] [53] increase the cooling rate to align it with the experimentally measured value [106]. Prior to this, the theoretically predicted cooling rate was 2-3 orders of magnitude smaller than that in the experiment.

4.1.1 Relation to MBL

Since the work on the overheated state, there have been multiple other studies involving indium oxide films and the I-V jumps, with a particular focus on the experimental [95] and theoretical [107] aspects of the superconductor-insulator transition. More important to the work in this thesis is that a bistability in I-V characteristics has been linked to MBL theoretically [27]. Further studies of indium oxide films have also made this link experimentally [108], although these results are not conclusive. By analysing the particular form of the resistance, the authors of [108] suggested that the conductivity of the sample could be parametrised more accurately by introducing an additional temperature scale, T_c,

$$\sigma(T) \sim \mathrm{e}^{-T_0/(T-T_c)}, \tag{4.4}$$

which suggests the vanishing of the conductivity at $T = T_c$. This finite temperature insulating state is one of the key results of MBL although alone it does not guarantee its existence and the bistability is simply an indication of electron-phonon decoupling which is a requirement for MBL. Therefore, further signatures are needed, an example of which is a divergence in the electronic noise as the MBL transition is approached. The details of this will be discussed further in Chapter 6, however it is worth noting that this has already been explored in indium oxide films [109, 110] and although these works observed enhanced electronic noise they were not conclusive in linking the results to MBL and either further theoretical work, or ideally signatures reflecting the entanglement and lack of thermalisation would be required.

In the work presented in the manuscript *Electron-Phonon Decoupling in Two Dimen-*

[1] These also cause a logarithmic frequency-dependent conductivity in the localised regime [14, 53].

sion [23] at the end of this chapter, the effects of electron-phonon decoupling are explored in two dimensions, which is relevant for the case of suspended thin films. In order to carry out this analysis, it is important to understand the electron-phonon interaction.

4.2 Electron-Phonon Interaction

In a metal the electrons are coupled to the lattice via the phonons (vibrations of the lattice). This interaction arises as the phonons change the local charge density of the lattice, which the electrons then couple to via the Coulomb interaction. If the ions of the lattice are located at positions $\mathbf{R}_j$, then the interaction is given by [86]

$$H_{\text{int}} = \int \mathrm{d}\mathbf{r}\, \psi^\dagger(\mathbf{r})\psi(\mathbf{r}) \sum_i V(\mathbf{r} - \mathbf{R}_i), \tag{4.5}$$

where $\psi^\dagger(\mathbf{r})$ ($\psi(\mathbf{r})$) are the field creation (annihilation) operators for an electron at position $\mathbf{r}$ and $V(\mathbf{r} - \mathbf{R}_i)$ is the potential coupling the electrons and ions. The displacements, $\mathbf{u}_i$ for the ions due to the lattice vibrations are in general small, $|\mathbf{r} - \mathbf{R}_i^{\text{eqm}}| \ll \mathbf{u}_i$, meaning the potential can be expanded around the equilibrium points of the ions, $\mathbf{R}_i^{\text{eqm}}$, giving

$$V(\mathbf{r} - \mathbf{R}_i) \approx V(\mathbf{r} - \mathbf{R}_i^{\text{eqm}}) + \mathbf{u}_i \cdot \nabla V(\mathbf{r} - \mathbf{R}_i^{\text{eqm}}). \tag{4.6}$$

The following observations can be made after substituting this result into Eq. (4.5). The first term is just a constant background potential for the electrons and is the cause of the periodic potential in crystals that leads to the well-known Bloch states for electrons [86]. The second term is the interaction between the electrons and ion displacements - in other words, this is the electron-phonon interaction. This interaction can be expressed in Fourier space in terms of the standard creation and annihilation operators, $c^\dagger, c$,

$$H_{\text{e-ph}} = \frac{i}{\sqrt{\mathcal{V}}} \sum_{\mathbf{p},\mathbf{q}} c^\dagger_{\mathbf{p}+\mathbf{q}} c_{\mathbf{p}} V(\mathbf{q})(\mathbf{q} \cdot \mathbf{u}_{\mathbf{q}}) = \frac{1}{\sqrt{\mathcal{V}}} \sum_{\mathbf{p},\mathbf{q}} c^\dagger_{\mathbf{p}+\mathbf{q}} c_{\mathbf{p}} (\mathbf{g}_{\mathbf{q}} \cdot \mathbf{u}_{\mathbf{q}}), \tag{4.7}$$

where $\mathcal{V}$ is the d-dimensional volume and $\mathbf{u_q}$ is the Fourier transform of the displacement of the ions due to the phonons. In the standard jellium model $V(\mathbf{q}) = C$, where $C = n_{\rm el}/\nu$, with ν being the density of states at the Fermi surface [111]. This gives a deformation potential constant of $C = (2/3)\varepsilon_{\rm F}$ in 3d and $C = \varepsilon_{\rm F}$ in 2d.

In a clean metal, the model described by Eq. (4.7) is sufficient for describing the electron-phonon interaction where only the longitudinal phonons interact with the electrons. This is because they modify the local charge density ensuring the coupling via the Coulomb interaction, whereas the transverse phonons do not, as shown in Fig. 4.2. In disordered systems (which are necessary for studying localisation) there is a further effect that needs to be added to the electron-phonon interaction. In this instance, the impurities can vibrate with the lattice, modifying the interaction and the Hamiltonian acquires an additional term [102–104]

$$H_{\rm e-ph-imp} = -\frac{i}{\sqrt{\mathcal{V}}}\sum_{\mathbf{p},\mathbf{q},\mathbf{k}} c^{\dagger}_{\mathbf{p}+\mathbf{q}+\mathbf{k}} c_{\mathbf{p}} U(\mathbf{k})(\mathbf{k}\cdot\mathbf{u_q}) = \frac{1}{\sqrt{\mathcal{V}}}\sum_{\mathbf{p},\mathbf{q},\mathbf{k}} c^{\dagger}_{\mathbf{p}+\mathbf{q}+\mathbf{k}} c_{\mathbf{p}} (\mathbf{g}^{\rm imp}_{\mathbf{k}}\cdot\mathbf{u_q}). \tag{4.8}$$

Here, $U(\mathbf{k})$ is the Fourier transform of the disorder potential and the sum of Eq. (4.7) and Eq. (4.8) provides the full Hamiltonian for the electron-phonon interaction in disordered systems.

4.3 The Electron-Phonon Cooling Rate

In order to explore the signatures of electron-phonon decoupling in two dimensions, an analysis of the heat balance equation, Eq. (4.1), will be required and therefore the electron-phonon cooling rate must be calculated. Although the main focus of this chapter is on the signatures of electron-phonon decoupling, the electron-phonon cooling rate in 3d disordered systems, Eq. (4.2), has some interesting properties of its own. The first is that it only depends on the transverse phonons. Although the cooling rate due to longitudinal phonons has the same form, the strong dependence on the speed of sound ensures they do not contribute as their speed of sound is a few times larger than the transverse equivalent

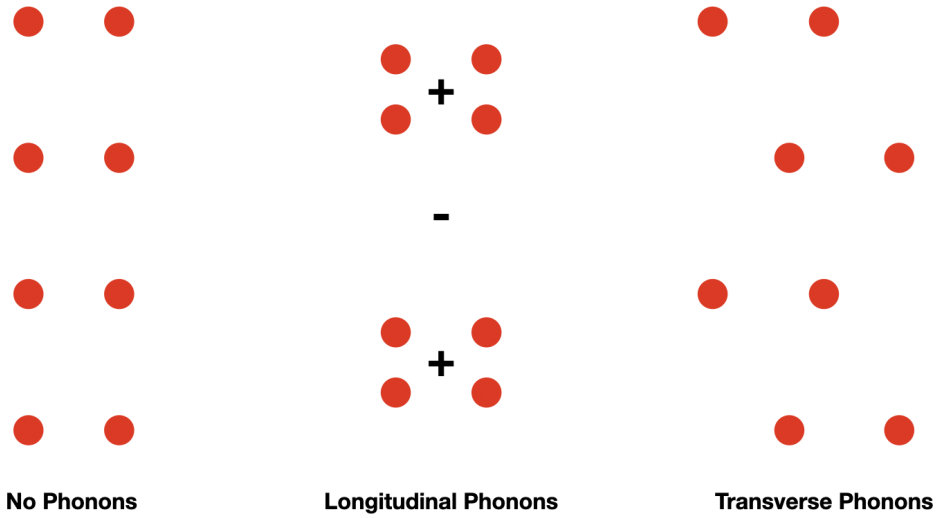

Figure 4.2: The electron-phonon interaction in clean metals. Longitudinal phonons alter the local charge density allowing coupling to the electrons whereas transverse phonons do not.

[112]. Second, the cooling rate in disordered semiconductor systems is suppressed by a factor $n^* lT/\hbar c_s$ compared to a clean metal [101] (n^* is the number of conduction electrons in a unit cell and is small in the systems of interest). This suggests that they are more promising for observing electron-phonon decoupling, although disorder is required for localisation anyway. These phenomena will also be shown to be true in 2d suspended films, but first, it is important to understand how to calculate the cooling rate. One way to achieve this is through the use of the quantum kinetic equation (QKE), which can be written in the form

$$\partial_t f_\varepsilon(t) = I[f_\varepsilon(t)], \tag{4.9}$$

where $f_\varepsilon(t) = 1 - 2n_{\mathrm{F}}(\varepsilon)$ and $n_{\mathrm{F}}(\varepsilon)$ is the standard Fermi distribution function, and $I[f]$ is the collision integral. This form of the QKE is advantageous in this scenario because it allows for a direct calculation of the cooling rate. Through multiplication of both sides of the equation by ε and integration over all energies[2], the left-hand side can be related to the cooling rate of the electrons. By noting that the energy of the electrons in a sample of

[2]The integration is from $-\infty$ to ∞ as measuring energies from the Fermi energy is implicitly assumed.

area $\mathcal{A}$ is given by $\mathcal{E}(T) = \pi^2 \nu \mathcal{A} T_{\mathrm{el}}^2/6$, the expression for the cooling rate can be expressed as

$$\dot{\mathcal{E}} = \frac{1}{2}\nu\mathcal{A}\int_{-\infty}^{\infty} \mathrm{d}\varepsilon \quad \varepsilon I[f_\varepsilon(t)]. \tag{4.10}$$

Clearly in order to calculate the cooling rate a clear understanding of the collision integral is required and this will be discussed in the remainder of this chapter.

4.3.1 The Boltzmann Equation

The form of the QKE in Eq. (4.9) resembles the Boltzmann equation which is commonly used to describe the evolution of the distribution function over time in semiclassical calculations. This distribution function can then be used to calculate various quantities, these range from thermal properties such as the cooling rate above to electrical properties such as the current. The Boltzmann equation is given by [28, 111]

$$\partial_t f(\mathbf{r}, \mathbf{p}, t) + \dot{\mathbf{r}} \cdot \nabla_{\mathbf{r}} f(\mathbf{r}, \mathbf{p}, t) + \dot{\mathbf{p}} \cdot \nabla_{\mathbf{p}} f(\mathbf{r}, \mathbf{p}, t) = I[f]. \tag{4.11}$$

where $f(\mathbf{r}, \mathbf{p}, t)$ is the distribution function and $I[f]$ is the collision integral. In this formalism, there are multiple ways to approach the collision integral, for instance using Fermi's golden rule. The simplest model however, is the relaxation time approximation, which assumes the distribution doesn't deviate too far from equilibrium and the relaxation time, τ is the scattering time. This model has the following form for the collision integral

$$I[f] = -\frac{f(\mathbf{r}, \mathbf{p}, t) - f_0(\mathbf{r}, \mathbf{p})}{\tau}, \tag{4.12}$$

where $f_0(\mathbf{r}, \mathbf{p})$ is the equilibrium distribution and τ is the scattering time, which encapsulates all the scattering processes.

4.3.2 The Quantum Kinetic Equation

The Boltzmann equation can be generalised to the quantum kinetic equation which still allows the incorporation of different scattering processes. There are various ways to express this equation, with one being a similar form to the semiclassical Boltzmann equation, Eq. (4.11), and such a derivation is presented in, for example [43, 83]. In this work, the preferred form is still similar to that of the Boltzmann equation - it is that in [102], which is the form in Eq. (4.9).

The starting points of the derivation are the left and right Dyson equations for the matrix form of the Green's function involving G^R, G^A, G^K (note the $\tilde{G}$ notation used in the previous chapter has been dropped),

$$G \circ \left(G_0^{-1} - \Sigma\right) = \mathbb{1}, \tag{4.13}$$

$$\left(G_0^{-1} - \Sigma\right) \circ G = \mathbb{1}, \tag{4.14}$$

where G_0^{-1} has the same structure as G but contains the inverses of the Green's functions. Upon subtraction this can be written as

$$[G_0^{-1} \circledcirc G] = [\Sigma \circledcirc G]. \tag{4.15}$$

After taking the Keldysh component of this equation, performing a temporal Wigner transform and then integration over the coordinates, $\mathbf{r}$, $\mathbf{r}'$, (which is equivalent to a trace) the QKE can be written as

$$\partial_t f_\varepsilon(t) = \frac{1}{2\pi\nu\mathcal{V}} \operatorname{Tr}\left(\Delta\Sigma G^K - \Sigma^K \Delta G\right), \tag{4.16}$$

where $\Delta G = G^R - G^A$, and $\Delta\Sigma = \Sigma^R - \Sigma^A$. For the details of the derivation see Appendix B.

4.3.3 The Collision Integral

The form of the QKE in Eq. (4.16) is the same as the general form in Eq. (4.9) with $I[f] = \frac{1}{2\pi\nu\mathcal{V}} \mathrm{Tr}\big(\Delta\Sigma G^K - \Sigma^K \Delta G\big)$. In the case of the electron-phonon interaction, which is relevant for the calculation of the cooling rate due to this interaction, the self-energy can be expressed via the diagram shown in Fig. 4.3. Calculation of this diagram can be performed using the techniques developed in the previous chapter (see Appendix B) and then disorder averaging can be performed to give the collision integral [23, 102]

$$I[f] = \frac{i}{4\pi\nu\mathcal{A}} \Big\langle \int_{-\infty}^{\infty} \frac{\mathrm{d}\omega}{2\pi} \int \mathrm{d}\mathbf{r}\mathrm{d}\mathbf{r}' \Delta G(\mathbf{r}, \mathbf{r}', \varepsilon) \hat{g}_\alpha(\mathbf{r}') \Delta G(\mathbf{r}', \mathbf{r}, \varepsilon - \omega) \times \Delta D_{\alpha\beta}(\mathbf{r}' - \mathbf{r}, \omega) \hat{g}_\beta(\mathbf{r}) [(f_\varepsilon - f_{\varepsilon-\omega}) N_\omega + f_\varepsilon f_{\varepsilon-\omega} - 1] \Big\rangle. \tag{4.17}$$

Here, $\Delta D = D^R - D^A$ is the difference between the retarded and advanced components of the phonon propagator, $N_\omega = 1 - 2n_{\mathrm{B}}(\omega)$, with $n_{\mathrm{B}}(\omega)$ being the standard Bose distribution and the g's represent either the clean electron-phonon vertex in Eq. (4.7), or its disordered counterpart in Eq. (4.8).

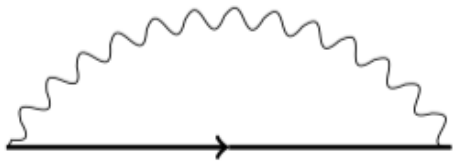

Figure 4.3: The Feynman diagram for the electron-phonon self-energy used in the calculation of the collision integral.

The two different types of vertex in combination with the disorder averaging lead to a variety of diagrams shown in Fig. 4.4 and it is the calculation of these diagrams that allows the electron-phonon cooling rate to be obtained. Subsequent analysis of the heat balance equation allows the conditions under which electron-phonon decoupling occurs

to be derived, as well as the signatures that allow this to be observed in suspended two-dimensional films. This is all discussed, along with the consequences of the results in the next section, where the manuscript *Electron-Phonon Decoupling in Two Dimensions* [23] is presented, with additional details on the calculations being provided in Appendix C.

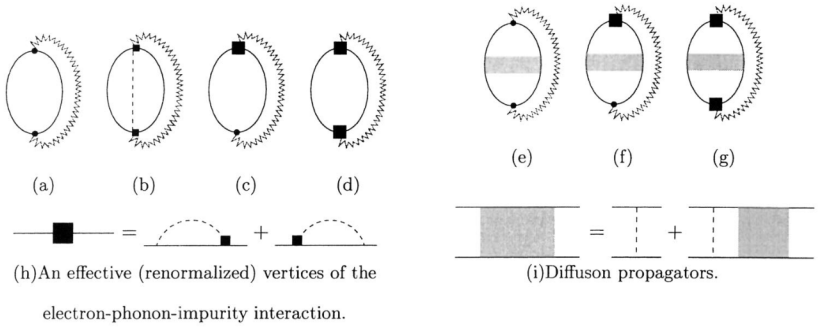

Figure 4.4: The Feynman diagrams for the collision integral after disorder averaging. Small circles correspond to the standard electron-phonon vertex, $\mathbf{g_q}$ and the large circles correspond the disorder modified vertex, $\mathbf{g}_{\mathbf{k}}^{\mathrm{imp}}$. The solid lines indicate disorder averaged electronic Green's functions. Figure taken from [102].

4.4 *Electron-Phonon Decoupling in Two Dimensions*

The following is the manuscript for the publication *Electron-Phonon Decoupling in Two Dimensions* produced by myself and my supervisor Igor V. Lerner. As first author, I performed the calculations and analysed the results. I additionally wrote the majority of the manuscript with assistance on the writing and the direction of the project provided by Igor V. Lerner. A version of this manuscript has been published in Scientific Reports [23].

Electron-Phonon Decoupling in Two Dimensions

George McArdle[1] **and Igor V. Lerner***[1]

[1]University of Birmingham, School of Physics & Astronomy, B15 2TT, UK
*i.v.lerner@bham.ac.uk

ABSTRACT

In order to observe many-body localisation in electronic systems, decoupling from the lattice phonons is required, which is possible only in out-of-equilibrium systems. We show that such an electron-phonon decoupling may happen in suspended films and it manifests itself via a bistability in the electron temperature. By studying the electron-phonon cooling rate in disordered, suspended films with two-dimensional phonons, we derive the conditions needed for such a bistability, which can be observed experimentally through hysteretic jumps of several orders of magnitude in the nonlinear current-voltage characteristics. We demonstrate that such a regime is achievable in systems with an Arrhenius form of the equilibrium conductivity, while practically unreachable in materials with Mott or Efros-Shklovskii hopping.

Introduction

Tremendous experimental progress in isolating quantum many-body systems from the environment (see[1] and[2] for reviews) led to the observation of many-body localization (MBL) in ultracold atomic systems.[3,4] The question remains, however, whether MBL can be observed in disordered electronic systems for which it was originally predicted.[5,6] In the absence of interaction, disorder localizes all electron states in low-dimensional systems[7] so that the dc electronic current vanishes without inelastic processes. The essence of MBL is that inelasticity due to the electron-electron (e-e) interaction alone does not lead to thermal equilibration of the system, as was first suggested for interacting electrons in a chaotic quantum dot.[8] Hence in the absence of other mechanisms of inelasticity all states would remain localized so that finite-temperature conductivity would remain zero.

The main obstacle to the observation of this effect in electronic systems lies in the coupling of the electron system to the environment via the electron-phonon (e-ph) interaction. In equilibrium, such a coupling equilibrates all electron states with the underlying lattice leading to their delocalization. This results in nonzero finite-temperature conductivity, which is driven, in the absence of the electron-electron interaction, by Mott's variable-range hopping[9,10] and given, at temperatures lower than some constant T_0, by

$$\sigma(T) = \sigma_0 \exp\left[-(T_0/T)^{\gamma}\right], \tag{1}$$

where $\gamma = 1/(d+1)$ for a d-dimensional system, and σ_0 is a constant, temperature-independent prefactor. The presence of an electron-electron interaction changes the mechanism of equilibration at sufficiently low temperatures due to the emergence of a so-called Coulomb gap in the single-electron density of states[11] resulting in the change of the exponent in Eq. (1) to $\gamma = 1/2$, independent of dimensionality.

Although the electron-phonon coupling makes it impossible to observe MBL in electronic systems equilibrated with the lattice, in out-of-equilibrium systems electrons and phonons might decouple even in the presence of a weak electron-phonon interaction. For MBL to be observable, the interacting electrons should be at internal equilibrium but not equilibrated with the underlying lattice. It has been suggested[12] that such an out-of-equilibrium decoupling could manifest itself via a bistability in the nonlinear current-voltage (I-V) characteristics. It has been shown later[13] that such a bistability, caused by the electrons overheating, occurs at low temperatures, $T \lesssim 0.1T_0$, provided that the equilibrium conductivity is close to the Arrhenius law, i.e. $\gamma \approx 1$ in Eq. (1). The quantitative description of this bistability,[13] based on an earlier developed analysis of the electron-phonon equilibration rate in bulk disordered systems,[14–16] allowed a full explanation of giant jumps (up to six orders in magnitude) of resistivity experimentally observed[17–20] in various materials with the Arrhenius equilibrium conductivity where T_0 is of order of a few kelvins.

The presence of a bistability in the I-V characteristics below a critical temperature is not, by itself, necessarily a signature of MBL but its absence would mean electron-phonon equilibration and hence the absence of MBL. Intuitively, it seems that the electron-phonon decoupling would be easier to achieve in suspended disordered 2d films. Hence, such films might be promising for observing MBL provided that they are sufficiently disordered for the one-electron Anderson localization on the length scale smaller than the film dimensions.

In this paper, we derive the electron-phonon equilibration rate in such films and use it to analyze a possible bistability of the I-V characteristics on the insulating side where the equilibrium conductivity is governed by Eq. (1). We found that in

suspended films with the Arrhenius equilibrium conductivity, the bistability occurs at lattice temperatures $T \lesssim 0.1T_0$ similar, albeit quantitatively different, to bulk systems or thick multilayered films. On the other hand, for disordered films with $\gamma \lesssim 1/2$, i.e. those with either Mott[9,10] or Efros-Shklovskii[11] conductivity, the bistability could take place at much lower temperatures. Hence only materials with the Arrhenius resistivity at low temperatures could be potentially promising for detecting MBL. While the origin of a small Arrhenius gap, $T_0 \sim 1$K, is quite an interesting problem by itself, we do not consider it here noticing only that there is a variety of materials with such a gap[21–25] which typically have granular disorder.

Model

We consider electron-phonon relaxation in a suspended disordered film where both electron and phonon degrees of freedom are two-dimensional. Electrons can thermally decouple from phonons when a finite source-drain voltage, V, drives the system out of equilibrium. The decoupling might reveal itself in a nonlinear, non-Ohmic regime when the electron-phonon interaction is too weak to effectively dissipate the power supplied to the electron system. Assuming the electron-electron interaction to be sufficiently strong for thermalizing electrons between themselves at a temperature $T_{\rm el}$, the energy dissipation from the electronic system to the phonon bath (or equivalently the lattice), which is at a temperature $T_{\rm ph}$, can be described by the phenomenological heat balance equation,[13]

$$\frac{V^2}{R(T_{\rm el})} = \frac{{\rm d}\mathcal{E}}{{\rm d}t} = \frac{\mathcal{E}(T_{\rm el})}{\tau_{\text{e-ph}}(T_{\rm el})} - \frac{\mathcal{E}(T_{\rm ph})}{\tau_{\text{e-ph}}(T_{\rm ph})}. \tag{2}$$

Here the temperature-dependent part of the total electron energy is given by $\mathcal{E}(T) = \pi^2\nu\mathcal{A}T^2/6$ (where $\mathcal{A}$ is the sample area and ν is the density of states at the Fermi surface), and $R(T_{\rm el})$ is the sample resistance at equilibrium, which is equal to the inverse conductivity $\sigma^{-1}(T_{\rm el})$, see Eq. (1), assuming for simplicity a square shape of the film. As the electron energy is conserved in e-e collisions, the heat balance is fully determined by the e-ph interaction with the scattering time $\tau_{\text{e-ph}}(T)$ which is energy-independent at the low temperatures at which MBL might occur, as the relevant part of the dispersion for both the electrons and phonons is linear. In the presence of disorder, the e-ph interaction is modified by the effect of phonon-induced impurity displacements.[14–16,26] This can occur in two possible ways depending on whether the phonons directly affect the impurities. In the case of a suspended film, the impurities oscillate with the lattice so that the Hamiltonian becomes

$$\mathcal{H} = \frac{1}{\sqrt{\mathcal{A}}} \sum_{\boldsymbol{p},\boldsymbol{q},\boldsymbol{k}} c^\dagger_{\boldsymbol{p}+\boldsymbol{q}+\boldsymbol{k}} c_{\boldsymbol{p}} \left(\boldsymbol{g}_{\boldsymbol{q}} \cdot \boldsymbol{u}_{\boldsymbol{q}}\, \delta_{\boldsymbol{k}\boldsymbol{0}} + \boldsymbol{g}^{\rm imp}_{\boldsymbol{k}} \cdot \boldsymbol{u}_{\boldsymbol{q}} \right). \tag{3}$$

Here $c^\dagger$, c are the electron creation and annihilation operators, $\boldsymbol{u}_{\boldsymbol{q}}$ is the the Fourier transform of the lattice displacement (corresponding to either transverse or longitudinal phonons), $\boldsymbol{g}_{\boldsymbol{q}} = iC\boldsymbol{q}$ is the standard electron-phonon vertex with the deformation potential C equal to the Fermi energy $\varepsilon_{\rm F}$ for two-dimensional phonons, and $\boldsymbol{g}^{\rm imp}_{\boldsymbol{k}} = -iU(\boldsymbol{k})\boldsymbol{k}$ is the vertex corresponding to the phonon-displaced impurities, with $U(\boldsymbol{k})$ being the Fourier transform of the impurity potential. For electron scattering from impurities we assume the standard model of uncorrelated s-scatterers,[27] which is equivalent to the Gaussian potential with zero average and δ-correlations,

$$\langle U(\boldsymbol{r})U(\boldsymbol{r}')\rangle = \frac{1}{2\pi\nu\tau}\delta(\boldsymbol{r}-\boldsymbol{r}'), \tag{4}$$

where τ is the mean scattering time.

Results

We show that electrons can decouple from the phonon bath in thin suspended films provided that the equilibrium finite-temperature conductivity is close to the Arrhenius law, i.e. $\gamma \approx 1$ in Eq. (1), and the bath temperature is much lower than the Arrhenius "gap" T_0. This conclusion is based on our analysis of the electron-phonon cooling rate for 2d phonons similar to that for the phonons in bulk materials (see, e.g.,[14–16]). Using the quantum kinetic equation derived in the Keldysh formalism (see, e.g.,[28]), we derive the following expression for the electron-phonon cooling rate due to transverse phonons:

$$\dot{\mathcal{E}} = \frac{\alpha^2 k_{\rm F}\ell n_{\rm el}\mathcal{A}}{\hbar\Delta_0^3}\left(T_{\rm el}^5 - T_{\rm ph}^5\right), \quad \Delta_0^3 = \hbar^2\rho_{2d}u_{\rm t}^4, \quad \alpha^2 = \frac{3}{\pi}\zeta(5) \approx 0.99, \tag{5}$$

where $k_{\rm F}$ is the Fermi wave vector, ℓ is the electron mean free path, $u_{\rm t}$ is the transverse phonon speed of sound, $n_{\rm el} = k_{\rm F}^2/(2\pi)$ is the 2d electron density, ρ_{2d} is the 2d material density and ζ is the Riemann-zeta function. This result corresponds to the τ-approximation for the e-ph relaxation rate in Eq. (2) with the temperature dependence $1/\tau_{\text{e-ph}}(T) \propto T^3$ and is similar to

that for the case of 3d phonons,[13] where $\dot{\mathcal{E}} \propto T_{\rm el}^6 - T_{\rm ph}^6$, with the difference being caused by the weaker dependence of the phonon density of states on the phonon frequency, which goes as ω^{d-1}. As in the 3d case, the leading contribution to the cooling rate is due to the impurity-facilitated interaction of electrons with transverse phonons, which is absent in a clean metal. The contribution from the interaction with longitudinal phonons has the same form as Eq. (5) with the change $u_{\rm t} \to u_{\rm l}$. Since the longitudinal speed of sound, $u_{\rm l}$, is typically a few times larger than its transverse counterpart,[29] the longitudinal-phonon contribution contains a small factor of $(u_{\rm t}/u_{\rm l})^4$ in comparison to the leading contribution given by Eq. (5). It is worth noting that the overall low-temperature suppression of the e-ph relaxation rate in disordered semiconductors, as compared to a clean metal, is given by a factor of $n^* T\ell/\hbar u_{\rm t}(u_{\rm l}/u_{\rm t})^3$, reflecting Pippard's ineffectiveness condition.[30] Here n^* is the number of electrons per unit cell, which is small in semiconductors most promising for MBL so that, with a typical $u_{\rm t}$ of order of $10^3{\rm m/s}$, the cooling rate could be several orders in magnitude smaller than in a dense clean metal in spite of the factor $(u_{\rm l}/u_{\rm t})^3 \sim 10$.

Next, we substitute the cooling rate (5) into the heat balance equation (2). Assuming the usual Drude prefactor for the equilibrium resistance,

$$R(T_{\rm el}) = R_0 \exp\left[\left(\frac{T_0}{T_{\rm el}}\right)^\gamma\right] \equiv \frac{\hbar k_{\rm F}}{n_{\rm el} e^2 \ell} \exp\left[\left(\frac{T_0}{T_{\rm el}}\right)^\gamma\right], \tag{6}$$

we find that the heat balance equation is independent of the mean free path, ℓ. This allows us to extend the results for the electron-phonon cooling rate we have obtained in the metallic regime, $k_{\rm F}\ell \gg 1$, to the transition regime, $k_{\rm F}\ell \sim 1$, and beyond. This is empirically justified by experiments[20] made in the vicinity of the superconducting-insulating transition, where $k_{\rm F}\ell < 1$, as the results obtained were in excellent quantitative agreement with the results for the bistability[13] obtained using the cooling rate via interactions with bulk phonons which had been calculated in the metallic regime.[14–16]

It is convenient to represent the heat balance equation, obtained by substituting the equilibrium resistance (6) and the cooling rate (5) into Eq. (2), in terms of a dimensionless temperature and voltage, defined by $t_{\rm el,ph} = T_{\rm el,ph}/T_0$ and $v = V/V_0$ with $V_0^2 = \alpha^2 k_{\rm F}^2 \mathcal{A} T_0^5/(e^2\Delta_0^3)$, as follows:

$$v^2 = \left[t_{\rm el}^5 - t_{\rm ph}^5\right] \exp\left[(1/t_{\rm el})^\gamma\right]. \tag{7}$$

For any given voltage, the electron temperature must be higher than the bath temperature to satisfy this equation. By itself this does not signify the electron-phonon decoupling. On the other hand, we can see clear evidence of decoupling in the presence of a bistability where, below a critical bath temperature and in a certain range of the applied voltage, electrons can mutually equilibrate at two distinct temperatures, "cold" $t_{\rm el}^<$ and "hot" $t_{\rm el}^>$. It is in the regime of overheating, at temperature $t_{\rm el}^>$ which is practically independent of the lattice temperature $t_{\rm ph}$, that the electrons become fully decoupled from the phonons.

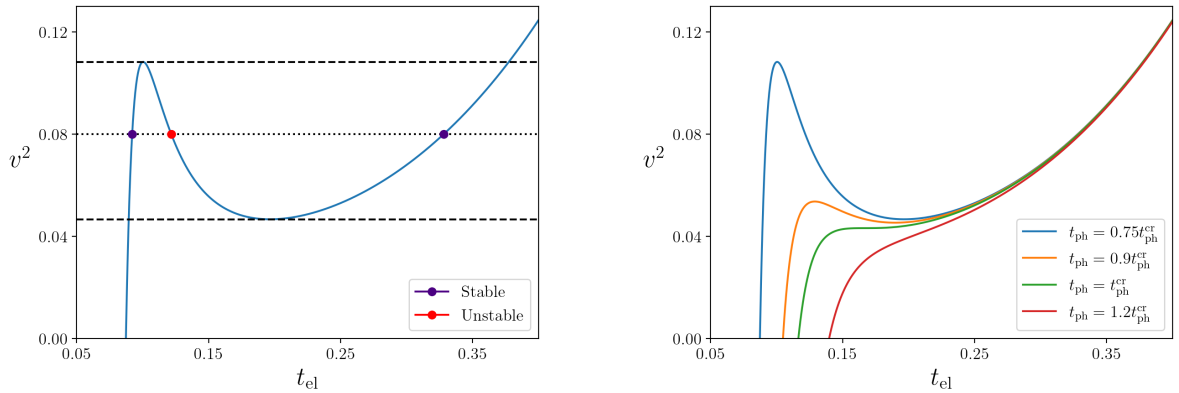

(a) **(b)**

Figure 1. (a). The bistability region, where two stable solutions for $t_{\rm el}$ exist in a certain range of the applied voltage, is shown for $t_{\rm ph} = 0.75t_{\rm ph}^{\rm cr}$ for the Arrhenius equilibrium resistance, $\gamma = 1$. The blue dots correspond to cold and hot electron states at temperatures $t_{\rm el}^<$ and $t_{\rm el}^>$, respectively, and the red dot to an unstable solution. **(b).** The dependence of $t_{\rm el}$ on v^2 for different phonon bath temperatures is shown as follows from Eq. (7). Above the critical bath temperature this corresponds to the actual $t_{\rm el}(v)$ dependence while below $t_{\rm ph}^{\rm cr}$ the electronic system will fall either to $t_{\rm el}^<$ or to $t_{\rm el}^>$, making temperatures in between experimentally inaccessible.

Such a bistability occurs when Eq. (7) has, for a given voltage and bath temperature, two stable solutions for $t_{\rm el}$. This happens below the critical phonon bath temperature $t_{\rm ph}^{\rm cr}$ when the r.h.s. of this equation becomes a non-monotonic function of the electron temperature. An elementary analysis shows that the critical bath temperature is given by

$$t_{\rm ph}^{\rm cr} \equiv \frac{T_{\rm ph}^{\rm cr}}{T_0} = \left(1+\frac{5}{\gamma}\right)^{-\left(\frac{1}{\gamma}+\frac{1}{5}\right)}. \tag{8}$$

For $t_{\rm ph} < t_{\rm ph}^{\rm cr}$ Eq. (7) has three solutions in a certain region of the source-drain voltage, as illustrated in Fig. 1 for the Arrhenius case, $\gamma = 1$. For a given voltage within this region, both the "cold" and "hot" states, at electronic temperatures $t_{\rm el}^{<}$ and $t_{\rm el}^{>}$ respectively, are stable. The middle solution, however, corresponds to an unstable electronic state.

Formally, a similar bistability takes place also for the Mott ($\gamma = 1/3$) and Efros-Shklovskii ($\gamma = 1/2$) hopping regimes. However, a faster than exponential dependence of the critical phonon bath temperature on $1/\gamma$, Eq. (8), pushes the bistability in these regimes to very low temperatures: while $t_{\rm ph}^{\rm cr} \approx 0.12$ in the Arrhenius case, it is about $5\cdot 10^{-3}$ in the Efros-Shklovskii regime, and 10^{-4} in the Mott regime. With $T_0 \sim 1$K in materials of interest, the bistability regime would be practically unreachable in the systems with the Mott or Efros-Shklovskii conductivity, while the experimentally observed bistability in an Arrhenius material[20] was in a quantitative agreement with the theoretical description[13] similar to that developed here but with the electrons interacting with bulk phonons. Due to this fact we conclude that for $\gamma \approx 1$ the bistability occurs for $T \lesssim 0.1T_0$.

At the bistability boundaries for a given $t_{\rm ph}$, the derivative of the r.h.s. of Eq. (7) vanishes, so that the boundaries are determined in the Arrhenius case by the following equation

$$5t_{\rm el} = 1 - (t_{\rm ph}/t_{\rm el})^5, \tag{9}$$

which for $t_{\rm ph} < t_{\rm ph}^{\rm cr}$ has two solutions, hot, $t_{\rm el}^{\rm h}$, and cold, $t_{\rm el}^{\rm c}$, depicted in Fig. 2(a). The corresponding temperature dependence of the voltage boundaries of the bistability, $v^{>}$ for the cold state and $v^{<}$ for the hot one, obtained by substituting $t_{\rm el}^{\rm c,h}$ into Eq. (7), is shown in Fig. 2(b). As previously mentioned, in order to satisfy the heat balance, Eq. (2), the electron temperature must always be higher than the phonon bath. However, while in the cold state $t_{\rm el}^{c}$ almost follows $t_{\rm ph}$, in the overheated hot state $t_{\rm el}^{h}$ is almost independent of the bath temperature, and so is the voltage boundary of this state, $v^{<}$. Since the electrons in the overheated state are practically decoupled from the phonon bath, it is the state most suitable for a possible observation of MBL.

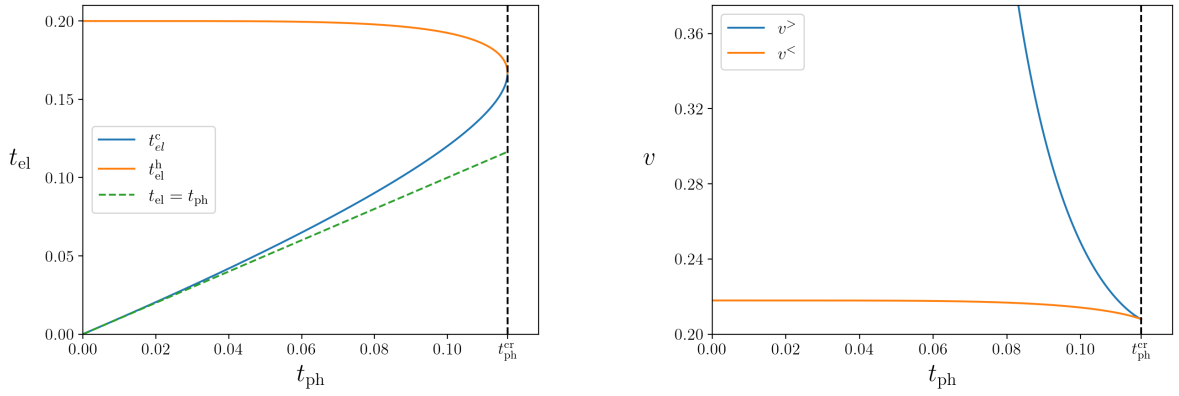

(a) **(b)**

Figure 2. Dependence of the bistability boundaries on the phonon temperature for **(a)** the electron temperature and **(b)** the source-drain voltage, for $\gamma = 1$. The region of electron temperatures inside the curve **(a)** is experimentally inaccessible as it corresponds to the unstable states.

It is important to understand the experimental signatures of the bistability as this will confirm with certainty that electron-phonon decoupling is present. A relatively simple experimental signature is the presence of a region of excluded temperatures corresponding to the unstable states, which are those enclosed by the curve in Fig. 2(a). Such a region was experimentally observed in[20] and turned out to be in quantitative agreement with the theoretical prediction[13] made for films on a substrate with electrons interacting with bulk phonons. But the most striking feature due to bistability is giant hysteretic jumps in the I-V characteristics: due to the exponential dependence of resistance on the inverse electron temperature, a switch between the cold and hot electron states under a given voltage V leads to abrupt changes in the current I that can be of many orders in magnitude.

To see this, we solve numerically the equation for the non-linear conductance in the Arrhenius regime,

$$G = \frac{I}{V} = \frac{1}{R(t_{\rm el})} = \frac{1}{R_0} \mathrm{e}^{-1/t_{\rm el}(v)}, \tag{10}$$

where R_0 is the Drude resistivity, Eq. (6). The solution has an S-shape, as shown in Fig. 3(a), with the dotted part being unstable. This makes hysteretic jumps between the low conductance (cold electron) state and the high conductance (hot electron) state inevitable.

These jumps are illustrated in Fig. 3(b). Let us stress that exact positions of the jumps are random as the boundaries here are simply bounds on the true jumps; where the actual jumps occur depends on the decay mechanisms of the states, as discussed in[13,31]. Moreover, we do not estimate numerical values for these boundaries, because in order to obtain an accurate value for the voltage scale, V_0, we would also need to include the effects of localisation into the electron-phonon cooling rate[32], which goes beyond the aim of this work. Despite this, the temperature dependence of the positions of the jumps should be experimentally observable, as in the case of electrons interacting with bulk phonons.[17–20] Namely, one expects to see a strong temperature dependence of the boundary for the cold electron states ($v^>$) and almost no temperature dependence of the boundary for the hot states ($v^<$), as well as the inaccessible region of electron temperatures as in Fig. 2(a).

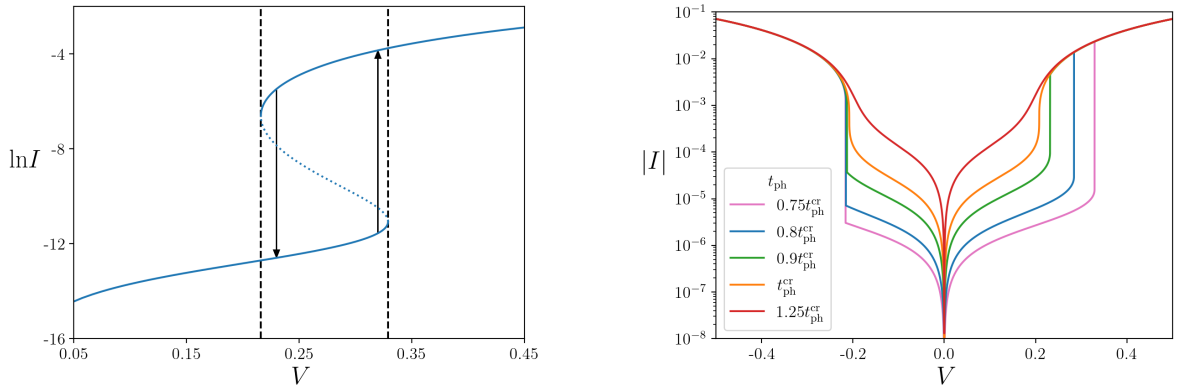

(a) **(b)**

Figure 3. (a). The S-shape solution to the equation for the non-linear conductance, Eq. (10), for $t_{\rm ph} = 0.75t_{\rm ph}^{\rm cr}$. The dotted part corresponds to unstable states, resulting in hysteretic jumps, denoted by the arrows. Note that the jumps do not necessarily occur at the boundaries of the bistability (dashed lines). **(b).** The numerically predicted I-V characteristics for various lattice temperatures. The jumps here are shown to be at the bistability boundaries, though this may not be the case in reality. The $V > 0$ side of the graph illustrates the transition from the cold electron (low conductance) state to the hot electron (high conductance) state, which occurs when the source-drain voltage is increased. The $V < 0$ side displays the opposite transition when the voltage is decreased, going from the hot to cold electron states. In both **(a)** and **(b)** the voltage is measured in units of V_0 and the current is in units such that the resistance is measured in units of R_0.

Discussion

To summarise, we have shown that for films with an equilibrium conductivity exhibiting an Arrhenius (or Arrhenius-like) law, $R(T) = R_0 \exp\left[(T_0/T)^\gamma\right]$ with $\gamma \approx 1$, electrons can decouple from phonons in a nonlinear regime. Such an electron-phonon decoupling manifests itself as a bistability in the electron temperature that can be observed via the I-V characteristics. This bistability occurs in a certain region of source-drain voltages for a lattice temperature $T \lesssim 0.1T_0$, while T_0 is known to be of order of a few kelvins in numerous materials. On the contrary, in systems where the equilibrium conductivity is of the form of either Mott ($\gamma = 1/3$) or Efros-Shklovskii ($\gamma = 1/2$) hopping, the lattice temperature required for the bistability is much lower and practically not accessible. Therefore, for achieving the electron-phonon decoupling necessary for MBL, materials with an Arrhenius conductivity, such as those recently seen in[33], are most promising.

The bistability in the electron temperature means that there exist stable 'cold' and 'hot' electron states. The former have a temperature proportional to (but slightly higher than) that of the lattice while the latter have a temperature which is almost independent of the lattice temperature. It is in this state that the electrons are fully decoupled from the phonons, making it most promising for observing MBL. The most significant experimental signature of the bistability is giant jumps in the non-linear

I-V characteristics between the cold (low conductance) and the hot (relatively high conductance) states. Such jumps have been previously associated, in the 3d case, with a possible transition to MBL[34]. We emphasise, however, that while these jumps provide the evidence for electron-phonon decoupling, further evidence would be needed to confirm the existence of the MBL state.

Methods

In order to calculate the electron-phonon cooling rate in two-dimensional systems, Eq. (5), we used the Keldysh formalism (see, e.g.,[28]) in the form similar to that used in calculating the cooling rate in 3D systems.[16] The quantum kinetic equation can be written as

$$\partial_t f_\varepsilon(t) = I[f], \tag{11}$$

where (after setting $\hbar = 1$) the collision integral for the electron-phonon interaction modified by disorder is given by,[16]

$$I[f] = \frac{i}{4\pi\nu\mathcal{A}} \left\langle \int_{-\infty}^{\infty} \frac{\mathrm{d}\omega}{2\pi} \int \mathrm{d}\boldsymbol{r}\mathrm{d}\boldsymbol{r'} \Delta G(\boldsymbol{r},\boldsymbol{r'},\varepsilon)\hat{g}_\alpha(\boldsymbol{r'})\Delta G(\boldsymbol{r'},\boldsymbol{r},\varepsilon-\omega)\Delta D_{\alpha\beta}(\boldsymbol{r'}-\boldsymbol{r},\omega)\hat{g}_\beta(\boldsymbol{r}) \right. \\ \left. \times[(f_\varepsilon - f_{\varepsilon-\omega})N_\omega + f_\varepsilon f_{\varepsilon-\omega} - 1] \right\rangle. \tag{12}$$

Here the brackets $\langle\cdots\rangle$ stand for averaging over the disorder potential, Eq. (4), $N_\omega = 1 + 2n_B(\omega)$ and $f_\varepsilon = 1 - 2n_F(\varepsilon)$, with $n_B(\omega)$ and $n_F(\varepsilon)$ being the standard Bose and Fermi distributions respectively; $\hat{g}_{\alpha,\beta}$ can be either $\boldsymbol{g_q}$ or $\boldsymbol{g}_{\boldsymbol{k}}^{\mathrm{imp}}$, see Eq. (3); $\Delta G \equiv G^R - G^A$ and $\Delta D \equiv D^R - D^A$ are the differences between the retarded and advanced Green's functions for electrons and phonons, respectively.

The phonon Green's functions are not directly affected by impurities so that their Fourier transforms, which include contributions from the longitudinal, $j = \mathrm{l}$, and transverse, $j = \mathrm{t}$, phonons, $\Delta D_{\alpha\beta}(\boldsymbol{q},\omega) = \sum_j \Delta D^{(j)}_{\alpha\beta}(\boldsymbol{q},\omega)$, are given by the standard expressions

$$\Delta D^{(j)}_{\alpha\beta}(\boldsymbol{q},\omega) = \left[D^R_{\alpha\beta}(\boldsymbol{q},\omega) - D^A_{\alpha\beta}(\boldsymbol{q},\omega)\right]^{(j)} = -\frac{\pi i \eta^{(j)}_{\alpha\beta}}{\rho_{2d}\omega_j(q)} \left[\delta\left(\omega - \omega_j(\boldsymbol{q})\right) - \delta\left(\omega + \omega_j(\boldsymbol{q})\right)\right], \tag{13}$$

where $\eta^{(l)}_{\alpha\beta} = q_\alpha q_\beta/q^2$ and $\eta^{(t)}_{\alpha\beta} = \delta_{\alpha\beta} - q_\alpha q_\beta/q^2$, and we assume the Debye model for the phonon dispersion, $\omega_j(\boldsymbol{q}) = u_j|\boldsymbol{q}|\Theta(q_0 - |\boldsymbol{q}|)$, where q_0 is the Debye momentum.

The disorder-averaged electron Green's functions $G^{R,A}(\boldsymbol{r},\boldsymbol{r'},\varepsilon)$ depend only on the difference of their spatial arguments, and the appropriate Fourier transforms are given by

$$G^{R,A}(\boldsymbol{p},\varepsilon) = \frac{1}{\varepsilon - \xi_{\boldsymbol{p}} \pm i/2\tau}, \quad \xi_{\boldsymbol{p}} = \varepsilon_{\boldsymbol{p}} - \varepsilon_{\mathrm{F}}. \tag{14}$$

A further contribution of disorder in the collision integral (12) is described by vertex corrections. Including only the leading transverse phonons contribution, these corrections are shown in the metallic regime, $k_{\mathrm{F}}\ell \gg 1$, in Fig.4. In the absence of disorder, transverse phonons do not alter the local charge density and so cannot couple directly to the electrons. However, in disordered materials they contribute via the vertices $\boldsymbol{g}_{\boldsymbol{k}}^{\mathrm{imp}}$, Eq. (3), which describe the effect of phonon-induced impurity displacements.

The longitudinal-phonons contribution to the cooling rate turns out to be functionally the same as that of the transverse phonons, given in Eq. (5), with u_{l} substituted for u_{t}. It is much smaller as $(u_{\mathrm{t}}/u_{\mathrm{l}})^4 \ll 1$. Note that this contribution, which exists also in clean systems, involves more cumbersome diagrams that include diffuson propagators similar to the 3d case.[16] We do not give any further detail of calculating the longitudinal-phonons contribution as it is not relevant for the final results.

The calculation of the diagrams depicted in Fig. 4 is relatively straightforward. We assume that the electron-electron interaction is sufficiently strong such that the electrons mutually thermalise and can be assigned a single temperature, T_{el} which is higher than the phonon bath (lattice) temperature, T_{ph}. This results in a quasi-equilibrium situation where $f_\varepsilon = \tanh(\varepsilon/2T_{\mathrm{el}}(t))$ and $N_\omega(T_{\mathrm{ph}}) = \coth(\omega/2T_{\mathrm{ph}})$. Then the spatial integral in Eq. (12) is calculated after the Fourier transform and using the fact that $q_T\ell \ll 1$ (where $q_T \sim T/u_{\mathrm{t}}$ is a typical phonon momentum at temperature T) and the identity $f_\varepsilon f_{\varepsilon-\omega} - 1 = -N_\omega(T_{\mathrm{el}})(f_\varepsilon - f_{\varepsilon-\omega})$, one reduces the collision integral to

$$I[f] = \int \mathrm{d}\omega\, K(\omega)\left[N_\omega(T_{\mathrm{ph}}) - N_\omega(T_{\mathrm{el}})\right]\left[(f_{\varepsilon+\omega} - f_\varepsilon) + (f_{\varepsilon-\omega} - f_\varepsilon)\right], \tag{15}$$

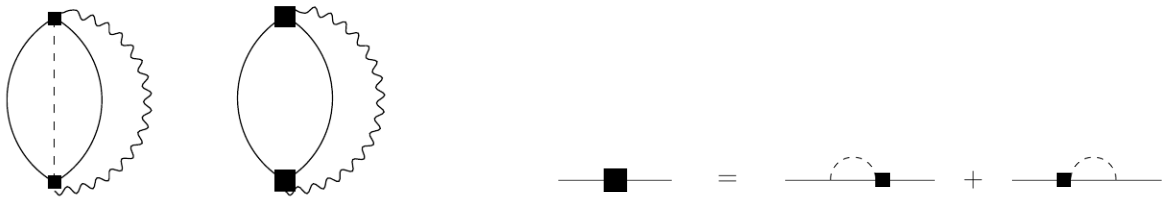

Figure 4. The two lowest-order diagrams that contribute to the collision integral in Eq. (12) due to the interaction of electrons with transverse phonons via impurity scattering: the smaller squares correspond to $g_{\boldsymbol{k}}^{\mathrm{imp}}$, the straight lines are the electron Green's functions, the wavy lines are the phonon Green's functions and the dashed lines describe the standard averaging over impurities.

where $K(\omega)$ is expressed in terms of a dimensionless electron-phonon coupling constant, $\beta_t = \dfrac{\nu\varepsilon_{\mathrm{F}}^2}{2\rho_{2d}u_{\mathrm{t}}^2}$, as

$$K(\omega) = \frac{\beta_t \,\mathrm{sgn}(\omega)}{8k_{\mathrm{F}}\ell}\left(\frac{\omega\ell}{u_{\mathrm{t}}}\right)^2. \tag{16}$$

Substituting the result of Eq. (15) into Eq. (11) and multiplying both sides by ε, one finds after integrating with to respect to ε that the cooling rate (restoring factors of $\hbar$) is given by

$$\dot{\mathcal{E}} = \frac{k_{\mathrm{F}}\ell n_{\mathrm{el}}\mathcal{A}}{\hbar\Delta_0^3}\int_0^\infty \frac{d\omega}{16\pi}\omega^4\left[\coth\left(\frac{\omega}{2T_{\mathrm{el}}}\right) - \coth\left(\frac{\omega}{2T_{\mathrm{ph}}}\right)\right], \qquad \Delta_0^3 = \hbar^2\rho_{2d}u_{\mathrm{t}}^4 \tag{17}$$

Performing the integration leads to the result in Eq. (5).

Acknowledgments

We gratefully acknowledge support from EPSRC under the grant EP/R029075/1. We thank V. I. Yudson for useful comments.

References

1. Bloch, I., Dalibard, J. & Zwerger, W. Many-body physics with ultracold gases. *Rev. Mod. Phys.* **80**, 885–964 (2008).
2. Abanin, D. A., Altman, E., Bloch, I. & Serbyn, M. Colloquium: Many-body localization, thermalization, and entanglement. *Rev. Mod. Phys.* **91**, 021001 (2019).
3. Schreiber, M. *et al.* Observation of many-body localization of interacting fermions in a quasirandom optical lattice. *Science* **349**, 842 (2015).
4. Lüschen, H. P. *et al.* Signatures of many-body localization in a controlled open quantum system. *Phys. Rev. X* **7**, 011034 (2017).
5. Basko, D. M., Aleiner, I. L. & Altshuler, B. L. Metal-insulator transition in a weakly interacting many-electron system with localized single-particle states. *Ann. Phys.* **321**, 1126 (2006).
6. Gornyi, I. V., Mirlin, A. D. & Polyakov, D. G. Interacting electrons in disordered wires: Anderson localization and low-t transport. *Phys. Rev. Lett.* **95**, 206603 (2005).
7. Abrahams, E., Anderson, P. W., Licciardello, D. C. & Ramakrishnan, T. V. Scaling theory of localization: Absence of quantum diffusion in two dimensions. *Phys. Rev. Lett.* **42**, 673 (1979).
8. Altshuler, B. L., Gefen, Y., Kamenev, A. & Levitov, L. S. Quasiparticle lifetime in a finite system: a nonperturbative approach. *Phys. Rev. Lett.* **78**, 2803 (1997).
9. Mott, N. F. Conduction in non-crystalline systems. 1. localized electronic states in disordered systems. *Philos. Mag.* **17**, 1259 (1968).
10. Mott, N. F. & Davis, E. A. Conduction in non-crystalline systems. 2. metal-insulator transition in a random array of centres. *Philos. Mag.* **17**, 1269 (1968).

11. Efros, A. L. & Shklovskii, B. I. Coulomb gap and low temperature conductivity of disordered systems. *J. Phys.* C **8** (1975).

12. Basko, D. M., Aleiner, I. L. & Altshuler, B. L. Possible experimental manifestations of the many-body localization. *Phys. Rev.* B **76**, 052203 (2007).

13. Altshuler, B. L., Kravtsov, V. E., Lerner, I. V. & Aleiner, I. L. Jumps in current-voltage characteristics in disordered films. *Phys. Rev. Lett.* **102**, 176803 (2009).

14. Reizer, M. Y. & Sergeev, A. V. Electron-phonon interaction in impure metals and superconductors. *Zh. Eksp. Teor. Fiz.* **90**, 1056 (1986).

15. Sergeev, A. & Mitin, V. Electron-phonon interaction in disordered conductors: Static and vibrating scattering potentials. *Phys. Rev. B* **61**, 6041–6047 (2000).

16. Yudson, V. I. & Kravtsov, V. E. Electron kinetics in isolated mesoscopic rings driven out of equilibrium. *Phys. Rev.* B **67**, 155310 (2003).

17. Sambandamurthy, G., Engel, L. W., Johansson, A., Peled, E. & Shahar, D. Experimental evidence for a collective insulating state in two-dimensional superconductors. *Phys. Rev. Lett.* **94**, 017003 (2005).

18. Fistul, M. V., Vinokur, V. M. & Baturina, T. I. Collective cooper-pair transport in the insulating state of Josephson-junction arrays. *Phys. Rev. Lett.* **100**, 086805 (2008).

19. Vinokur, V. M. *et al.* Superinsulator and quantum synchronization. *Nature* **452**, 613 (2008).

20. Ovadia, M., Sacépé, B. & Shahar, D. Electron-phonon decoupling in disordered insulators. *Phys. Rev. Lett.* **102**, 176802 (2009).

21. Kowal, D. & Ovadyahu, Z. Disorder-induced granularity in an amorphous superconductor. *Sol. State Commun.* **90**, 783 (1994).

22. Gantmakher, V. F., Golubkov, M. V., Lok, J. G. S. & Geim, A. K. Giant negative magnetoresistance of semi-insulating amorphous indium oxide films in strong magnetic fields. *ZhETF* **109**, 1765 (1996).

23. Sambandamurthy, G., Engel, L. W., Johansson, A. & Shahar, D. Superconductivity-related insulating behavior. *Phys. Rev. Lett.* **92**, 107005 (2004).

24. Dubi, Y., Meir, Y. & Avishai, Y. Nature of the superconductor-insulator transition in disordered superconductors. *Nature* **449**, 876–880 (2007).

25. Hen, B., Zhang, X., Shelukhin, V., Kapitulnik, A. & Palevski, A. Superconductor-insulator transition in two-dimensional indium-indium-oxide composite. *Proc. Natl Acad. Sci. USA* **118** (2021).

26. Schmid, A. Dynamics of electrons in an impure metal. *Z. Phys.* **271**, 251 (1974).

27. Abrikosov, A. A., Gor'kov, L. P. & Dzyaloshinskii, I. E. *Methods of Quantum Field Theory in Statistical, Physics* (Pergamon Press, New York, 1965).

28. Rammer, J. & Smith, H. Quantum field-theoretical methods in transport theory of metals. *Rev. Mod. Phys.* **58**, 323 (1986).

29. Ptitsina, N. G. *et al.* Electron-phonon interaction in disordered metal films: The resistivity and electron dephasing rate. *Phys. Rev. B* **56**, 10089 (1997).

30. Kittel, C. *Quantum Theory of Solids* (John Wiley & Sons, Inc., United States of America, 1987), 2nd edn.

31. Doron, A. *et al.* Instability of insulators near quantum phase transitions. *Phys. Rev. Lett.* **119**, 247001 (2017).

32. Feigel'man, M. V. & Kravtsov, V. E. Electron-phonon cooling power in Anderson insulators. *Phys. Rev. B* **99**, 125415 (2019).

33. Gul, Y., Myronov, M., Holmes, S. & Pepper, M. Activated and metallic conduction in p-type modulation-doped Ge-Sn devices. *Phys. Rev. Applied* **14**, 054064 (2020).

34. Ovadia, M. *et al.* Evidence for a finite-temperature insulator. *Sci. Rep.* **5**, 13503 (2015).

4.5 Summary

In this chapter, a detailed account of electron-phonon decoupling in thin films was presented. By starting with the consideration of films on a substrate and the observed jumps in the I-V characteristics, it was seen how this is an indication of electron-phonon decoupling. Similar signatures can be observed in two-dimensional suspended films provided that the equilibrium conductivity of the film has an Arrhenius form and the temperature is sufficiently low. These signatures are hysteretic jumps of several orders of magnitude in the I-V characteristics and an excluded region of electron temperatures. The hysteresis is caused by a difference in behaviour of the bistability boundaries with variations in lattice temperature. The boundary for the hot electron state is almost independent of the phonon temperature, indicating that in this state the electrons and phonons are decoupled. In the search for MBL in solid-state setups, this allows for the identification of materials that have electron-phonon decoupling. Potential candidates include GeSn [113] and graphene [114]. However, it should be emphasised that whilst this bistability has been linked to MBL [27, 108], it is not a guarantee of localisation and should instead be viewed as a necessary but sufficient condition for MBL. Further signatures of any MBL behaviour should be sought, such as a divergence in the electronic noise [27] which will be discussed in Chapter 6.

CHAPTER 5

QUANTUM DOTS - ASYMMETRIC COUPLING TO THE LEADS

The previous chapter demonstrated how in electronic systems electron-phonon decoupling can be observed via a bistability in the electron temperature which causes jumps of several orders of magnitude in the I-V characteristics, although this is not an indication of MBL itself. Quantum dots provide a suitable way to study electronic noise, a potential signature of MBL, as they undergo a transition analogous to that of many-body localisation. In particular, the concept of localisation in Fock space is important. The next two chapters will focus on understanding quantum dots - why they are a useful model, how they relate to MBL, and how the absence of thermalisation can be understood and detected in these systems.

5.1 The Coulomb Blockade

Quantum dots are 'zero-dimensional' devices which can have a large degree of control exerted over them due to the use of gate voltages and where interactions play a key role resulting in interesting physics (see [8, 36, 115] for reviews). Additionally, they can

be made to exhibit diffusive-like behaviour either through the addition of impurities or by reducing the coupling to the leads so that the electrons scatter off the boundaries of the dot multiple times before escaping. This latter regime is more common and is known as a chaotic quantum dot [115]. It is characterised by the separation of energy scales $\Gamma \ll E_{\mathrm{Th}}$, where Γ is the tunnelling rate to the leads and the Thouless energy, $E_{\mathrm{Th}} \sim v_{\mathrm{F}}/L$, is the inverse of the time to traverse a dot of linear dimension, L. The tunnelling rate is also important in defining an open or closed dot. In an open dot, the coupling of the leads allows for electrons to easily tunnel between the dot and leads and the Coulomb interaction between electrons on the dot is unimportant. However, in the opposite case of a closed dot where the coupling to the leads is weaker, the effect of the interactions is more prevalent and leads to the phenomenon of the Coulomb blockade. This is where the dot has a capacitance, C, so that there is a charging energy, $E_{\mathrm{c}} = e^2/C$, due to the Coulomb interaction that needs to be overcome in order to add electrons onto the dot.

There are two different characterisations of the Coulomb blockade regime. The classical Coulomb blockade considers the regime where the energy levels on the dot (with an average spacing Δ) are smeared by the temperature, T, such that [36]

$$\Gamma \ll \Delta \ll T \ll E_{\mathrm{c}}, \tag{5.1}$$

whereas the quantum Coulomb blockade regime swaps the order of Δ and T, such that the discreteness of the levels becomes important. It is the regime dictated by Eq. (5.1) that is relevant in this work. Including the additional limit of large dimensionless conductance, $g = E_{\mathrm{Th}}/\Delta \gg 1$, the Hamiltonian can be written as [8, 36, 115]

$$H = \sum_n \varepsilon_n d_n^\dagger d_n + \frac{E_{\mathrm{c}}}{2}\left(\hat{N} - N_g\right)^2, \tag{5.2}$$

where $d_n^\dagger(d_n)$ creates (annihilates) an electron on the dot with energy ε_n and N_g is the number of electrons on the dot set by the gate voltage. It is worth noting that in the

derivation of this, two other types of interaction are neglected - these are the spin exchange interaction and the Cooper interaction [8, 116]. The first of these describes the difference in energy between spins that are parallel or anti-parallel. The typical energy scale for this is smaller than the mean energy spacing, so this interaction can be ignored. The Cooper interaction is what is responsible for superconductivity and gets renormalised to zero if it is repulsive (which is what will be considered here) [8,116]. Nevertheless, the Hamiltonian in Eq. (5.2) leads to a lot of interesting phenomena via the Coulomb blockade. The first of these is peaks in the conductance as a function of gate voltage, see Fig. 5.1. Defining $E_N = E_{\rm c}(N - N_g)^2/2$, the energy to add an electron to the dot is

$$\Omega_N \equiv E_{N+1} - E_N = E_{\rm c}\Big(N + \tfrac{1}{2} - N_{\rm g}\Big), \tag{5.3}$$

so that when $N_g = N + \frac{1}{2}$, the energy difference is zero and an electron can be added to the dot even in linear response. This leads to a peak in the differential conductance with the peak shape being given by [25, 117–119],

$$G = \frac{e^2}{2\Delta}\frac{\Gamma_{\rm L}\Gamma_{\rm R}}{\Gamma}\frac{\frac{\beta}{2}(\Omega_N + \varepsilon_{\rm F} - \mu)}{\sinh\big(\frac{\beta}{2}(\Omega_N + \varepsilon_{\rm F} - \mu)\big)}, \tag{5.4}$$

where $\varepsilon_{\rm F}, \mu$ are the Fermi energies for the dot and leads respectively and $\Gamma = \Gamma_{\rm L} + \Gamma_{\rm R}$ is the tunnelling rates for the left and right leads. In the valleys of conductance, $\Omega_N \approx E_{\rm c}/2$, and so an electron cannot be added in linear response and the conductance vanishes.

The presence of the charging energy also has an impact on the non-equilibrium regime as an electron can only be added to the dot when the bias voltage is increased by an amount comparable to the charging energy. This leads to a staircase in the I-V characteristics [9, 117, 121] and it is precisely this staircase that will be explored in this chapter as its presence and form may be able to provide a signature of the absence of thermalisation in a quantum dot.

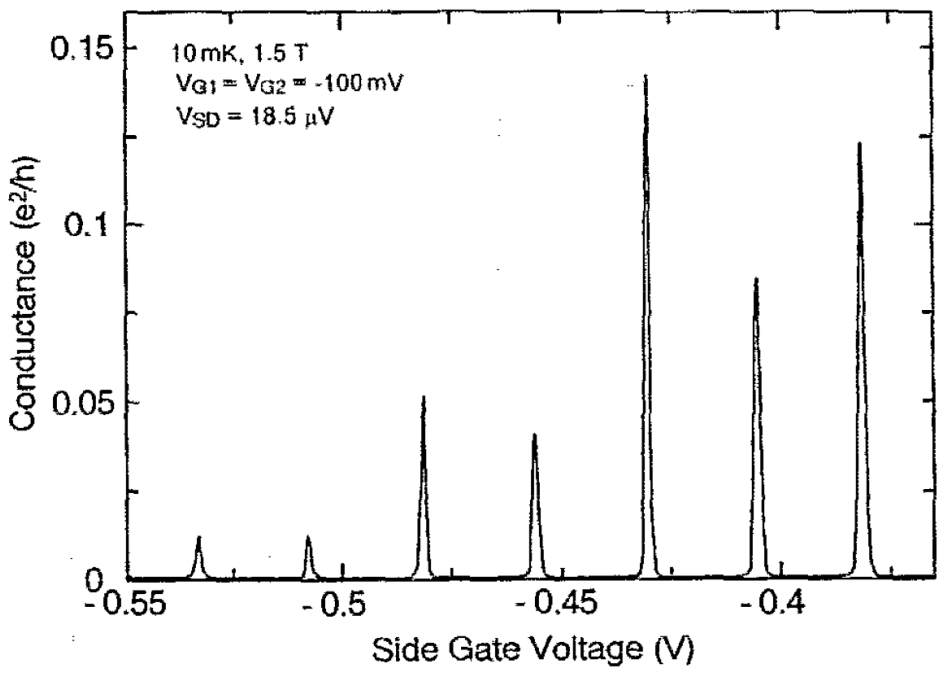

Figure 5.1: The peaks in the conductance of a quantum dot as a function of the gate voltage. Figure taken from [120].

5.2 Relaxation and Localisation in Quantum Dots

The absence of thermalisation on a dot occurs when the relaxation rate, γ, is much smaller than the tunnelling rate,

$$\gamma \ll \Gamma, \tag{5.5}$$

as this corresponds to the electrons tunnelling off the dot before they thermalise. Whilst this regime is applicable for a wide range of energies, it is of particular interest in this work because in the case of localisation $\gamma \to 0$.

Understanding the relaxation rate in quantum dots was clearly addressed by the authors of [122], where it was found that the quasiparticles on a quantum dot decay due to the electron-electron interaction according to the rate

$$\gamma(\varepsilon) \approx \Delta \left(\frac{\varepsilon}{E_{\mathrm{Th}}} \right)^2. \tag{5.6}$$

This result was also supported in subsequent works [123]. The above expression for

the relaxation rate is applicable provided that $\sqrt{g}\Delta < \varepsilon < E_{\mathrm{Th}}$, with the lower bound ensuring that the quasiparticles are well-defined [24], which is necessary to ensure that Fermi's golden rule holds - as is the case in the result in Eq. (5.6). At lower quasiparticle energies this no longer remains true and a different approach must be taken. This was done by Altshuler *et. al.* [24] when they considered the decay of quasiparticles in Fock space as a problem on a Cayley tree[1]. Through careful consideration of the coupling between the single-particle excitation and the many-particle states that the excitation can decay to, as well as the density of states at each level of the decay, they found that below a certain energy, there is localisation in Fock space.

In the localised regime, the initial excitations are weakly coupled to all the other levels of the decay and therefore the full many-body states are just comprised of the single-particle excitations. This is in direct contrast to the extended regime considered in [122], where the single-particle states are coupled to all many-particle states (see Fig. 5.2) and so the peak is broadened to a width, $\gamma(\varepsilon)$ given by Eq. (5.6). In terms of the Cayley tree picture, this covers two possibilities. First, where the whole tree is explored (delocalised and ergodic) and second, where almost none of the tree is explored (localised and non-ergodic). An intermediate regime also exists whereby there is delocalisation but not all of the tree is covered and this leads to a delocalised but non-ergodic regime. This intermediate regime was also later identified in MBL [124–127] and consequently the localisation in quantum dots, although it does not have all the same structure as MBL, acts as a good precursor.

[1]A Cayley tree is a structure where each vertex has a constant number of branches emerging from it. In [24] the branching number represents the number of ways a decay can occur at each level of the overall decay process and is proportional to g^3.

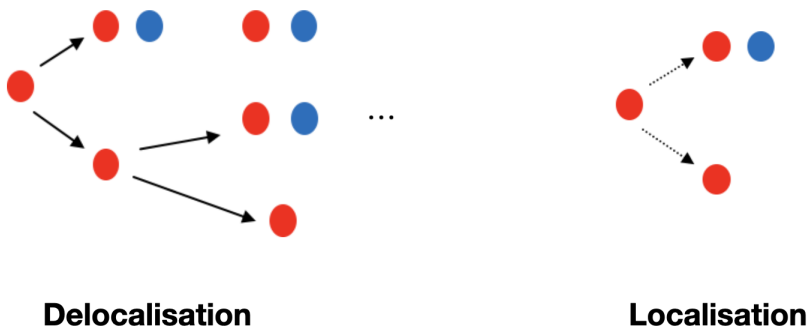

Figure 5.2: Localisation and delocalisation in Fock space. The red circles indicate electrons and the blue circles are holes. In the delocalised and ergodic regime, the single particle excitation is coupled to all states at every order of the decay. In the localised and non-ergodic regime, there is only weak coupling (indicated by the dotted arrow) to the three-particle state and decay of the excitations does not occur.

This work about localisation in quantum dots has been built on in many instances since with a focus on the transition. For example the statistics of energy levels [128] and fluctuations in the local density of states [129] have been studied, but perhaps more important is the identification of the energy at which the localisation-delocalisation transition occurs. Both analytical and numerical arguments now support the transition occurring at a quasiparticle energy of

$$\varepsilon_{\mathrm{cr}} = \Delta \frac{g}{\ln g}, \tag{5.7}$$

which is different from the initial estimates [130]. The fact that the dots undergo this transition in Fock space means they are a suitable model to explore the effects of localisation and may provide insight into spatially extended MBL. Therefore, the rest of this chapter will be used to explore the non-equilibrium properties of quantum dots, namely the Coulomb staircase and how this can be used to identify the absence of thermalisation - a regime important when the electrons are localised.

5.3 The Coulomb Staircase and the Classical Master Equation

The Coulomb blockade manifests itself in the non-equilibrium regime when a bias voltage is applied across the dot, through the appearance of a Coulomb staircase. This is most pronounced in the case of strong asymmetry in the coupling to the leads where one lead causes a bottleneck in the transport. For instance, in the case where the bias voltage is applied to the left lead and $\Gamma_{\mathrm{L}} \gg \Gamma_{\mathrm{R}}$, then as the bias is increased by E_{c}, more electrons are added to the dot and they can accumulate on it, leading to a staircase structure in the current-voltage (I-V) characteristics. On the other hand, this staircase structure is less noticable when the couplings to each lead are approximately equal ($\Gamma_{\mathrm{L}} \approx \Gamma_{\mathrm{R}}$) as electrons tunnel on and off at roughly the same rate. The one-on-one-off type of tunnelling limits the accumulation of electrons on the dot and the staircase becomes less observable.

The Coulomb staircase is often treated in the case of instantaneous (and therefore complete) thermalisation, with the use of the classical master equation being the most prevalent approach. The master equation uses a rate equation for the probability, p_N, of having N electrons on the dot. Due to the presence of the large charging energy, the dot experiences single electron tunnelling meaning that the rate equation is given by [9, 117, 121, 131]

$$\frac{\mathrm{d}p_N}{\mathrm{d}t} = \Gamma^{\mathrm{F}}_{N-1} p_{N-1} + \Gamma^{\mathrm{T}}_{N+1} p_{N+1} - \left(\Gamma^{\mathrm{F}}_N + \Gamma^{\mathrm{T}}_N\right) p_N, \tag{5.8}$$

where $\Gamma^{\mathrm{F(T)}}_N$ is the tunnelling rate from (to) the leads given that there are N electrons on the dot before the tunnelling event has occurred. These have contributions from both the left and right lead, for example $\Gamma^{\mathrm{F}}_N = \Gamma^{\mathrm{FL}}_N + \Gamma^{\mathrm{FR}}_N$, and have the form

$$\Gamma^{\alpha}_N = \frac{G_\alpha}{e^2} \int \mathrm{d}E f(E)(1 - f(E - \Delta E_\alpha)) = \frac{G_\alpha}{e^2} \frac{\Delta E_\alpha}{\mathrm{e}^{\beta \Delta E_\alpha} - 1}, \tag{5.9}$$

where $\alpha = \mathrm{FL}, \mathrm{FR}, \mathrm{TL}, \mathrm{TR}$, ΔE_α is the change in energy due to the tunnelling event α

and $G_{\mathrm{FL}} = G_{\mathrm{TL}}$ etc. as there is only one value of conductance per lead. The form of the tunnelling rates in Eq. (5.9) are indicative of the full thermalisation occurring in the dot because, in addition to the integration over all energies, the distribution function in both the dot and leads is the standard Fermi function.

After defining the set of equations for the probabilities, Eq. (5.8), the steady-state current can be found, first by finding the steady-state probabilities through utilising $\frac{\mathrm{d}p_N}{\mathrm{d}t} = 0$ and the normalisation $\sum_N p_N = 1$ and then by making use of current conservation. This is simply the statement that the total current (as opposed to the current at each individual energy) going from the dot to right lead is equal to that coming to the dot from the left lead and allows the current to be expressed as [9, 117, 121, 131]

$$I = \frac{e}{2} \sum_N p_N \left(\Gamma_N^{\mathrm{FL}} + \Gamma_N^{\mathrm{TR}} - \Gamma_N^{\mathrm{TL}} - \Gamma_N^{\mathrm{FR}} \right). \tag{5.10}$$

Using this formula, the properties mentioned above regarding the Coulomb staircase can be obtained, as well as the peaks in the conductance as a function of gate voltage. In general, this method is useful for calculating many transport properties in the classical Coulomb blockade regime, providing that the tunnelling electrons undergo instantaneous thermalisation with the rest of the electrons on the dot. The Fermi energy of the dot must also be much larger than the charging energy so that the lowest energy levels of the dot do not influence transport.

Despite the simplicity of the formalism describing the classical Coulomb blockade regime, if the absence of thermalisation is to be considered in the non-equilibrium situation, an alternative method is required. In the limit where there are a large number of electrons on the dot, previous studies involving the absence of thermalisation have been limited to the linear response regime [118] as well as numerical studies [132]. To build on this, the work presented in *Coulomb staircase in an asymmetrically coupled quantum dot* [25] at the end of this chapter explores the Coulomb staircase analytically and numerically in the case of asymmetrical coupling to the leads and a complete absence of

thermalisation. In addition, the effect of the bottom of the dot is also studied - leading to an additional transport regime where the staircase is practically unobtainable experimentally. In order to address this problem the Keldysh formalism will be used and a discussion on the use of this in the Coulomb blockade regime will be discussed in the next section.

5.4 Tunnelling Density of States in Quantum Dots

Previously the Keldysh formalism has been used to study quantum dots to draw comparisons between the zero-bias anomaly and the Coulomb blockade [7] as both are characterised by gaps in the tunnelling density of states at small energies.

The tunnelling density of states in a Coulomb blockaded quantum dot was expanded upon in [133] where the authors used the Keldysh formalism to calculate the tunnelling density of states, $\nu(\varepsilon)$ in the linear response regime. Crucially, the authors used the fact that for any given gate voltage only two states with a different number of particles (N and $N+1$) contribute to the tunnelling density of states giving

$$\frac{\nu(\varepsilon)}{\nu_0} = \frac{U(\varepsilon - \Omega_N) + \mathrm{e}^{-\beta\Omega_N} U(\varepsilon - \Omega_{N+1})}{1 + \mathrm{e}^{-\beta\Omega_N}}. \tag{5.11}$$

Here ν_0 is the density of states at large energies (greater than E_c) and $U(\varepsilon - \Omega_N) = f_0(\varepsilon - \Omega_{N-1}) + 1 - f_0(\varepsilon - \Omega_N)$, with $f_0(\varepsilon)$ being a Fermi function containing the chemical potential of the dot, ε_F. This result not only provides the correct gap in the tunnelling density of states in the valley of conductance but it also identifies a half-gap at the peak, which is necessary in order to produce the correct peak shape given by Eq. (5.4). It can also be used to identify the electronic noise in the linear response regime [134,135]. Though these results are specific to equilibrium and linear response, the use of Keldysh and more specifically the form of current used can be used in the absence of thermalisation (though this makes no difference in equilibrium). The current expression used can be derived using

the expression of the current for a single lead, α,

$$I_\alpha = -ie\langle[H, N_\alpha]\rangle, \tag{5.12}$$

with $N_\alpha = \sum_k c^\dagger_{\alpha,k} c_{\alpha,k}$ being the number operator for electrons in the leads and H is the Hamiltonian for the dot and lead system. Through various manipulations using the Keldysh contour and expansion of the S-matrix, the current can be written as [25,85,136]

$$I_\alpha = e\Gamma_\alpha \sum_N p_N \sum_n \Big(F_N(\varepsilon_n)\left[1 - f(\varepsilon_n - \mu_\alpha + \Omega_{N-1})\right] - \left[1 - F_N(\varepsilon_n)\right] f(\varepsilon_n - \mu_\alpha + \Omega_N) \Big), \tag{5.13}$$

with the details in Appendix D. Then in order to understand the non-equilibrium current, it is necessary to be able to calculate (in the absence of thermalisation) the probability that the dot contains N electrons, p_N, as well as the distribution function of the electrons given that there are N of them on the dot, $F_N(\varepsilon_n)$. This is the subject of the next section in which the manuscript *Coulomb staircase in an asymmetrically coupled quantum dot* [25] is presented.

5.5 *Coulomb staircase in an asymmetrically coupled quantum dot*

The manuscript for the publication *Coulomb staircase in an asymmetrically coupled quantum dot* authored by myself, Rose Davies, Igor V. Lerner and Igor V. Yurkevich features below. As first author, I performed the analytical calculations and analysed the results. The numerical calculations using the QmeQ package were performed by Rose Davies. I additionally wrote the majority of the manuscript with collaboration on the writing being provided by the other co-authors. Assistance on the direction of the project was provided by Igor V. Lerner and Igor V. Yurkevich. A version of this manuscript can be found in *Journal of Physics: Condensed Matter* [25].

Coulomb staircase in an asymmetrically coupled quantum dot

G McArdle[1], R Davies[2], I V Lerner[1], I V Yurkevich[2]

[1] School of Physics and Astronomy, University of Birmingham, Birmingham, B15 2TT

[2] School of Informatics and Digital Engineering, Aston University, Birmingham, B4 7ET

E-mail: i.v.lerner@bham.ac.uk

Abstract. We investigate the Coulomb blockade in quantum dots asymmetrically coupled to the leads for an arbitrary voltage bias focusing on the regime where electrons do not thermalise during their dwell time in the dot. By solving the quantum kinetic equation, we show that the current-voltage characteristics are crucially dependent on the ratio of the Fermi energy to charging energy on the dot. In the standard regime when the Fermi energy is large, there is a Coulomb staircase which is practically the same as in the thermalised regime. In the opposite case of the large charging energy, we identify a new regime in which only one step is left in the staircase, and we anticipate experimental confirmation of this finding.

Keywords: Coulomb blockade; quantum dots; non-equilibrium systems; many-body localisation; Keldysh techniques.

Submitted to: *J. Phys.: Condens. Matter*

1. Introduction

The phenomenon of the Coulomb blockade in quantum dots has been a longstanding topic of interest and many aspects of it have been studied (see [1, 2, 3] for reviews). It arises due to the strong Coulomb interaction resulting in large charging energy, $E_{\rm c} = e^2/C$, that must be overcome in order to add an additional electron onto the dot of capacitance C. This leads to a number of notable physical results such as peaks in the conductance as a function of gate voltage [4, 5, 6] and a staircase in the dependence of current on the bias voltage (I-V characteristics) that has become known as the Coulomb staircase [4, 7, 8].

A prominent approach to understanding transport in mesoscopic systems is based on the classical master equation [5, 7, 9], which has typically assumed full thermalisation on the dot. However, a master equation approach is not limited to only dealing with the thermalised case, and the quantum master equation provides a full microscopic description by including the traced-out leads, with the assumption of thermalisation being made to simplify calculations. Using this approach, the full counting statistics of the problem can be calculated under a Markovian approximation [10, 11, 12, 13], with recent progress in calculating noise for non-Markovian tunnelling to second order [14]. Other approaches have been successful, such as using the Ambegaokar-Eckern-Schön (AES) action [15] to study relaxation dynamics on a quantum dot [16] - although this method cannot be utilised in all regimes [17]. The non-equilibrium Green's function approach has also been used to highlight the relation between the Coulomb blockade and the zero-bias anomaly [18, 19, 20, 21], as well as to calculate the tunnelling density of states of a Coulomb-blockaded quantum dot near equilibrium [18, 22].

The assumption of thermalisation is justified when the quasiparticle decay rate due to the electron-electron interaction, γ, is much larger than the tunnelling rates to the (left and right) leads, $\Gamma_{\rm L,R}$, so that the time spent by the extra electrons on the dot is sufficient for their full thermalisation.

In this paper we consider the regime where one can neglect thermalisation,

$$\gamma \ll \Gamma, \tag{1}$$

otherwise keeping the separation of energy scales characteristic for the classical Coulomb blockade [3]:

$$\hbar\Gamma \ll \Delta \ll k_B T \ll E_{\rm c}, \tag{2}$$

where Δ is the typical energy level spacing and T is the temperature. The rest of this paper will set the Boltzmann and reduced Plank constant to equal one, $\hbar, k_B = 1$. The regime (1) is important, in particular, when electrons in the dot experience localisation in the Fock space [23] (the precursor for many-body localisation [24]) and is easily reachable in metallic quantum dots with a large dimensionless conductance g. We additionally consider the regime where there are a large number of electrons on the dot ($N \gg 1$). Previously, analytical calculations for this regime have been performed in the linear response limit [6], while numerical calculations for an arbitrary bias voltage [25]

have been limited to the experimentally important regime [26] when $\varepsilon_{\rm F} \gg E_{\rm c}$ with $\varepsilon_{\rm F}$ being the Fermi energy on the dot. The opposite limit of considerable experimental and theoretical interest is that of a few electrons on the dot, where the lowest energy levels make a strong impact on the observables (see [27] for a review), and the fine structure of the Coulomb staircase is resolved [28].

Here we consider a quantum dot in the absence of thermalisation with strong asymmetry in the coupling to the leads (typically assumed in considerations of the thermalised regime [4, 7, 8, 9]) for both large and small ratio $\varepsilon_{\rm F}/E_{\rm c}$. We use the quantum kinetic equation to develop a full analytical solution for the Coulomb staircase for $N \gg 1$ at any voltage eV.

The solution crucially depends on the ratio $\varepsilon_{\rm F}/E_{\rm c}$. For $\varepsilon_{\rm F} \gg E_{\rm c}$, the absence of thermalisation does not play a significant role and the Coulomb staircase remains practically the same as in the thermalised regime [4, 7, 8, 9], with an equilibrium established with the most strongly coupled lead.

However, for $\varepsilon_{\rm F} \ll E_{\rm c}$ we show that the staircase practically vanishes. Instead, assuming the traditional anisotropy in coupling to the leads, $\Gamma_{\rm R} \ll \Gamma_{\rm L}$, with the voltage V applied to the left lead, there is a single step in the current equal to $e\Gamma_{\rm R}(N_0{+}1)$ (with N_0 being the number of electrons on the dot at $V{=}0$) when V increases from 0 to $eV \sim E_{\rm c}$. All the further steps are of order 1 in the same units of $e\Gamma_{\rm R}$, i.e. practically invisible for $N \gg 1$. This result is complimented with a numerical calculation using the quantum master equation approach, showing that features of this very strong charging energy regime persist even for $N \lesssim 10$. This is due to a significant contribution of the low energy levels even for a large number of electrons in the dot.

2. Model

We consider the quantum dot asymmetrically coupled to two leads with the bias voltage V applied to the left one described by the Hamiltonian

$$H = H_{\rm d} + H_\ell + H_{\rm T}\,. \tag{3}$$

Here $H_{\rm d}$ is the Hamiltonian of the Coulomb-blockaded dot in the zero-dimensional limit [1, 2, 3],

$$H_{\rm d} = \sum_n \varepsilon_n d_n^\dagger d_n + \tfrac{1}{2} E_{\rm c} \left(\hat{N} - N_{\rm g}\right)^2, \tag{4}$$

where ε_n are the energy levels of the dot, $d_n^\dagger$ (d_n) are the creation (annihilation) operators of the quantum dot, $\hat{N} = \sum_n d_n^\dagger d_n$ is the number operator for the dot, and $N_{\rm g}$ is the preferable number of electrons on the dot in equilibrium set by the gate voltage. The leads are described by

$$H_\ell = \sum_{k,\alpha} (\varepsilon_k - \mu_\alpha)\, c_{k,\alpha}^\dagger c_{k,\alpha}, \tag{5}$$

where $\alpha = {\rm L}, {\rm R}$ labels the lead, $c_{k,\alpha}^\dagger$ ($c_{k,\alpha}$) are the creation (annihilation) operators for an electron of energy ε_k, and μ_α is the chemical potential of the lead, $\mu_{\rm L} = \mu + eV$ and

$\mu_{\rm R} = \mu$. The tunnelling between the dot and the leads is described by the tunnelling Hamiltonian

$$H_{\rm T} = \sum_{\alpha,k,n} \left(t_\alpha c^\dagger_{k,\alpha} d_n + \text{h.c.} \right), \tag{6}$$

where the tunnelling amplitude t_α, which is assumed to be independent of k and n, defines the broadening of the energy levels $\Gamma = \Gamma_{\rm L} + \Gamma_{\rm R}$ with $\Gamma_\alpha = 2\pi\nu_\alpha |t_\alpha|^2$, with the density of states ν_α taken to be a constant.

We assume the absence of thermalisation in the dot which will allow us to use the quantum kinetic equation for a given energy. This is justified when the inequality (1) is satisfied. For a zero-dimensional diffusive dot, the quasiparticle decay rate due to the electron-electron interaction at energy ε is given for $\Delta \ll T$ by [23, 29, 30]

$$\gamma(\varepsilon) \approx \Delta \left(\frac{\varepsilon}{E_{\rm Th}} \right)^2, \tag{7}$$

where $E_{\rm Th} = g\Delta$ is the Thouless energy and $g \gg 1$ is the dimensionless conductance of the dot. This result is valid provided that $\sqrt{g}\Delta < \varepsilon < E_{\rm Th}$.

In the equilibrium regime in the absence of the coupling to the leads, the tunnelling density of states has some interesting features [22] which, intuitively, are preserved if one lead dominates the behaviour of the system and the chemical potential on the dot will be determined by that lead. This quasi-equilibration allows us to solve exactly the case of strongly asymmetrically coupled leads, either for $\Gamma_{\rm L}/\Gamma_{\rm R} \gg 1$ when the jumps in the current exist, or for $\Gamma_{\rm L}/\Gamma_{\rm R} \ll 1$ when the current has almost Ohmic behaviour.

3. Quantum kinetic equation

To analyse the Coulomb blockaded quantum dot in the non-linear regime we use the Keldysh technique (see, e.g., [31] for a review) in a way similar to that detailed in [32].

3.1. Quantum dot in the weak coupling limit

In the case of an isolated dot, i.e. totally neglecting the level broadening Γ, the Keldysh Green's function can be written as a sum over all levels, $g^{>,<}(\varepsilon) = \sum_n g_n^{>,<}(\varepsilon)$ with the single-level Green's functions given by

$$g_n^>(t) = -i \,\text{Tr}\left(\hat\rho_0 d_n(t) d_n^\dagger\right), \;\; g_n^<(t) = i \,\text{Tr}\left(\hat\rho_0 d_n^\dagger d_n(t)\right), \tag{8}$$

where $d_n(t) = \mathrm{e}^{iHt} d_n \mathrm{e}^{-iHt}$ and $\hat\rho_0$ is the density matrix. Additionally, the particle number is conserved and the Green's functions can be written as sums over the N-particle subspaces,

$$g_n^>(\varepsilon) = -2\pi i \sum_N \delta\left(\varepsilon - \varepsilon_n - \Omega_N\right) g_N^>(\varepsilon_n), \qquad g_N^>(\varepsilon_n) = \text{Tr}_N\left(\hat\rho_0 d_n d_n^\dagger\right), \tag{9}$$

$$g_n^<(\varepsilon) = -2\pi i \sum_N \delta\left(\varepsilon - \varepsilon_n - \Omega_{N-1}\right) g_N^<(\varepsilon_n), \quad g_N^<(\varepsilon_n) = -\,\text{Tr}_N\left(\hat\rho_0 d_n^\dagger d_n\right), \tag{10}$$

with the normalisation $\sum_N \left(g_N^>(\varepsilon_n) - g_N^<(\varepsilon_n)\right) = 1$. The charging energy required to add an electron is included above through Ω_N defined as

$$\Omega_N \equiv E_{N+1} - E_N = E_\mathrm{c}\Big(N + \tfrac{1}{2} - N_\mathrm{g}\Big), \qquad E_N \equiv \tfrac{1}{2}E_\mathrm{c}(N - N_\mathrm{g})^2. \tag{11}$$

The coupling to the leads is included via the quantum kinetic equation (QKE), which in the weak coupling limit ($\Gamma \to 0$) can be written for each level as [32, 33]

$$g_n^{>,<}(\varepsilon) = g_n^\mathrm{R}(\varepsilon)\,\Sigma^{>,<}(\varepsilon)\,g_n^\mathrm{A}(\varepsilon). \tag{12}$$

The self energies for non-interacting leads are assumed to be independent of the dot level n and are given by

$$\Sigma^>(\varepsilon) = \sum_{k,\alpha} |t_\alpha|^2 g_{k,\alpha}^>(\varepsilon) = -i\left[\Gamma - (\Gamma_\mathrm{L} f_\mathrm{L}(\varepsilon) + \Gamma_\mathrm{R} f_\mathrm{R}(\varepsilon))\right], \tag{13}$$

$$\Sigma^<(\varepsilon) = \sum_{k,\alpha} |t_\alpha|^2 g_{k,\alpha}^<(\varepsilon) = i\left(\Gamma_\mathrm{L} f_\mathrm{L}(\varepsilon) + \Gamma_\mathrm{R} f_\mathrm{R}(\varepsilon)\right). \tag{14}$$

Above, the Green's functions for the leads are $g_{k,\alpha}^>(\varepsilon) = -2\pi i(1 - f(\varepsilon - \mu_\alpha))\delta(\varepsilon - \varepsilon_k + \mu_\alpha)$ and $g_{k,\alpha}^<(\varepsilon) = 2\pi i f(\varepsilon - \mu_\alpha)\delta(\varepsilon - \varepsilon_k + \mu_\alpha)$, where $f(\varepsilon - \mu_\alpha)$ is a Fermi function. The density of states in the leads, which enters via the tunnelling rates $\Gamma_\alpha = 2\pi\nu_\alpha|t_\alpha|^2$, is given by $\nu_\alpha = \sum_k \delta(\varepsilon - \varepsilon_k + \mu_\alpha)$, while $\Gamma = \Gamma_\mathrm{L} + \Gamma_\mathrm{R}$. Note that the form of (12), with all functions being considered at the same energy, corresponds to no thermalisation with $\gamma \to 0$. This rate must be the smallest scale in the system for the hierarchy of scales in (1, 2) to be satisfied, therefore it can be taken to zero with no issues.

Now we rewrite the QKE (12) as

$$g_n^>(\varepsilon)\Sigma^<(\varepsilon) = g_n^<(\varepsilon)\Sigma^>(\varepsilon). \tag{15}$$

Substituting in Eqs. (9, 10) we use the ansatz

$$g_N^>(\varepsilon_n) = p_N\left(1 - F_N(\varepsilon_n)\right) \quad \text{and} \quad g_N^<(\varepsilon_n) = -p_N F_N(\varepsilon_n), \tag{16}$$

where p_N is the probability of having N electrons on the dot and $F_N(\varepsilon_n)$ is the distribution function given N electrons on the dot which, in the case of complete thermalisation, goes over to the equilibrium Fermi distribution function. In these terms, we write the QKE as follows:

$$p_N\left(1 - F_N(\varepsilon_n)\right)\widetilde{f}(\varepsilon_n + \Omega_N) = p_{N+1}F_{N+1}(\varepsilon_n)\left(1 - \widetilde{f}(\varepsilon_n + \Omega_N)\right), \tag{17}$$

where

$$\widetilde{f}(\varepsilon) = \frac{\Gamma_\mathrm{L}}{\Gamma} f(\varepsilon - \mu - eV) + \frac{\Gamma_\mathrm{R}}{\Gamma} f(\varepsilon - \mu). \tag{18}$$

This corresponds to the detailed balance equations derived in [6] for $\Delta \gg T$ and reproduces the case of complete thermalisation after the summation over n and making the replacement $F_N(\varepsilon) \to f(\varepsilon - \varepsilon_\mathrm{F})$. The QKE (17) should be complemented by the normalisation conditions, $\sum_N p_N = 1$ and $\sum_n F_N(\varepsilon_n) = N$.

We represent the current going from the dot to the lead α via p_N and $F_N(\varepsilon_n)$ as

$$I_\alpha = e\Gamma_\alpha \sum_N p_N \sum_n \Big(F_N(\varepsilon_n)\left[1 - f(\varepsilon_n - \mu_\alpha + \Omega_{N-1})\right] - \left[1 - F_N(\varepsilon_n)\right] f(\varepsilon_n - \mu_\alpha + \Omega_N)\Big) \tag{19}$$

Applying current conservation, $I = I_{\rm R} = -I_{\rm L}$ and using $\mu_{\rm L} = \mu + eV$ and $\mu_{\rm R} = \mu$, we express the current as

$$I = e\frac{\Gamma_{\rm L}\Gamma_{\rm R}}{\Gamma}\sum_N p_N \sum_n \Big(F_N(\varepsilon_n)\left[f(\varepsilon_n - \mu_{N-1} - eV) - f(\varepsilon_n - \mu_{N-1})\right] + (1 - F_N(\varepsilon_n))\left[f(\varepsilon_n - \mu_N - eV) - f(\varepsilon_n - \mu_N)\right]\Big). \tag{20}$$

with $\mu_N \equiv \mu - \Omega_N$. Assuming a density of states on the dot to be constant, $1/\Delta$, we convert the sum over n to an integral over all energies on the dot (counted from zero). Then in the low-T limit

$$I = e\frac{\Gamma_{\rm L}\Gamma_{\rm R}}{\Gamma}\sum_N p_N \left[\int_{\mu_{N-1}}^{\mu_{N-1}+eV} {\rm d}\varepsilon\, \Theta(\varepsilon) F_N(\varepsilon) + \int_{\mu_N}^{\mu_N+eV} {\rm d}\varepsilon\, \Theta(\varepsilon)(1 - F_N(\varepsilon))\right], \tag{21}$$

where $\Theta(\varepsilon)$ is the Heaviside step function.

3.2. Solution to the QKE

The charging energy strongly penalises states with a wrong number of electrons on the dot. In the case of strongly asymmetric leads with $\Gamma_{\rm L} \gg \Gamma_{\rm R}$, the main contribution to (20) is given by the two states with N closest to $N_{\rm g} + eV/E_{\rm c}$, since electrons have time to fill the dot up. In the opposite case, $\Gamma_{\rm L} \ll \Gamma_{\rm R}$, the two relevant states are those closest to $N_{\rm g}$. Keeping only the appropriate two states in the QKE (17) allows us to obtain the following exact solution:

$$\begin{aligned} p_N &= \frac{Z_N}{Z_N + Z_{N+1}}, & p_{N+1} &= \frac{Z_{N+1}}{Z_N + Z_{N+1}}, \\ F_N(\varepsilon_n) &= \frac{Z_N(\varepsilon_n)}{Z_N}, & F_{N+1}(\varepsilon_n) &= \frac{Z_{N+1}(\varepsilon_n)}{Z_{N+1}}, \end{aligned} \tag{22}$$

where

$$\begin{aligned} Z_N &= \sum_{\{n_j=0,1\}} \prod_{j=1}^{\infty} \left[\varphi(\varepsilon_j + \Omega_N)\right]^{n_j} \delta_{(\sum_j n_j),N}, \\ Z_{N+1} &= \sum_{\{n_j=0,1\}} \prod_{j=1}^{\infty} \left[\varphi(\varepsilon_j + \Omega_N)\right]^{n_j} \delta_{(\sum_j n_j),N+1}, \end{aligned} \tag{23}$$

with functions φ defined via $\widetilde{f}$ in (18) as

$$\varphi(\varepsilon_j + \Omega_N) = \frac{\widetilde{f}(\varepsilon_j + \Omega_N)}{1 - \widetilde{f}(\varepsilon_j + \Omega_N)}, \tag{24}$$

while $Z_N(\varepsilon_n)$ in (22) is defined by restricting the sums in (23) to configurations with the state ε_n occupied. It is important to highlight that due to the form of the QKE (17), Z_{N+1} in (23) contain Ω_N rather than Ω_{N+1} so that the relevant N dependence enters only in the Krönecker delta.

When $N \gg 1$, the Krönecker delta is equivalent to a delta function,

$$\delta_{(\sum_j n_j),N} = \int \frac{{\rm d}\theta}{2\pi} {\rm e}^{i\theta(\sum_j n_j - N)}\,, \tag{25}$$

which allows us to write the sums in (23) in the form

$$Z_N = \int \frac{\mathrm{d}\theta}{2\pi} \mathrm{e}^{Nf(\theta)}, \qquad f(\theta) = \frac{1}{N}\sum_j \ln\left(1+\varphi(\varepsilon_j+\Omega_N)\mathrm{e}^{i\theta}\right) - i\theta. \tag{26}$$

Now Z_N can be evaluated in the saddle-point approximation. The optimal θ_0 is found from the second equation above where the sum is converted to the integral, $\sum_j \to \Delta^{-1}\int_0^\infty \mathrm{d}\varepsilon$, which gives

$$\varepsilon_\mathrm{F} = N\Delta = \int_0^\infty \mathrm{d}\varepsilon \left(\frac{\mathrm{e}^{-i\theta_0}}{\varphi(\varepsilon+\Omega_N)}+1\right)^{-1}. \tag{27}$$

As Ω_N is unchanged by definition when going between Z_N and Z_{N+1}, (23), the relevant N dependence of θ_0 enters only via $\varepsilon_\mathrm{F} = N\Delta$. Thus we find that in the saddle-point approximation $Z_N = g(\theta_0)\mathrm{e}^{-iN\theta_0}$, where $g(\theta_0)$ is a function which depends on N only via ε_F. Hence for $N \gg 1$, this function is approximately the same for Z_N and Z_{N+1} which allows us to cancel $g(\theta_0)$ in calculating p_N and $F_N(\varepsilon_n)$ in (22). This results in

$$\frac{p_{N+1}}{p_N} = \mathrm{e}^{-i\theta_0}, \quad F_N(\varepsilon_n) \approx F_{N+1}(\varepsilon_n) \approx \left(\frac{\mathrm{e}^{-i\theta_0}}{\varphi(\varepsilon+\Omega_N)}+1\right)^{-1}. \tag{28}$$

The ratio of probabilities can be found by using $N = \sum_n F_N(\varepsilon_n)$, which corresponds to the saddle point equation above.

The resulting I-V characteristics turn out to be strikingly different for the two opposite regimes, when the ratio $\varepsilon_\mathrm{F}/E_\mathrm{c}$ is either small or large, as described in the following section.

4. Results and Discussion

We begin by reproducing the well-known results of the standard theory for $\varepsilon_\mathrm{F} \gg E_\mathrm{c}$ to show that (i) our approach works and (ii) the absence of the full thermalisation does not make a significant impact on the Coulomb staircase in the case of strong asymmetry in the coupling to the leads.

Then we show that in the opposite limit, $\varepsilon_\mathrm{F} \ll E_\mathrm{c}$, there is only one significant step left in the Coulomb staircase if $N \gg 1$. Additionally, we present numerical results for small N which are in full agreement with our analytical results for $N \gg 1$.

4.1. Small charging energy, $E_\mathrm{c} \ll \varepsilon_\mathrm{F}$

We start with the linear response regime. Then $\widetilde{f}(\varepsilon) \to f(\varepsilon-\mu)$ in (18) so that $\varphi(\varepsilon+\Omega_N) \to \exp[-\beta(\varepsilon-\mu+\Omega_N)]$ in (24). Hence, using (28) we reduce the saddle point equation (27) to

$$\varepsilon_\mathrm{F} = \int_0^\infty \frac{\mathrm{d}\varepsilon}{\mathrm{e}^{\beta(\varepsilon-\mu_N)-i\theta_0}+1} = T\ln\left(\mathrm{e}^{\beta\mu_N+i\theta_0}+1\right) \approx \mu_N + i\theta_0 T, \tag{29}$$

where the approximate equality holds in the low-temperature limit, $\beta\mu_N + i\theta_0 \gg 1$. The result in (29) leads to $i\theta_0 = \beta(\varepsilon_\mathrm{F}-\mu_N) = \beta(\varepsilon_\mathrm{F}-\mu+\Omega_N)$ (with μ being the

chemical potential in the leads and $\varepsilon_{\rm F}$ in the dot), meaning that the low-temperature limit corresponds to $\beta\varepsilon_{\rm F} \gg 1$ satisfying the conditions in (2). Furthermore, substituting into (28) the expression for $i\theta_0$, and using $p_N + p_{N+1} \approx 1$ results in the following expressions for the probabilities and distribution function,

$$p_N = \frac{\mathrm{e}^{-\beta(E_N+N(\varepsilon_{\rm F}-\mu))}}{\sum_N \mathrm{e}^{-\beta(E_N+N(\varepsilon_{\rm F}-\mu))}}, \quad F_N(\varepsilon) = \frac{1}{\mathrm{e}^{\beta(\varepsilon-\varepsilon_{\rm F})}+1}, \tag{30}$$

where the sum over N is restricted to the two states with N closest to $N_{\rm g}$. Substituting (30) into the current (20) results in the following shape of the differential conductance near the peak, $\mu - \Omega_N - \varepsilon_{\rm F} = 0$:

$$G = \frac{\mathrm{d}I}{\mathrm{d}V} = \frac{e^2}{2\Delta}\frac{\Gamma_{\rm L}\Gamma_{\rm R}}{\Gamma}\frac{\frac{\beta}{2}(\Omega_N+\varepsilon_{\rm F}-\mu)}{\sinh(\frac{\beta}{2}(\Omega_N+\varepsilon_{\rm F}-\mu))}, \tag{31}$$

in agreement with [4, 6].

We now turn to the nonlinear regime and demonstrate, by reproducing the well-known results [4, 7, 8] for strongly asymmetric coupling to the leads and $\varepsilon_{\rm F} \gg E_{\rm c}$, that the absence of thermalisation has no impact on the Coulomb staircase. For $\Gamma_{\rm L} \gg \Gamma_{\rm R}$, the solution to the QKE (17) for any V is given by (30) provided that we replace μ by $\mu_{\rm L} \equiv \mu + eV$ and restrict the sum over N to the two states with N closest to $N_{\rm g} + eV/E_{\rm c}$. Due to the exponential forms of the probabilities in (30), only one such state contributes to the current outside some narrow windows in V. For a given V, this is the state where N obeys the inequality $\Omega_{N-1} \lesssim eV \lesssim \Omega_N$. Noticing that the distribution function in (30), $F_N(\varepsilon) = f(\varepsilon - \varepsilon_{\rm F})$, is a Fermi function with a chemical potential $\varepsilon_{\rm F}$, we see that the second integral in (21) does not contribute to the current for low T, as the upper limit of integration $\mu_N + eV \approx \varepsilon_{\rm F} - (\Omega_N - eV) < \varepsilon_{\rm F}$.

Consider the contribution of the first integral in (21), starting with the regime that begins in equilibrium ($V = 0$) and continues for $0 \leq eV \lesssim \Omega_{N_0}$, when there

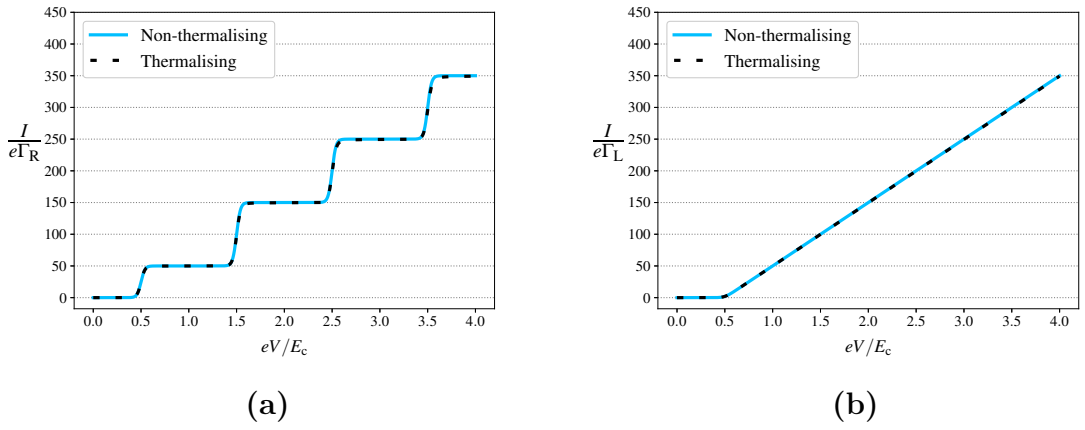

Figure 1. The I-V characteristics for a dot in the regime where $N_0\Delta \gg E_{\rm c}$ ($N_0\Delta$=10$E_{\rm c}$) and $\Omega_{N_0} = E_{\rm c}/2$. The blue line represents our solution to the QKE and the black dashed line is the solution to the master equation in the standard theory where full thermalisation is assumed [4, 7, 8]. In both instances, **(a)**: $\Gamma_{\rm L}/\Gamma_{\rm R} = 10^3$ and **(b)**: $\Gamma_{\rm L}/\Gamma_{\rm R} = 10^{-3}$ an equilibrium is set up with the dominant lead and the approaches produce the same results.

are N_0 electrons on the dot. Then, as $\Omega_{N_0} \approx E_c/2$ the lower integration limit $\mu_{N_0-1} \equiv \mu - \Omega_{N_0-1} \approx \varepsilon_F + E_c/2 > \varepsilon_F$ so that this integral also vanishes. The current is therefore zero as expected. With V increasing beyond Ω_{N_0}, there are $N > N_0$ electrons on the dot. In this case, having $\varepsilon_F \gg E_c$ ensures that $\varepsilon_F > \Omega_N$ for all relevant Ω_N and both the integration limits are positive, so the presence of $\Theta(\varepsilon)$ is irrelevant. The steps in the current in the low-T limit are, therefore, given by

$$\begin{aligned} I &= 0, & 0 \le eV \lesssim \Omega_{N_0} \qquad & (p_{N_0} = 1), \\ I &= e\Gamma_R \frac{\Omega_{N_0}}{\Delta}, & \Omega_{N_0} \lesssim eV \lesssim \Omega_{N_0+1} \qquad & (p_{N_0+1} = 1), \\ I &= e\Gamma_R \frac{\Omega_{N_0+1}}{\Delta}, & \Omega_{N_0+1} \lesssim eV \lesssim \Omega_{N_0+2} \qquad & (p_{N_0+2} = 1), \end{aligned} \tag{32}$$

and so on. This demonstrates a staircase structure with the steps separated by $eV{=}E_c$ and an almost constant height proportional to E_c/Δ. The full results, including the windows around the jumps at $eV{=}\Omega_N$, are obtained by substituting (30) with the change $\mu \to \mu_L$ into (20) and are practically indistinguishable from the full thermalisation case [4, 7, 8], as shown in Figure 1(a).

For the opposite asymmetry, $\Gamma_R \gg \Gamma_L$, equilibrium with the right lead (with no voltage applied there) is maintained and no staircase is observed as $p_{N_0} \approx 1$ for all values of V. Instead, the Ohmic behaviour prevails for $eV \gtrsim \Omega_{N_0}$ as the tunnelling electron gains more energy as shown in Figure 1(b).

4.2. Large charging energy, $E_c \gg \varepsilon_F$

In this limit, the low-energy states in the dot make a considerable impact on the transport behaviour. The reason is that the regime $\varepsilon_F < \Omega_N$, which was impossible $\varepsilon_F/E_c \gg 1$, now arises.

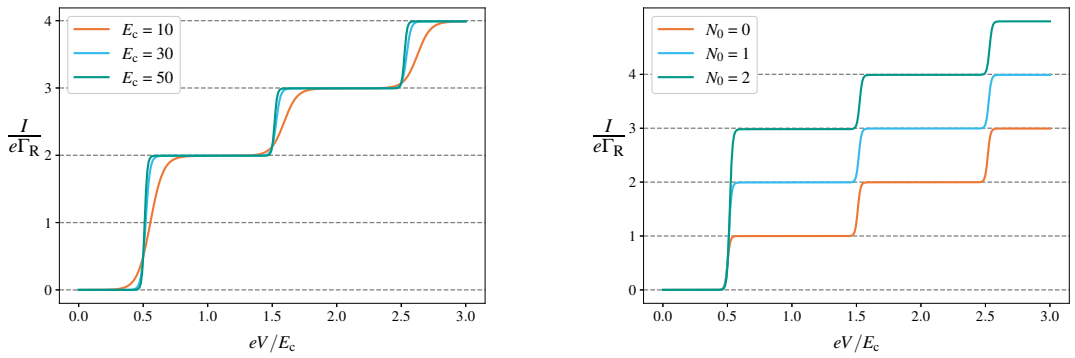

(a) **(b)**

Figure 2. The numerical I-V characteristics for a dot with 7 states in the regime where $N_0\Delta \ll E_c$ ($N_0\Delta \approx 0.01E_c$) and $\Omega_{N_0} = E_c/2$. **(a)**: Increasing the charging energy makes the steps sharper but does not affect the size of the jumps. **(b)**: Increasing the number, N_0, of electrons in equilibrium (with the gate voltage) illustrates that the first jump is equal to $e\Gamma_R(N_0{+}1)$. In both cases $\Gamma_L = 100\Gamma_R$.

For $\Gamma_{\rm L} \gg \Gamma_{\rm R}$, the expressions for p_N and $F_N(\varepsilon)$ are formally the same as for $E_{\rm c} \ll \varepsilon_{\rm F}$ in (30) with the substitution $\mu \to \mu_{\rm L}$. However, as $F_N(\varepsilon)$ is now an extremely narrow function (on the scale of $E_{\rm c}$) and the integration limits may be negative, the contributions of the above integrals to the current are severely restricted in comparison to the case of $\varepsilon_{\rm F}/E_{\rm c} \gg 1$. Starting again with N_0 electrons on the dot at equilibrium, we make similar arguments as in the former case to see that only the first integral in (21) contributes. The crucial difference for $N > N_0$ is that the lower limit of integration, $\mu_{N-1} \approx \varepsilon_{\rm F} - \Omega_{N-1} = N\Delta - \Omega_{N-1}$, is less than zero, so that $\Theta(\varepsilon)$ becomes relevant. Therefore, we find the current in the low-T limit to be strikingly different from that in (32). (Note that for the opposite asymmetry, $\Gamma_{\rm R} \gg \Gamma_{\rm L}$, the current remains Ohmic for any ratio $\varepsilon_{\rm F}/E_{\rm c}$.)

$$\begin{aligned} &I = 0, && 0 \le eV \lesssim \Omega_{N_0} && (p_{N_0} = 1), \\ &I = e\Gamma_{\rm R}(N_0+1), && \Omega_{N_0} \lesssim eV \lesssim \Omega_{N_0+1} && (p_{N_0+1} = 1), \\ &I = e\Gamma_{\rm R}(N_0+2), && \Omega_{N_0+1} \lesssim eV \lesssim \Omega_{N_0+2} && (p_{N_0+2} = 1), \end{aligned} \tag{33}$$

and so on. Crucially the first jump in the current (measured in units of $e\Gamma_{\rm R}$) at $eV = \Omega_{N_0}$ is equal to $N_0 + 1$ while all the subsequent jumps equal to 1 in these units.

For $N_0 \gg 1$, this means that the staircase practically disappears beyond the first step in contrast to the constant jumps of size $E_{\rm c}/\Delta$ for large $N_0\Delta$, see (32). Although we have performed analytical calculations for $N_0 \gg 1$, the results for $\varepsilon_{\rm F} \ll E_{\rm c}$ turn out to be exactly the same for small N_0 given a constant charging energy. We demonstrate this by numerically solving the quantum master equation [34] under the conditions (1, 2), for a dot with 7 levels. This was achieved by solving the first order von Neumann equation for a dot that has N energy levels separated by Δ; the first order equation is sufficient due to the small coupling to the leads. The many-body states on the diagonal of the density matrix are all the 2^N occupations with the appropriate charging energy, $E_c(N - N_g)^2/2$, added for the occupation of the configuration. There is no dissipation mechanism for a state to decay on the dot, with relaxation occurring after tunnelling into the leads, therefore the numerical calculations are for the case of zero thermalisation on the dot. The results are shown in Figure 2. While all the steps there are pronounced, all but the first one would practically disappear for $N_0 \gg 1$.

5. Conclusion

To summarise, we have analytically calculated I-V characteristics of the quantum dot with a strong asymmetry in the tunnelling coupling to the leads in the Coulomb blockade regime (2) in the absence of thermalisation (1). We have solved the appropriate quantum kinetic equation in the two limits, for either a large or small ratio, $E_{\rm c}/\varepsilon_{\rm F}$, of the charging energy to the Fermi energy of electrons in the dot.

We have demonstrated that for a relatively small charging energy, $E_{\rm c}/\varepsilon_{\rm F} \ll 1$, the absence of thermalisation in a quantum dot has practically no impact on the Coulomb staircase as an equilibrium is established between the dot and the most strongly coupled

lead, see Figure 1. This is in agreement with previous numerical results [25] which assume the distribution function is the same for all relevant N. We have verified this assumption in the large N limit when no more than two states are relevant in (28).

In the opposite limit, $E_c/\varepsilon_F \gg 1$, we have analytically shown that for $N \gg 1$ the Coulomb staircase has only one pronounced step. With a voltage V applied to the left lead and $\Gamma_L/\Gamma_R \gg 1$, this is a step in the current from 0 to $e\Gamma_R(N_0+1)$ in a narrow window around $eV = \Omega_{N_0}$ with $\Omega_{N_0} = E_c/2$ if $N_0 = N_g$, see (11). All the subsequent current jumps with V increasing have the magnitude $e\Gamma_R$, see (33), i.e. negligible when the number of electrons at equilibrium $N_0 \gg 1$. Further to the analytic results, we have numerically solved the quantum master equation for a constant E_c to find that the analytical results (33) proven for $N \gg 1$ are exactly valid also in the experimentally attractive regime of $N \lesssim 10$, see Figure 2. The reason for such behaviour of the Coulomb staircase is that the only electrons available for tunnelling are those in an energy window $\sim \varepsilon_F$ with the voltage window being much larger, $eV \sim E_c$. With ε_F/E_c increasing, more electrons are available for tunnelling, thus restoring the jumps between the steps to their full value $\propto E_c/\Delta$ in the usual regime $\varepsilon_F \gg E_c$ [4, 7, 8] where electrons from the entire voltage window contribute to the current.

Acknowledgements

We gratefully acknowledge support from EPSRC under the grant EP/R029075/1 (IVL) and from the Leverhulme Trust under the grant RPG-2019-317 (IVY).

References

[1] I. L. Aleiner, P. W. Brouwer, and L. I. Glazman, Quantum effects in Coulomb blockade, *Phys. Rep.* **358**, 309 (2002).

[2] Y. Alhassid, The statistical theory of quantum dots, *Rev. Mod. Phys.* **72**, 895 (2000).

[3] L. P. Kouwenhoven *et al.*, in *Mesoscopic Electron Transport*, edited by L. L. Sohn, L. P. Kouwenhoven, and G. Schön (Springer Netherlands, Dordrecht, 1997), pp. 105–214.

[4] I. O. Kulik and R. I. Shekhter, Kinetic phenomena and charge discreteness effects in granulated media, *Zh. Eksp. Teor. Fiz.* **68**, 623 (1975).

[5] D. V. Averin and K. K. Likharev, Coulomb blockade of single-electron tunneling and coherent oscillations in small tunnel junctions, *Journal of Low Temperature Physics* **62**, 345 (1986).

[6] C. W. J. Beenakker, Theory of Coulomb-blockade oscillations in the conductance of a quantum dot, *Phys. Rev. B* **44**, 1646 (1991).

[7] D. Averin and K. Likharev, in *Mesoscopic Phenomena in Solids*, Vol. 30 of *Modern Problems in Condensed Matter Sciences*, edited by B. Altshuler, P. Lee, and R. Webb (Elsevier, Amsterdam, 1991), pp. 173–271.

[8] M. Amman *et al.*, Analytic solution for the current-voltage characteristic of two mesoscopic tunnel junctions coupled in series, *Phys. Rev. B* **43**, 1146 (1991).

[9] S. Hershfield *et al.*, Zero-frequency current noise for the double-tunnel-junction Coulomb blockade, *Phys. Rev. B* **47**, 1967 (1993).

[10] D. A. Bagrets and Y. V. Nazarov, Full counting statistics of charge transfer in Coulomb blockade systems, *Phys. Rev. B* **67**, 085316 (2003).

[11] D. Marcos, C. Emary, T. Brandes, and R. Aguado, Finite-frequency counting statistics of electron transport: Markovian theory, *New J. Phys.* **12**, 123009 (2010).
[12] X.-Q. Li, P. Cui, and Y. Yan, Spontaneous Relaxation of a Charge Qubit under Electrical Measurement, *Phys. Rev. Lett.* **94**, 066803 (2005).
[13] C. Flindt *et al.*, Counting Statistics of Non-Markovian Quantum Stochastic Processes, *Phys. Rev. Lett.* **100**, 150601 (2008).
[14] Y. Xu, J. Jin, S. Wang, and Y. Yan, Memory-effect-preserving quantum master equation approach to noise spectrum of transport current, *Phys. Rev. E* **106**, 064130 (2022).
[15] V. Ambegaokar, U. Eckern, and G. Schön, Quantum dynamics of tunneling between superconductors, *Phys. Rev. Lett.* **48**, 1745 (1982).
[16] Y. I. Rodionov, I. S. Burmistrov, and N. M. Chtchelkatchev, Relaxation dynamics of the electron distribution in the Coulomb-blockade problem, *Phys. Rev. B* **82**, 155317 (2010).
[17] I. S. Beloborodov, K. B. Efetov, A. Altland, and F. W. J. Hekking, Quantum interference and Coulomb interaction in arrays of tunnel junctions, *Phys. Rev. B* **63**, 115109 (2001).
[18] A. Kamenev and Y. Gefen, Zero-bias anomaly in finite-size systems, *Phys. Rev. B* **54**, 5428 (1996).
[19] B. L. Altshuler and A. G. Aronov, Zero bias anomaly in tunnel resistance and electron-electron interaction, *Solid State Commun.* **30**, 115 (1979).
[20] B. L. Altshuler, A. G. Aronov, and P. A. Lee, Interaction effects in disordered fermi systems in two dimensions, *Phys. Rev. Lett.* **44**, 1288 (1980).
[21] B. L. Altshuler and A. G. Aronov, in *Electron–Electron Interactions in Disordered Systems*, Vol. 10 of *Modern Problems in Condensed Matter Sciences*, edited by A. L. Efros and M. Pollak (Elsevier, Amsterdam, 1985), pp. 1–153.
[22] N. Sedlmayr, I. V. Yurkevich, and I. V. Lerner, Tunnelling density of states at Coulomb-blockade peaks, *Europhys. Lett.* **76**, 109 (2006).
[23] B. L. Altshuler, Y. Gefen, A. Kamenev, and L. S. Levitov, Quasiparticle lifetime in a finite system: a nonperturbative approach, *Phys. Rev. Lett.* **78**, 2803 (1997).
[24] D. M. Basko, I. L. Aleiner, and B. L. Altshuler, Metal-insulator transition in a weakly interacting many-electron system with localized single-particle states, *Ann. Phys.* **321**, 1126 (2006).
[25] D. V. Averin and A. N. Korotkov, Influence of discrete energy spectrum on correlated single-electron tunneling via a mezoscopically small metal granule, *Zh. Eksp. Teor. Fiz.* **97**, 1661 (1990).
[26] L. P. Kouwenhoven *et al.*, Single electron charging effects in semiconductor quantum dots, *Z. Phys. B Con. Mat.* **85**, 367 (1991).
[27] L. P. Kouwenhoven, D. G. Austing, and S. Tarucha, Few-electron quantum dots, *Rep. Prog. Phys.* **64**, 701 (2001).
[28] O. Agam *et al.*, Chaos, interactions, and nonequilibrium effects in the tunneling resonance spectra of ultrasmall metallic particles, *Phys. Rev. Lett.* **78**, 1956 (1997).
[29] U. Sivan, Y. Imry, and A. G. Aronov, Quasi-particle lifetime in a quantum dot, *Europhys. Lett.* **28**, 115 (1994).
[30] Y. M. Blanter, Electron-electron scattering rate in disordered mesoscopic systems, *Phys. Rev. B* **54**, 12807 (1996).
[31] J. Rammer and H. Smith, Quantum field-theoretical methods in transport theory of metals, *Rev. Mod. Phys.* **58**, 323 (1986).
[32] A.-P. Jauho, N. S. Wingreen, and Y. Meir, Time-dependent transport in interacting and noninteracting resonant-tunneling systems, *Phys. Rev. B* **50**, 5528 (1994).
[33] H. Haug and A.-P. Jauho, *Quantum kinetics in transport and optics of semiconductors* (Springer, Berlin, 1998).
[34] G. Kiršanskas *et al.*, QmeQ 1.0: An open-source Python package for calculations of transport through quantum dot devices, *Comput. Phys. Commun.* **221**, 317 (2017).

5.6 Summary

This chapter demonstrated how quantum dots are a useful system for studying the effects of many-body localisation as they undergo an analogous transition of localisation in Fock space. One of the most common ways to deal with a quantum dot in the classical Coulomb blockade regime is through a master equation and typically the classical master equation is used when there are a large number of particles on the dot. This correctly predicts the Coulomb staircase in the presence of instantaneous thermalisation on the dot and strong asymmetry in the coupling to the leads. In the publication *Coulomb staircase in an asymmetrically coupled quantum dot* [25], the Keldysh formalism is used to explore the staircase in the absence of thermalisation. When the Fermi energy of the dot is much larger than the charging energy, the usual Coulomb staircase is recovered due to the formation of an equilibrium with the lead most strongly coupled to the dot. However, for a much smaller Fermi energy, the staircase practically vanishes for a large number of electrons on the dot, as the low-lying energy levels of the dot dominate the transport. Therefore, if there is to be a clear signature of the absence of thermalisation in the I-V characteristics it will be in the case of symmetric coupling where it would be expected that an equilibrium will not be established with one lead. This will be the topic of discussion in the next chapter.

CHAPTER 6

QUANTUM DOTS - SYMMETRIC COUPLING TO THE LEADS

The previous chapter illustrated that in the case of a quantum dot asymmetrically coupled to the lead, the Coulomb staircase is recovered in the limit of a large Fermi energy on the dot. In this instance, there is no difference between the cases of full thermalisation and its complete absence, as an equilibrium is established with the strongly coupled lead. In the case of symmetric coupling, however, there is no reason why such an equilibrium should be established as electrons enter the dot from the left and right leads with similar rates. This will be addressed in this chapter.

6.1 Thermalisation in One-Dimensional Wires

The absence of thermalisation has previously been considered in one-dimensional wires [137], where it was found that on short enough length scales electrons do not thermalise and a double-step distribution characterises the electrons through the wire. By attaching wires of different lengths to two leads and measuring the differential conductance at different points along the wire (see Fig. 6.1), the authors were able to identify that the distribution function varied depending on the amount of thermalisation occurring in the system.

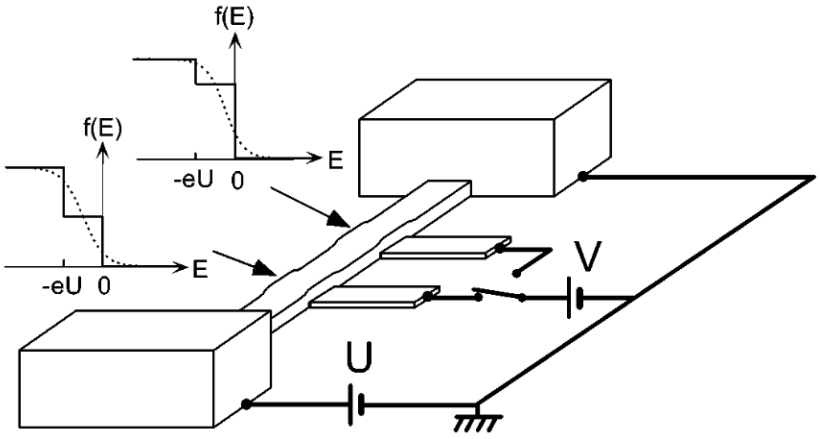

Figure 6.1: The absence of thermalisation in 1d wires. A wire was placed between two leads with a potential difference of U. Different distribution functions can be found at different points along the wire in the absence of inelastic scattering. Figure taken from [137].

In the absence of all inelastic scattering, the distribution function is simply a linear combination of the two leads and results in a different distribution function depending on how far along the wire it is observed. For a wire of unit length, the distribution function has a double-step form and varies with the position along the wire, x, as [137]

$$F(x,\varepsilon) = (1-x)f(\varepsilon) + xf(\varepsilon + eU), \tag{6.1}$$

where the f's are standard Fermi functions and U is the potential difference between the two leads. In the opposite limit of strong inelastic scattering, the wire will have a distribution function in which the intermediate step is smeared out. It has a Fermi function form with a chemical potential and temperature that depends on the distance along the wire and the size of U. Both of these limiting cases were observed with the double-step being seen in shorter wires where insufficient scattering occurs to thermalise the electrons and the smeared distribution was present in longer wires [137].

Intuitively a similar outcome would be expected in a quantum dot in the non-linear regime, where in the absence of inelastic scattering a dot coupled to two leads would form a double-step style distribution. For a non-interacting dot the distribution is simply a

linear combination of the Fermi functions of the two leads (left, L, and right, R) [82, 85]

$$F(\varepsilon) = \frac{\Gamma_{\mathrm{L}}}{\Gamma} f_{\mathrm{L}}(\varepsilon) + \frac{\Gamma_{\mathrm{R}}}{\Gamma} f_{\mathrm{R}}(\varepsilon). \tag{6.2}$$

The effect of interactions is explored in the manuscript *Coulomb blockade in a non-thermalized quantum dot* [26] in the next section. Such an analysis is vital for understanding the effect of the absence of thermalisation in quantum dots - a regime that is particularly relevant for the localisation of electrons on the dot.

6.2 *Coulomb blockade in a non-thermalized quantum dot*

The manuscript for the publication *Coulomb blockade in a non-thermalized quantum dot* authored by myself, Rose Davies, Igor V. Lerner and Igor V. Yurkevich features below. As first author, I performed the analytical calculations and most of the numerical calculations with help from Rose Davies. I wrote the majority of the manuscript with assistance from the other co-authors on writing and editing. Igor V. Lerner and Igor V. Yurkevich additionally provided help with the direction of the project. A version of this manuscript can be found on arXiv [26].

Coulomb blockade in a non-thermalized quantum dot

G. McArdle,[1] R. Davies,[2] I. V. Lerner,[1] and I. V. Yurkevich[2]

[1] *School of Physics and Astronomy, University of Birmingham, Birmingham, B15 2TT*
[2] *School of Informatics and Digital Engineering, Aston University, Birmingham, B4 7ET*

(Dated: October 5, 2023)

We investigate non-equilibrium transport properties of a quantum dot in the Coulomb blockade regime under the condition of negligible inelastic scattering during the dwelling time of the electrons in the dot. Using the quantum kinetic equation we show that the absence of thermalization leads to a double-step in the distribution function of electrons on the dot, provided that it is symmetrically coupled to the leads. This drastically changes nonlinear transport through the dot resulting in an additional (compared to the thermalized case) jump in the conductance at voltages close to the charging energy, which could serve as an experimental manifestation of the absence of thermalization.

Many-body localization (MBL), predicted for disordered many-electron systems which are not thermalized with the environment [1, 2], has attracted a lot of theoretical and experimental attention (for a review see [3]) and has been observed in systems of ultracold atoms [4]. One of the defining properties of MBL is the absence of thermalization [5, 6].

Prior to the MBL papers [1, 2], a similar regime of localization in Fock space was predicted for quantum dots [7] where electrons fail to mutually equilibrate as their dwelling time on the dot, $\tau_{\rm dw}$, is much shorter than the equilibration time $\tau_{\rm eq}$. Alternatively, this condition can be formulated as

$$\gamma \ll \Gamma, \tag{1}$$

where $\gamma \sim 1/\tau_{\rm eq}$ is the equilibration rate and $\Gamma \sim 1/\tau_{\rm dw}$ is the tunneling rate. For a zero-dimensional diffusive dot, the electron-electron equilibration rate [7–9],

$$\gamma \approx \Delta \left(\frac{\varepsilon}{g\Delta}\right)^2, \tag{2}$$

can be sufficiently small provided that $\sqrt{g}\Delta < \varepsilon < g\Delta$, where ε is the quasiparticle energy, Δ is the mean level spacing on the dot, and $g\Delta$ is the Thouless energy of the dot with dimensionless conductance $g \gg 1$.

In this Letter, we show that such an absence of thermalization leads to striking changes in nonlinear transport in the Coulomb blockade regime, where electrons are loaded one-by-one into a quantum dot due to the charging energy, $E_{\rm c} = e^2/C$, of a dot of capacitance C, preventing a continuous flow. We assume the separation of scales typical for the classical Coulomb blockade at a temperature T (see [10–12] for reviews):

$$\Gamma \ll \Delta \ll T \ll E_{\rm c}. \tag{3}$$

Typically, the study of quantum dots in the Coulomb blockade regime has been focused on the regime where complete thermalization is assumed. This regime is characterized by peaks in the conductance as a function of gate voltage [13, 14] that can be attributed to interesting features in the tunneling density of states [15], and – in case of strong asymmetry in the coupling to the leads – by a staircase in the current as a function of the bias voltage V [16–19]. When the coupling is approximately symmetric, $\Gamma_{\rm L} \sim \Gamma_{\rm R}$, the Coulomb staircase practically vanishes in the thermalized case. But it is precisely in this case when the absence of thermalization reveals itself by an additional jump in the nonlinear differential conductance, as we show in this Letter by solving the quantum kinetic equation. The absence of thermalization on a dot, therefore, can be detected by this jump which occurs within the first step of the Coulomb staircase.

The jump arises due to the change in the distribution function of the dot; going from a Fermi function in the fully thermalized case to a double-step form. A similar structure (although for practically noninteracting electrons) has previously been observed in one-dimensional wires where the distribution function was a linear combination of the two Fermi functions of the leads due to insufficient time for equilibration [20]. A double-step distribution has also been predicted for open quantum dots, where electrons are practically noninteracting [21], and for auxiliary non-interacting electrons in the slave-boson approach to the Kondo effect in quantum dots [22]. Here, in the Coulomb-blockade regime in region (3), a double-step form of the electron distribution function is substantially modified by the interaction.

The standard Hamiltonian of a Coulomb-blockaded quantum dot coupled to two leads is $H = H_{\rm dot} + H_{\rm l} + H_{\rm tun}$, where

$$H_{\rm dot} = \sum_n \varepsilon_n d_n^\dagger d_n + \tfrac{1}{2} E_{\rm c}\big(\hat{N} - N_{\rm g}\big)^2, \tag{4a}$$

$$H_{\rm l} = \sum_{k,\alpha} (\varepsilon_k - \mu_\alpha) c_{k,\alpha}^\dagger c_{k,\alpha}, \tag{4b}$$

$$H_{\rm tun} = \sum_{k,n,\alpha} \big(t_\alpha c_{k,\alpha}^\dagger d_n + \text{h.c.}\big). \tag{4c}$$

Here α=L, R labels the leads, $d_n^\dagger(d_n), c_{k,\alpha}^\dagger(c_{k,\alpha})$ are the creation (annihilation) operators for electrons with energies ε_n and ε_k in the dot and leads respectively, $\hat{N} = \sum_n d_n^\dagger d_n$ is the number operator for the dot, and $N_{\rm g}$

is the preferred number of electrons on the dot set by the gate voltage. The leads have chemical potentials $\mu_{\rm L}=\mu+eV$ and $\mu_{\rm R}=\mu$. The k- and n-independent tunneling amplitudes between the dot and leads, t_α, define, along with the density of states of the leads ν_α (taken to be constant), the tunneling rates $\Gamma_\alpha=2\pi\nu_\alpha|t_\alpha|^2$ with the total $\Gamma=\Gamma_{\rm L}+\Gamma_{\rm R}$.

In addition to inequalities (3), we assume that the Fermi energy of the dot is much larger than the charging energy, $\varepsilon_{\rm F}\gg E_{\rm c}$, to ensure that only electrons in a relatively narrow energy strip around $\varepsilon_{\rm F}$ contribute the transport properties of the system. This assumption is also utilized in the orthodox theory of the Coulomb blockade [14, 16–19] and is achievable in experiments [10, 23]. By starting with the standard expression for tunneling current [24] and assuming current conservation, we express the current across a quantum dot in the Coulomb blockade regime in the region (3) as

$$I=e\frac{\Gamma_{\rm L}\Gamma_{\rm R}}{\Gamma}\sum_{N,n}p_N\Big(F_N(\varepsilon_n)\left[f_{\rm L}(\varepsilon_n+\Omega_{N-1})-f_{\rm R}(\varepsilon_n+\Omega_{N-1})\right]+(1-F_N(\varepsilon_n))\left[f_{\rm L}(\varepsilon_n+\Omega_N)-f_{\rm R}(\varepsilon_n+\Omega_N)\right]\Big), \quad (5)$$

with details of the derivation in *Supplemental Material*. Here p_N is the probability of N electrons being on the dot, $F_N(\varepsilon_n)$ is their distribution function, and $f_{\rm L,R}(\varepsilon_n)$ are Fermi functions in the leads with chemical potentials $\mu_{\rm L}=\mu+eV$ and $\mu_{\rm R}=\mu=\varepsilon_{\rm F}$ respectively. The presence of the charging energy is encapsulated by

$$\Omega_N=E_{N+1}-E_N=E_{\rm c}\left(N+\tfrac{1}{2}-N_{\rm g}\right), \quad (6)$$

where $E_N=\frac{1}{2}E_{\rm c}(N-N_{\rm g})^2$.

The current through a thermalized quantum dot is usually considered with the help of a master equation [13, 14, 16–19] involving electrons of all energies. In the non-thermalized regime (1), the electrons with different energies are not mixed. Hence, the probabilities and distribution functions can be found from the energy-conserving quantum kinetic equation (QKE), which is formulated using the Keldysh formalism (see, e.g., [24–26]) in terms of the "greater", $g^>(t)$, and "lesser", $g^<(t)$, Green's function of the dot. In the regime (3), where the mean level spacing is much larger than the level broadening due to tunneling, they are split into a sum over the energy levels, with Green's function for the $n^{\rm th}$ level given by $g_n^>(t)=-i\langle d_n(t)d_n^\dagger(0)\rangle$ and $g_n^<(t)=i\langle d_n^\dagger(0)d_n(t)\rangle$, where $d_n(t)={\rm e}^{iHt}d_n{\rm e}^{-iHt}$. Then, to linear order in tunneling, the QKE is reduced to [24–26],

$$g_n^>(\varepsilon)\Sigma^<(\varepsilon)=g_n^<(\varepsilon)\Sigma^>(\varepsilon). \quad (7)$$

Here, the conservation of particle number for an isolated dot allows one to represent the single-level Green's functions as (see *Supplemental Material)*

$$g_n^>(\varepsilon)=-2\pi i\sum_N\delta\left(\varepsilon-\varepsilon_n-\Omega_N\right)p_N(1-F_N(\varepsilon_n)),$$
$$g_n^<(\varepsilon)=2\pi i\sum_N\delta\left(\varepsilon-\varepsilon_n-\Omega_{N-1}\right)p_NF_N(\varepsilon_n), \quad (8)$$

with the normalization $\sum_N p_N=1$. The self-energy functions of the leads in Eq. (7) are assumed to be n-independent and are given by

$$\Sigma^>(\varepsilon)=i\sum_{\alpha={\rm L,R}}\Gamma_\alpha(f_\alpha(\varepsilon)-1),\quad \Sigma^<(\varepsilon)=i\sum_{\alpha={\rm L,R}}\Gamma_\alpha f_\alpha(\varepsilon). \quad (9)$$

Substituting Eqs. (8)and (9) into Eq. (7) leads to the QKE reflecting the detailed balance equations, coinciding with those derived in [14] for $\Delta\gg T$,

$$p_{N+1}F_{N+1}(\varepsilon_n)\left(1-\widetilde{f}(\varepsilon_n+\Omega_N)\right)=p_N\left(1-F_N(\varepsilon_n)\right)\widetilde{f}(\varepsilon_n+\Omega_N), \quad (10)$$
$$\widetilde{f}(\varepsilon)=(\Gamma_{\rm L}/\Gamma)f_{\rm L}(\varepsilon)+(\Gamma_{\rm R}/\Gamma)f_{\rm R}(\varepsilon).$$

It is this equation along with the normalization conditions, $\sum_N p_N=1$ and $\sum_n F_N(\varepsilon_n)=N$, that can be used to obtain the probabilities and distribution functions required in Eq. (5) to calculate the current. The results for full thermalization are recovered by summing Eq. (10) over n using the fact that in this case we can substitute the equilibrium distribution function, $F_N(\varepsilon_n)=f(\varepsilon_n-\varepsilon_{\rm F})$.

The absence of thermalization, however, drastically changes the distribution function. In this case, QKE (10) has an exact solution providing there are only two relevant states (N and $N+1$) for a given voltage (see *Supplemental Material*). In the case of approximately equal coupling, this condition can be satisfied only for a finite bias window, i.e. within the first step of the Coulomb staircase. For higher bias, one needs to account for more states with different numbers of particles that are not being exponentially suppressed (in contrast to the asymmetric case when $\Gamma_{\rm L}/\Gamma_{\rm R}\gg 1$ [27]).

Assuming that the chemical potential in the dot is of order of the unbiased chemical potential in the (right) lead, we show that the current and, hence, the differential conductance has an additional peak in the window $0\le eV\lesssim\Omega_{N+1}$ as compared to the thermalized case [16–19]. In this window, where only two levels

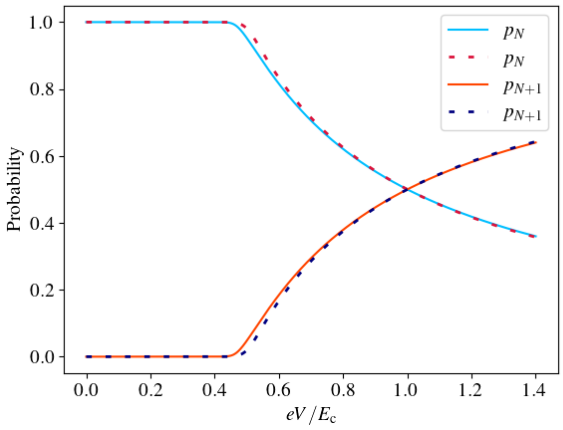

FIG. 1. The occupation probabilities p_N (the upper line) and p_{N+1} (the lower line) as functions of bias voltage, V, for Γ_L=Γ_R, and N=N_g. Here they depend only on the ratio E_c/T in the temperature region $10-100$mK, albeit this dependence is rather weak ($E_c/T = 100$ was used for this figure).The solid lines represent the results for the non-thermalized case, the dashed lines for the full-thermalization case [16–19]. In this temperature range they are practically indistinguishable.

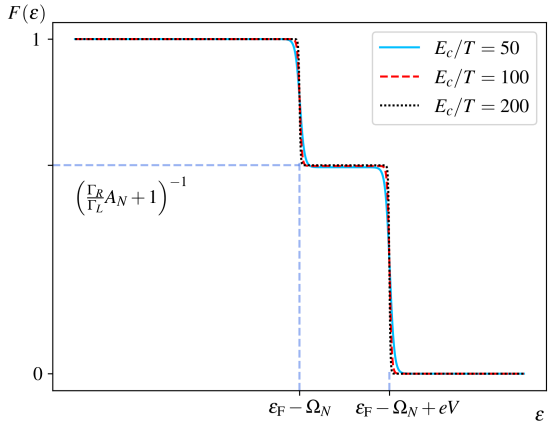

FIG. 2. The electron distribution function in the dot for $\Gamma_L = \Gamma_R$, $N = N_g$, and $eV = 0.8E_c$ where numerically we find $A_N \approx 0.6$. The double-step structure is robust as long as $eV > \Omega_N$ – in the opposite case $A_N \equiv p_{N+1}/p_N \to 0$, as seen from Fig. (1), and the middle step disappears. $F(\varepsilon)$ has only a weak dependence on E_c/T so that the three curves above practically merge.

are relevant, the kinetic equation (10) has the solution $F_N(\varepsilon_n) \approx F_{N+1}(\varepsilon_n) \approx F(\varepsilon_n)$ in the limit $N \gg 1$, leading to

$$F(\varepsilon_n) = \frac{\widetilde{f}(\varepsilon_n + \Omega_N)}{[1 - \widetilde{f}(\varepsilon_n + \Omega_N)]A_N + \widetilde{f}(\varepsilon_n + \Omega_N)}, \qquad (11)$$

where $A_N = p_{N+1}/p_N$. This ratio of probabilities is found from normalization, $N = \sum_n F(\varepsilon_n) = (1/\Delta)\int_0^\infty F(\varepsilon)\mathrm{d}\varepsilon$, while $p_N + p_{N+1} = 1$ as shown in *Supplemental Material*. As seen in Fig. (1), depicted for the middle of the Coulomb blockade valley where $\Omega_N = E_c/2$, both p_N and p_{N+1} are practically indistinguishable from the thermalized case. It remains the case as long as Ω_N, Eq. (6), remains far from the peaks of the Coulomb blockade. Note that this and all subsequent results depend only on ratios of energetic parameters and are fully applicable in experimental regimes where $T \sim 10 - 100$mK and $E_c \sim 1$meV.

On the contrary, the distribution function, found by substituting the ratio $A_N \equiv p_{N+1}/p_N$ into Eq. (11), acquires an additional step

$$F(\varepsilon_n) \approx \begin{cases} 1, & \varepsilon_n < \mu_R - \Omega_N \\ \left(1 + \frac{\Gamma_R}{\Gamma_L} A_N\right)^{-1}, & \mu_R - \Omega_N < \varepsilon_n < \mu_L - \Omega_N \\ 0. & \mu_L - \Omega_N < \varepsilon_n \end{cases} \qquad (12)$$

as depicted for the middle of the valley in Fig. 2. Such a double-step is similar to that observed in short quasi-one-dimensional wires [20]. However, in the wire the double-step was simply a linear combination of the two Fermi-functions of the leads, while in the present case it is substantially affected by the Coulomb interaction. Still, in both cases the double-step reflects the lack of thermalization between electrons coming from the left and right leads. In the steady-state limit, electrons from both leads enter the dot at two different chemical potentials and thermalize with the opposite lead only after exiting the dot. Note that the double-step is effectively washed out in the one-lead limit of the Coulomb blockade when $\Gamma_R/\Gamma_L \ll 1$.

The double-step distribution in the dot drastically changes the differential conductance, $G = \mathrm{d}I/\mathrm{d}V$, in comparison with the thermalized case [16–19]. Substituting p_N and $F(\varepsilon_n)$ into Eq. (5) with $F_N(\varepsilon_n) \approx F(\varepsilon_n)$, we find G as shown in Fig. 3. For small voltages, $eV < E_c$, the absence of thermalization has little impact in the low-T limit. However, at $eV = E_c$, there appears a secondary jump in the non-thermalized case. It is robust as long as the tunneling is symmetric, $\Gamma_L \approx \Gamma_R$, when there are three distinct regions for the distribution, Eq. (12). Rewriting Eq. (5) for the current in the low-T limit and for $eV \lesssim \Omega_{N+1}$ will make this clearer:

$$I = \frac{e}{\Delta}\frac{\Gamma_L\Gamma_R}{\Gamma}\Big(p_N \int_{\mu-\Omega_{N-1}}^{\mu-\Omega_{N-1}+eV} F(\varepsilon)\mathrm{d}\varepsilon + \int_{\mu-\Omega_N}^{\mu-\Omega_N+eV} \big[p_N(1-F(\varepsilon)) + p_{N+1}F(\varepsilon)\big]\mathrm{d}\varepsilon + p_{N+1}\int_{\mu-\Omega_{N+1}}^{\mu-\Omega_{N+1}+eV}(1-F(\varepsilon))\mathrm{d}\varepsilon\Big). \qquad (13)$$

The second integration over the middle step starts to con-

tribute at $eV \geqslant E_c/2$ when p_N and p_{N+1} start to change, see Fig. 1, signaling that the oncoming particle is sufficiently energetic to overcome the charging energy. This results in the usual blockade jump which is the same for both the thermalized and non-thermalized cases. As long as $eV < E_c$, the first and third integrals in Eq. (13) are negligible as the each integration is over a region where the integrands are exponentially small at $T \ll E_c$. For $eV \geqslant E_c$, this is no longer the case and the appropriate non-zero contribution results in a sudden change in the current revealed as a jump in the differential conductance at $eV = E_c$.

The position of this jump is insensitive to gate voltage as it only depends on the difference $\Omega_{N+1} - \Omega_N = E_c$. In the region around the jump, the ratio of probabilities is given for $T \ll E_c$ (see *Supplemental Material*) by

$$A_N \equiv \frac{p_{N+1}}{p_N} \approx \frac{\Gamma_L}{\Gamma_R}\left(\frac{eV - \Omega_N}{\Omega_N}\right). \tag{14}$$

Then, calculating the current from Eq. (13) on both sides of the jump we find that the jump in the differential conductance, neglecting corrections in T/E_c, has the height

$$\delta G = \frac{e^2}{2\Delta}\frac{\Gamma_L\Gamma_R}{\Gamma}, \tag{15}$$

in the middle of the Coulomb blockade valley, $\Omega_N = \frac{1}{2}E_c$. (The general expression for δG is given in *Supplemental Material*). This jump is rather robust: it occurs at $eV = E_c$ independently of Ω_N and has only a weak temperature dependence. As the temperature is increased, while still obeying inequalities (3), the jump is only slightly smeared across a wider range of voltages as shown in the inset in Fig. (3). This jump should be experimentally observable and give a clear indication of the absence of thermalization within a quantum dot.

In conclusion we note that the existence of additional fine structure of the Coulomb blockade peaks has been established numerically and experimentally [28] for small dots, where $\Delta \gg T$. Here we have considered the opposite case of large quantum dots, (3), where we have shown that the absence of thermalization manifests itself as an additional jump in the differential conductance at $eV = E_c$, which follows the usual jump at $eV = \Omega_N$. This is a direct consequence of the lack of equilibration between electrons coming from the left and right leads so that the distribution function on the dot has a double-step form. We anticipate this jump to be experimentally accessible at the appropriate voltages and therefore could be used as a method of identifying the absence of thermalization in the dot.

We gratefully acknowledge support from EPSRC under the grant EP/R029075/1 (IVL) and from the Leverhulme Trust under the grant RPG-2019-317 (IVY).

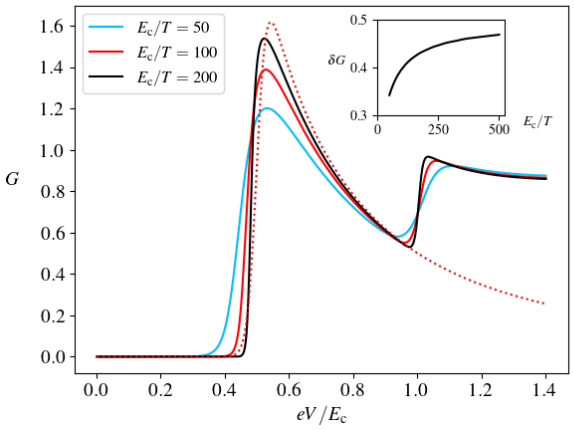

FIG. 3. The differential conductance, $G(V)$, in units of $\frac{e^2}{\Delta}\frac{\Gamma_L\Gamma_R}{\Gamma} \approx \frac{e^2\Gamma}{4\Delta}$ when $\Gamma_L \approx \Gamma_R$. For $\Gamma_L \sim \Gamma_R$, an additional jump in G is always at $eV = E_c$. Such a jump is absent in the thermalized case [16–19], depicted here by the dotted line for $E_c/T = 100$. The dependence of its height, δG, on the ratio E_c/T, is shown in the inset.

[1] D. Basko, I. Aleiner, and B. Altshuler, *Annals of Physics* **321**, 1126 (2006).
[2] I. V. Gornyi, A. D. Mirlin, and D. G. Polyakov, *Phys. Rev. Lett.* **95**, 206603 (2005).
[3] D. A. Abanin and Z. Papić, *Annalen der Physik* **529**, 1700169 (2017).
[4] M. Schreiber *et al.*, *Science* **349**, 842 (2015).
[5] R. Nandkishore and D. A. Huse, *Annual Review of Condensed Matter Physics* **6**, 15 (2015).
[6] M. Serbyn, D. A. Abanin, and Z. Papić, *Nature Physics* **17**, 675 (2021).
[7] B. L. Altshuler, Y. Gefen, A. Kamenev, and L. S. Levitov, *Phys. Rev. Lett.* **78**, 2803 (1997).
[8] U. Sivan, Y. Imry, and A. G. Aronov, *Europhys. Lett.* **28**, 115 (1994).
[9] Y. M. Blanter, *Phys. Rev. B* **54**, 12807 (1996).
[10] L. P. Kouwenhoven *et al.*, in *Mesoscopic Electron Transport*, edited by L. L. Sohn, L. P. Kouwenhoven, and G. Schön (Springer Netherlands, Dordrecht, 1997), pp. 105–214.
[11] I. L. Aleiner, P. W. Brouwer, and L. I. Glazman, *Phys. Rep.* **358**, 309 (2002).
[12] Y. Alhassid, *Rev. Mod. Phys.* **72**, 895 (2000).
[13] D. V. Averin and K. K. Likharev, *Journal of Low Temperature Physics* **62**, 345 (1986).
[14] C. W. J. Beenakker, *Phys. Rev. B* **44**, 1646 (1991).
[15] N. Sedlmayr, I. V. Yurkevich, and I. V. Lerner, *Europhys. Lett.* **76**, 109 (2006).
[16] I. O. Kulik and R. I. Shekhter, *Zh. Eksp. Teor. Fiz.* **68**, 623 (1975).
[17] D. Averin and K. Likharev, in *Mesoscopic Phenomena in Solids*, Vol. 30 of *Modern Problems in Condensed Matter Sciences*, edited by B. Altshuler, P. Lee, and R. Webb (Elsevier, Amsterdam, 1991), pp. 173–271.

[18] M. Amman *et al.*, *Phys. Rev. B* **43**, 1146 (1991).
[19] D. V. Averin, A. N. Korotkov, and K. K. Likharev, *Phys. Rev. B* **44**, 6199 (1991).
[20] H. Pothier *et al.*, *Phys. Rev. Lett.* **79**, 3490 (1997).
[21] A. Altland and R. Egger, *Phys. Rev. Lett.* **102**, 026805 (2009).
[22] S. Smirnov and M. Grifoni, *Phys. Rev. B* **84**, 125303 (2011).
[23] L. P. Kouwenhoven *et al.*, *Z. Phys. B Con. Mat.* **85**, 367 (1991).
[24] A.-P. Jauho, N. S. Wingreen, and Y. Meir, *Phys. Rev. B* **50**, 5528 (1994).
[25] J. Rammer and H. Smith, *Rev. Mod. Phys.* **58**, 323 (1986).
[26] H. Haug and A.-P. Jauho, *Quantum kinetics in transport and optics of semiconductors* (Springer, Berlin, 1998).
[27] G. McArdle, R. Davies, I. V. Lerner, and I. V. Yurkevich, *Journal of Physics: Condensed Matter* **35**, 475302 (2023).
[28] O. Agam *et al.*, *Phys. Rev. Lett.* **78**, 1956 (1997).

Supplemental material for Coulomb blockade in a non-thermalized quantum dot

G. McArdle,[1] R. Davies,[2] I. V. Lerner,[1] and I. V. Yurkevich[2]

[1] *School of Physics and Astronomy, University of Birmingham, Birmingham, B15 2TT*
[2] *School of Informatics and Digital Engineering, Aston University, Birmingham, B4 7ET*

GREEN'S FUNCTIONS FOR AN ISOLATED QUANTUM DOT AND THE INCORPORATION OF TUNNELING TO THE LEADS

The Green's function for an isolated dot can be found explicitly, as we demonstrate below and then in the limit of weak coupling to the leads, the quantum kinetic equation can be derived using the non-equilibrium Keldysh formalism (see, e.g., [S1–S3]), allowing the Green's function of the dot coupled to leads to be found. In the limit where the broadening of the levels due to tunneling to and from the leads, Γ, is much less than the mean level spacing, Δ, then the Green's functions of a dot, $g(\varepsilon)$ can be expressed as a sum over the Green's functions for individual energy levels, n, so that $g(\varepsilon) = \sum_n g_n(\varepsilon)$. The greater and lesser functions are given by $g_n^>(t) = -i\langle d_n(t) d_n^\dagger(0)\rangle$ and $g_n^<(t) = i\langle d_n^\dagger(0) d_n(t)\rangle$ respectively, where $d_n(t) = \mathrm{e}^{iHt} d_n(0) \mathrm{e}^{-iHt}$ annihilates an electron on the dot. In the case of an isolated dot, the Hamiltonian is given by Eq. (4a) of the main text, which ensures that the number of electrons on the dot, N, is conserved allowing the Green's functions to be expressed as sums over N,

$$g_n^>(\varepsilon) = -i \sum_N \mathrm{Tr}_N \left(\hat{\rho}_0 \mathrm{e}^{iHt} d_n \mathrm{e}^{-iHt} d_n^\dagger(0) \right), \tag{S1}$$

$$g_n^<(\varepsilon) = i \sum_N \mathrm{Tr}_N \left(\hat{\rho}_0 d_n^\dagger(0) \mathrm{e}^{iHt} d_n \mathrm{e}^{-iHt} \right). \tag{S2}$$

Here $\hat{\rho}_0$ is the density matrix for an isolated dot and Tr_N is the trace in the subspace where there are N electrons on the dot. Explicit evaluation of these leads to, after Fourier transforming, the Green's functions of the isolated dot [S4]

$$g_n^>(\varepsilon) = -2\pi i \sum_N \delta\left(\varepsilon - \varepsilon_n - \Omega_N\right) g_N^>(\varepsilon_n), \qquad g_N^>(\varepsilon_n) = \mathrm{Tr}_N \left(\hat{\rho}_0 d_n d_n^\dagger \right), \tag{S3}$$

$$g_n^<(\varepsilon) = -2\pi i \sum_N \delta\left(\varepsilon - \varepsilon_n - \Omega_{N-1}\right) g_N^<(\varepsilon_n), \qquad g_N^<(\varepsilon_n) = -\mathrm{Tr}_N \left(\hat{\rho}_0 d_n^\dagger d_n \right). \tag{S4}$$

By defining the probability of having N electrons on the dot, p_N, and the associated distribution function for this number of electrons, $F_N(\varepsilon_n)$, we use the ansatz $g_N^>(\varepsilon_n) = p_N\left(1 - F_N(\varepsilon_n)\right)$ and $g_N^<(\varepsilon_n) = -p_N F_N(\varepsilon_n)$. This leads to the results in Eq. (8) of the main text. In order to incorporate the tunneling to the leads, the standard quantum kinetic equation is used for each level on the dot [S1–S3]

$$g_n^{>,<}(\varepsilon) = g_n^{\mathrm{R}}(\varepsilon)\, \Sigma^{>,<}(\varepsilon)\, g_n^{\mathrm{A}}(\varepsilon). \tag{S5}$$

where we have used that the full Green's function of the dot can be replaced by that of the isolated dot in the weak coupling limit, $\Gamma \to 0$. Combining the two equations in Eq. (S5) leads to the form of the kinetic equation given in Eq. (7) of the main text,

$$g_n^>(\varepsilon)\Sigma^<(\varepsilon) = g_n^<(\varepsilon)\Sigma^>(\varepsilon). \tag{S6}$$

Upon substitution of the forms of the Green's functions and self-energies laid out in the main text (Eq.(8) and (9) respectively), the QKE has the form

$$p_{N+1} F_{N+1}(\varepsilon_n) \left(1 - \widetilde{f}(\varepsilon_n + \Omega_N)\right) = p_N \left(1 - F_N(\varepsilon_n)\right) \widetilde{f}(\varepsilon_n + \Omega_N), \tag{S7}$$

$$\widetilde{f}(\varepsilon) = (\Gamma_{\mathrm{L}}/\Gamma) f_{\mathrm{L}}(\varepsilon) + (\Gamma_{\mathrm{R}}/\Gamma) f_{\mathrm{R}}(\varepsilon).$$

similar to the detailed balance relations derived in [S5].

The results of the QKE, that is p_N and $F_N(\varepsilon)$ can then be subsequently used to calculate the current. To see this, consider the standard expression for tunneling current going from the dot to the lead, α [S1]

$$I_\alpha = -ie\Gamma_\alpha \int \frac{\mathrm{d}\varepsilon}{2\pi} \left(g^<(\varepsilon) + f_\alpha(\varepsilon) \left[g^>(\varepsilon) - g^<(\varepsilon) \right] \right). \tag{S8}$$

After substitution of the dot Green's functions in Eq. (S3, S4) along with the corresponding ansatz, into this formula for the current, then the current can be expressed as

$$I_\alpha = e\Gamma_\alpha \sum_N p_N \sum_n \Big(F_N(\varepsilon_n)[1 - f_\alpha(\varepsilon_n + \Omega_{N-1})] - [1 - F_N(\varepsilon_n)] f_\alpha(\varepsilon_n + \Omega_N) \Big). \tag{S9}$$

By utilising current conservation, the current can then be expressed as

$$I = e\frac{\Gamma_\mathrm{L}\Gamma_\mathrm{R}}{\Gamma} \sum_{N,n} p_N \Big(F_N(\varepsilon_n) \left[f_\mathrm{L}(\varepsilon_n + \Omega_{N-1}) - f_\mathrm{R}(\varepsilon_n + \Omega_{N-1}) \right] + (1 - F_N(\varepsilon_n)) \left[f_\mathrm{L}(\varepsilon_n + \Omega_N) - f_\mathrm{R}(\varepsilon_n + \Omega_N) \right] \Big), \tag{S10}$$

as is presented in Eq.(5) of the main text. We have calculated the current in the case when only two consecutive occupation numbers, say N and $N+1$, contribute, but the above equation is applicable more generally. Outside the Coulomb blockade regime, specified by inequalities (3), one just needs to modify Eq.(6) for Ω_N.

FULL SOLUTION TO THE QUANTUM KINETIC EQUATION

In order to calculate the current through the quantum dot using Eq. (5) of the main text, it is necessary to find the probability that it has N electrons, p_N, and the distribution function given that it has N electrons, $F_N(\varepsilon)$. To do this, we make use of the quantum kinetic equation (QKE) which for a quantum dot in the Coulomb blockade regime coupled to two leads is given by Eq. (10) in the main text

$$p_N \left(1 - F_N(\varepsilon_n)\right) \tilde{f}(\varepsilon_n + \Omega_N) = p_{N+1} F_{N+1}(\varepsilon_n) \left(1 - \tilde{f}(\varepsilon_n + \Omega_N) \right). \tag{S11}$$

In this equation, $\tilde{f}(\varepsilon) = \frac{\Gamma_\mathrm{L}}{\Gamma} f_\mathrm{L}(\varepsilon) + \frac{\Gamma_\mathrm{R}}{\Gamma} f_\mathrm{R}(\varepsilon)$ and the absence of thermalization on the dot has been assumed. Providing there are only two states whose probabilities aren't exponentially suppressed this has a solution in which $F_N(\varepsilon_n) \approx F_{N+1}(\varepsilon_n) \approx F(\varepsilon_n)$. The probabilities are then found from the normalization conditions,

$$\int_0^\infty F_N(\varepsilon)\mathrm{d}\varepsilon = N\Delta \equiv \varepsilon_\mathrm{F}, \quad \sum_N p_N = 1, \tag{S12}$$

where the energies in the dot are counted from the bottom of the band and the normalization of the probabilities can be written as $p_N + p_{N+1} \approx 1$. This solution is valid in the limit $N \gg 1$ and here we demonstrate how this solution is obtained using the saddle point approximation as we achieved in [S4]. When there are only two relevant probabilities, Eq. (S11) has an exact solution

$$\begin{aligned} p_N &= \frac{Z_N}{Z_N + Z_{N+1}}, \qquad p_{N+1} = \frac{Z_{N+1}}{Z_N + Z_{N+1}}, \\ F_N(\varepsilon_n) &= \frac{Z_N(\varepsilon_n)}{Z_N}, \qquad F_{N+1}(\varepsilon_n) = \frac{Z_{N+1}(\varepsilon_n)}{Z_{N+1}}. \end{aligned} \tag{S13}$$

Introducing

$$\varphi(\varepsilon) = \frac{\tilde{f}(\varepsilon)}{1 - \tilde{f}(\varepsilon)}, \tag{S14}$$

Z_N and Z_{N+1} are defined as

$$Z_N = \sum_{\{n_j=0,1\}} \prod_{j=1}^{\infty} [\varphi(\varepsilon_j + \Omega_N)]^{n_j} \, \delta_{(\sum_j n_j),N},$$
$$Z_{N+1} = \sum_{\{n_j=0,1\}} \prod_{j=1}^{\infty} [\varphi(\varepsilon_j + \Omega_N)]^{n_j} \, \delta_{(\sum_j n_j),N+1}. \tag{S15}$$

Then $Z_N(\varepsilon_n)$ and $Z_{N+1}(\varepsilon_n)$, required for calculating the distribution functions in Eq. (S13), are found by restricting the sums in Eq. (S15) to terms where the level ε_n is occupied. We stress that in these definitions the relevant N dependence enters only via the Krönecker delta's as both Z_N and Z_{N+1} contain $\varphi(\varepsilon_j + \Omega_N)$, reflecting the fact that the two states are coupled via the QKE, Eq. (S11), which contains $\tilde{f}(\varepsilon_n + \Omega_N)$. The Krönecker delta can be written as an integral

$$\delta_{(\sum_j n_j),N} = \int \frac{\mathrm{d}\theta}{2\pi} \mathrm{e}^{i\theta\left(\sum_j n_j - N\right)}, \tag{S16}$$

meaning that Z_N can be written in a form which we evaluate using the saddle-point approximation.

$$Z_N = \int \frac{\mathrm{d}\theta}{2\pi} \mathrm{e}^{N f(\theta)}, \qquad f(\theta) = \frac{1}{N} \sum_j \ln\left(1 + \varphi(\varepsilon_j + \Omega_N)\mathrm{e}^{i\theta}\right) - i\theta. \tag{S17}$$

Recalling that the density of states in the dot is approximately the inverse of the mean level spacing, Δ^{-1}, we write the sum in the definition of $f(\theta)$ as an integral, so that the saddle point, θ_0, is determined by the equation

$$\varepsilon_{\mathrm{F}} = \int_0^{\infty} \mathrm{d}\varepsilon \frac{\varphi(\varepsilon + \Omega_N)}{\varphi(\varepsilon + \Omega_N) + \mathrm{e}^{-i\theta_0}}. \tag{S18}$$

Despite the presence of Ω_N, the relevant N dependence of θ_0 enters only via $\varepsilon_{\mathrm{F}} \equiv N\Delta$, as there is no change in Ω_N going from Z_N to Z_{N+1}. Therefore we write $Z_N = g(\theta_0)\mathrm{e}^{-iN\theta_0}$, where $g(\theta_0)$ is a function depending on N only through ε_{F}. In the limit $N \gg 1$, $N\Delta \approx (N+1)\Delta$, so that ε_{F} is approximately a constant and consequently $g(\theta_0)$ is approximately the same for Z_N and Z_{N+1}. Therefore we find, after using Eq. (S13), that

$$\frac{p_{N+1}}{p_N} = \mathrm{e}^{-i\theta_0}, \quad F_N(\varepsilon_n) \approx F_{N+1}(\varepsilon_n) \approx \left(\frac{\mathrm{e}^{-i\theta_0}}{\varphi(\varepsilon + \Omega_N)} + 1\right)^{-1}. \tag{S19}$$

This solution is equivalent to assuming $F_N(\varepsilon_n) \approx F_{N+1}(\varepsilon_n)$ in the QKE, Eq. (S11), with the ratio of probabilities then being given by the normalization of $F_N(\varepsilon_n)$, Eq. (S12) (or equivalently Eq. (S18)). This is the solution presented in the main text.

NORMALIZATION OF THE NON-THERMALIZED DISTRIBUTION FUNCTION

In the regime characterized by the inequalities (1) and (3) of the main text, $\widetilde{f}(\varepsilon_n + \Omega_N) = (\Gamma_{\mathrm{L}}/\Gamma) f_{\mathrm{L}}(\varepsilon_n + \Omega_N) + (\Gamma_{\mathrm{R}}/\Gamma) f_{\mathrm{R}}(\varepsilon_n + \Omega_N)$ can be split into three regions,

$$\widetilde{f}(\varepsilon_n + \Omega_N) \approx \begin{cases} 1 - (\Gamma_{\mathrm{R}}/\Gamma)\mathrm{e}^{\beta(\varepsilon_n - (\mu - \Omega_N))}, & \varepsilon_n < \mu - \Omega_N \\ \Gamma_{\mathrm{L}}/\Gamma, & \mu - \Omega_N < \varepsilon_n < \mu - \Omega_N + eV \\ (\Gamma_{\mathrm{L}}/\Gamma)\mathrm{e}^{-\beta[\varepsilon_n - (\mu - \Omega_N + eV)]}, & \mu - \Omega_N + eV < \varepsilon_n. \end{cases} \tag{S20}$$

Using the normalization of $F(\varepsilon_n)$ with $\varepsilon_{\mathrm{F}} = N\Delta$

$$\varepsilon_{\mathrm{F}} = \int_0^{\infty} \mathrm{d}\varepsilon F(\varepsilon_n) = \int_0^{\infty} \mathrm{d}\varepsilon \frac{\widetilde{f}(\varepsilon + \Omega_N)}{[1 - \widetilde{f}(\varepsilon + \Omega_N)]A_N + \widetilde{f}(\varepsilon + \Omega_N)} \tag{S21}$$

and making use of the three regions in Eq. (S20) results in the following equation to determine A_N:

$$\beta\varepsilon_{\mathrm{F}} = \frac{\beta eV}{A_N \frac{\Gamma_{\mathrm{R}}}{\Gamma_{\mathrm{L}}} + 1} + \ln\left(\frac{\Gamma}{\Gamma_{\mathrm{R}} A_N} \mathrm{e}^{\beta(\mu-\Omega_N)} + 1\right) + \ln\left(\frac{\frac{\Gamma_{\mathrm{L}}}{\Gamma} + A_N}{\frac{\Gamma}{\Gamma_{\mathrm{R}}} + A_N}\right). \tag{S22}$$

This equation can be solved numerically across the entire voltage range, $0 \leq eV \lesssim \Omega_{N+1}$ leading to the probabilities p_N and p_{N+1} as shown in Fig. 1 of the main text. In the vicinity of the additional jump in the differential conductance, where $A_N \sim 1$, a useful analytical estimate for A_N can be obtained, which allows for an estimation of the size of the jump not present in the thermalized case [S6–S9]. Since $\mu = \varepsilon_{\mathrm{F}} \gg E_{\mathrm{c}}$, then the first logarithm in Eq. (S22) can be simplified to give

$$\beta\varepsilon_{\mathrm{F}} \approx \frac{\beta eV}{A_N \frac{\Gamma_{\mathrm{R}}}{\Gamma_{\mathrm{L}}} + 1} + \beta(\mu - \Omega_N) + \ln\left(\frac{\Gamma}{\Gamma_{\mathrm{R}} A_N}\right) + \ln\left(\frac{\frac{\Gamma_{\mathrm{L}}}{\Gamma} + A_N}{\frac{\Gamma}{\Gamma_{\mathrm{R}}} + A_N}\right). \tag{S23}$$

The first term on the right-hand side of this equation is of the order $\beta E_{\mathrm{c}} \gg 1$ near the additional jump in conductance and as the arguments of the logarithms are $\mathcal{O}(1)$, then it can be found that close to the jump

$$A_N \approx \frac{\Gamma_{\mathrm{L}}}{\Gamma_{\mathrm{R}}}\left(\frac{eV - \Omega_N}{\Omega_N}\right) \tag{S24}$$

as presented in the main text. By evaluating the current (Eq. (13) of the main text) on either side of the jump, which occurs at $eV = E_{\mathrm{c}}$, the size of the jump in the low temperature limit is found to be,

$$\delta G = \frac{e^2}{\Delta} \frac{\Gamma_{\mathrm{L}}\Gamma_{\mathrm{R}}}{\Gamma} \frac{1 + \frac{\Gamma_{\mathrm{R}}}{\Gamma_{\mathrm{L}}}\tilde{A}_N^2}{(1 + \tilde{A}_N)(1 + \frac{\Gamma_{\mathrm{R}}}{\Gamma_{\mathrm{L}}}\tilde{A}_N)} \tag{S25}$$

with $\tilde{A}_N$ being given by Eq. (S24) evaluated at the position of the jump, $eV = E_{\mathrm{c}}$. This leads to the result of Eq. (15) in the main text for $\Omega_N = E_{\mathrm{c}}/2$.

[S1] A.-P. Jauho, N. S. Wingreen, and Y. Meir, *Phys. Rev. B* **50**, 5528 (1994).
[S2] J. Rammer and H. Smith, *Rev. Mod. Phys.* **58**, 323 (1986).
[S3] H. Haug and A.-P. Jauho, *Quantum kinetics in transport and optics of semiconductors* (Springer, Berlin, 1998).
[S4] G. McArdle, R. Davies, I. V. Lerner, and I. V. Yurkevich, *Journal of Physics: Condensed Matter* **35**, 475302 (2023).
[S5] C. W. J. Beenakker, *Phys. Rev. B* **44**, 1646 (1991).
[S6] D. Averin and K. Likharev, in *Mesoscopic Phenomena in Solids*, Vol. 30 of *Modern Problems in Condensed Matter Sciences*, edited by B. Altshuler, P. Lee, and R. Webb (Elsevier, Amsterdam, 1991), pp. 173–271.
[S7] I. O. Kulik and R. I. Shekhter, *Zh. Eksp. Teor. Fiz.* **68**, 623 (1975).
[S8] M. Amman *et al.*, *Phys. Rev. B* **43**, 1146 (1991).
[S9] D. V. Averin, A. N. Korotkov, and K. K. Likharev, *Phys. Rev. B* **44**, 6199 (1991).

6.3 Future Work - Electronic Noise and MBL

The work presented in the previous section demonstrates a clear way of identifying the absence of thermalisation in quantum dots. This aligns with the other work in this thesis which aims to provide signatures of the absence of thermalisation in electronic systems in order to identify systems where MBL may be observed. When expanding on this work, it is worth exploring the signatures of the MBL phase itself. One signature that has been mentioned in this thesis is the divergence in the electronic noise as the localisation-delocalisation transition is approached [27]. Electronic noise can be defined in terms of the current-current correlation function as [138]

$$S(\omega) = 2\int_{-\infty}^{\infty} \mathrm{d}t' \mathrm{e}^{i\omega t'} \langle \delta I(t) \delta I(t+t') \rangle, \tag{6.3}$$

with $\delta I(t) = I(t) - \langle I \rangle$. This arises due to a variety of reasons[1], for example there is thermal (or equilibrium or Nyquist-Johnson) noise which is due to the thermal fluctuations in the system and leads to the noise being independent of frequency but depending on the conductance, G via

$$S = \frac{4G}{\beta}. \tag{6.4}$$

There is additionally $1/f$ noise that occurs at low frequencies and is believed to be caused by changes in the impurity configuration [14, 142], although this is not the subject of this discussion. An interesting form of noise in mesoscopic systems is shot noise which arises due to the discrete nature of electrons. The electrons passing through the system will have a distribution - the mean of this distribution will be related to the current and the variance will be related to the noise (see for example [143]). As an example, if the electrons are uncorrelated, as is the case for a weak tunnelling current, then the distribution is a Poisson one, which leads to the noise being given by

$$S = 2e\langle I \rangle. \tag{6.5}$$

[1] See [14, 138–141] for more in-depth discussions on these.

In this instance, the noise is proportional to the current so vanishes in equilibrium, though in general this sort of formula only holds if the charge is transferred in one direction and so usually the noise has an equilibrium and non-equilibrium part to it. The third moment of the distribution has no such limitation however and can be a better indication of non-equilibrium noise [143]. This is particularly relevant for MBL where the non-equilibrium component is of interest [27].

The third moment of current fluctuations is expected to diverge near the MBL transition when the transition is viewed as a function of temperature. Whilst it is currently unclear whether a stable MBL phase exists at finite temperatures in the thermodynamic limit, MBL physics should still be observable in experiments which have a finite size and time associated with them. Therefore, a transition occurring at T_{c}, given by Eq. (2.17), is of interest. The transition can be thought of as a cascade process because as T_{c} is approached a phonon begins to excite electrons and cause hopping. The number of electrons that hop due to the phonon diverges at the transition, restoring a phononless transport regime. Whilst there are nuances in precisely how this number of electrons diverges [27], the key thing to note is that this causes the bunching of electrons as the temperature is increased and therefore a divergence in the noise. However, as previously mentioned it is better to observe this in the third moment of the current fluctuations where the non-equilibrium contribution is clearer.

Therefore, a natural extension to this project is to explore the third moment of current fluctuations in electronic systems. In quantum dots this can be done by utilising the Keldysh formalism to calculate the noise using Eq. (6.3) and then the third moment. As well as considering previous approaches to noise, for instance the tunnelling current [143], it will also be important to consider the fine structure of tunnelling states at the low energies relevant for localisation [144] in order to accurately assess the noise in this regime. Another possible direction of future research could include exploring signatures in driven systems as the driving can in some instances counteract the thermalisation due to the phonons [145], though the work with electronic noise is more of a direct extension of the

work carried out here.

6.4 Summary

This chapter has focused on identifying the absence of thermalisation in quantum dots through the appearance of an additional peak in the differential conductance compared to the fully thermalised case. This arises due to the distribution function of electrons having a double-step form which reflects the fact that electrons coming from the left and right leads do not equilibrate and is predicted to be observable providing that the coupling to the leads is symmetric and the dot is in the classical Coulomb blockade regime. This effect also occurs in a non-interacting dot and has been observed in mesoscopic wires [137]. After this, a discussion of electronic noise as a signature of MBL was discussed as a way to extend the work presented in this thesis.

CHAPTER 7

CONCLUSION

To summarise, this work has focused on the identification of signatures of the absence of thermalisation in electronic systems. This will allow for materials to be found that could potentially be candidates for observing many-body localisation, which has so far eluded traditional solid-state setups due to the presence of phonons.

This thesis began by introducing the concept of mesoscopic physics and the associated transport regimes. It was shown how the phase coherence length being comparable to or larger than the system size is crucial in observing new behaviour such as weak localisation which gives a decreased conductivity in a weakly disordered metal. This is due to the phase coherence between electronic paths resulting in an increased return probability. In strongly disordered materials, this phase coherence manifests itself as Anderson localisation where electronic wavefunctions are localised in space leading to zero transport across a system. It was then seen how transport can be restored (and localisation destroyed) at finite temperatures due to the phonons in the system providing electrons with the energy to hop. The topic of MBL was introduced as electron-electron interactions may not be sufficient to destroy localisation in the same way as the phonons. This gives rise to a localised regime with a number of unique properties, such as breaking the eigenstate thermalisation hypothesis and avoiding thermalisation, in addition to the logarithmic growth of entanglement in time. Whilst this entanglement growth is seen as one of the defining

features of MBL, it is inaccessible in solid-state setups.

By making use of the Keldysh formalism, an analysis of the electron-phonon cooling rate was performed which showed that electron-phonon decoupling can be identified via hysteretic jumps of several orders of magnitude in the current-voltage characteristics. This arises below a critical lattice temperature due to a bistability in the electron temperature, in which a cool electron state exists as well as an overheated one, the latter of which leads to phonon-independent transport. The bistability can also be observed through the existence of a regime of inaccessible electron temperatures, corresponding to the unstable states. For the system to exhibit this observable decoupling, an Arrhenius resistance is required, as other forms of resistance result in significantly lower critical temperatures making the bistability practically inaccessible. It is important to emphasise that this bistability is simply a reflection of the decoupling and does not indicate MBL itself and further signatures must be identified.

An ideal system to study these signatures is that of quantum dots which undergo a localisation transition in Fock space, analogous to that in MBL. Interactions play a key role in quantum dots with the Coulomb blockade being a key example of this. In this regime, a large amount of energy is needed to overcome the Coulomb repulsion and add an additional electron onto the dot. It was shown how the Coulomb staircase, which has characteristically been studied in the case of full thermalisation, persists in the case of asymmetric coupling to the leads even when thermalisation on the dot is absent. This is due to the formation of an equilibrium with the strongly coupled lead. Although the absence of thermalisation is not identifiable in the context of the Coulomb staircase here, a new regime of transport was identified where the contribution of the lowest energy levels on the dot causes the practical disappearance of the staircase.

Finally, it was shown that when the leads are coupled to the dot equally, the absence of thermalisation can be identified as the distribution function on the dot changes from a Fermi function to a double-step function reflecting the fact that electrons from the left and right leads tunnel on at different energies and do not equilibrate. This has the

consequence of an additional jump in the differential conductance compared to the fully thermalised dot and should allow for an experimentally accessible signature of the absence of thermalisation. In order to further this work, signatures of the localised regime itself should be sought after with the behaviour of electronic noise providing the most appealing opportunity to identify localisation.

APPENDIX A

ANALYTIC CONTINUATION IN KELDYSH

In this section the process of analytic continuation in the Keldysh formalism will be detailed. This provides a procedure that goes from the double-time contour back to real time, which is necessary for any physical calculations. The first part of this section will look at performing this procedure for the case of a scalar potential where the added complication of index notation in interaction vertices is not required. After, the index notation will also be addressed. This is based on work presented in [43].

For the scalar, potential the first order correction to the contour-ordered Green's function, G can be expressed as

$$\delta G^{(1)}(x,x') = \int \mathrm{d}\mathbf{r_1} \int_C \mathrm{d}\tau_1 G_0(\mathbf{r},\mathbf{r_1},t,\tau_1) U(\mathbf{r_1},\tau_1) G_0(\mathbf{r_1},\mathbf{r}',\tau_1,t'), \tag{A.1}$$

with $x = (\mathbf{r}, t)$. The aim is to then express this in terms of the matrix in Eq. (3.33), which has the notation $G_{ij}(x,x')$ with $i,j = 1,2$. If x has a time argument on the upper contour, then $i = 1$ and if x' is lower contour $j = 2$ etc. The contour integral in the expression above can then be split into an integral along the upper contour and an integral over the

lower contour, resulting in[1],

$$\delta G^{(1)}_{ij}(x,x') = \int \mathrm{d}x_1 \left[(G_0)_{i1}(x,x_1)U(x_1)(G_0)_{1j}(x_1,x') - (G_0)_{i2}(x,x_1)U(x_1)(G_0)_{2j}(x_1,x')\right], \tag{A.2}$$

where $\int \mathrm{d}x_1 = \int \mathrm{d}\mathbf{r}_1 \int_{-\infty}^{\infty} \mathrm{d}t_1$. By expressing the above in matrix form, the result of Eq. (3.38) is obtained. The Keldysh rotation [43, 89] is then performed using the transformation $G \to L\sigma^{(z)}GL^\dagger$, with

$$L = \frac{1}{\sqrt{2}}\begin{pmatrix} 1 & -1 \\ 1 & 1 \end{pmatrix}, \tag{A.3}$$

such that $L^\dagger L = \mathbb{1}$ and $\sigma^{(z)}\sigma^{(z)} = \mathbb{1}$. This restores all the results for the scalar potential mentioned in the main text. The focus will now be on developing the index notation through exploration of the correction to the Green's function due to the electron-phonon (or electron-electron as they have the same diagrammatic expansion) interaction. The first order correction is shown in Fig. 3.4(b) and after splitting the contour integral into integrals over the upper and lower branch, the correction is given by

$$\begin{aligned}\delta G^{(1)}_{ij}(x,x') = i \int \mathrm{d}x_1 \mathrm{d}x_2 \Big[& G_{i1}(x,x_1)\gamma(x_1)G_{11}(x_1,x_2)D_{11}(x_1,x_2)\gamma(x_2)G_{1j}(x_2,x') \\ & - G_{i1}(x,x_1)\gamma(x_1)G_{12}(x_1,x_2)D_{12}(x_1,x_2)\gamma(x_2)G_{2j}(x_2,x') \\ & - G_{i2}(x,x_1)\gamma(x_1)G_{21}(x_1,x_2)D_{21}(x_1,x_2)\gamma(x_2)G_{1j}(x_2,x') \\ & + G_{i2}(x,x_1)\gamma(x_1)G_{22}(x_1,x_2)D_{22}(x_1,x_2)\gamma(x_2)G_{2j}(x_2,x')\Big],\end{aligned} \tag{A.4}$$

where the γ's represent the vertices and the G's and D's under the integral are G_0 and D_0 but the subscript has been dropped for clarity. This can be expressed fully in terms

[1] An alternative to this is to use Langreth's theorem which involves the deformation of the contour, details of which can be found in [85].

of index notation (where repeated indices are summed over) to give

$$\delta G^{(1)}_{ij}(x,x') = i\int \mathrm{d}x_1\mathrm{d}x_2 G_{im}(x,x_1)\gamma(x_1)\sigma^{(z)}_{mk}G_{mm'}(x_1,x_2) \\ \times D_{kk'}(x_1,x_2)\gamma(x_2)\sigma^{(z)}_{m'k'}G_{m'j}(x_2,x'). \quad \text{(A.5)}$$

After condensing the index notation, making use of the convolution symbol and considering the case that each vertex has a factor λ associated with it, Eq. (3.41) is recovered, that is

$$\delta G^{(1)}_{ij} = (G_0)_{im}\circ\Sigma_{mm'}\circ(G_0)_{m'j}, \quad \Sigma_{mm'} = i\gamma^k_{mn}(G_0)_{nn'}(D_0)_{kk'}\gamma^{k'}_{n'm'}, \quad \text{(A.6)}$$

with $\gamma^k_{mn} = \lambda\delta_{mn}\sigma^{(z)}_{nk}$. The remaining task is then to perform the Keldysh rotation. In order to preserve the form of Dyson's equation, although the Green's functions transform as $G \to L\sigma^{(z)}GL^\dagger$, the self-energy transforms as $\Sigma \to L\Sigma\sigma^{(z)}L^\dagger$. After various insertions of the identity via $L^\dagger L = \mathbb{1}$ and $\sigma^{(z)}\sigma^{(z)} = \mathbb{1}$, the 'rotated' self-energy becomes

$$\tilde{\Sigma}_{mm'} = i\tilde{\gamma}^k_{mn}(\tilde{G}_0)_{nn'}(\tilde{D}_0)_{kk'}\bar{\gamma}^{k'}_{n'm'}, \quad \text{(A.7)}$$

where the emission, $\tilde{\gamma}^k_{mn}$, and absorption, $\bar{\gamma}^{k'}_{n'm'}$, vertices transform as

$$\tilde{\gamma}^k_{mn} = L_{mi}\gamma^l_{ij}\sigma^{(z)}_{jf}\sigma^{(z)}_{lg}L^\dagger_{fn}L^\dagger_{gk}, \quad \text{(A.8)}$$

$$\bar{\gamma}^{k'}_{n'm'} = L_{n'i}L_{k'j}\gamma^j_{il}\sigma^{(z)}_{lf}L^\dagger_{fm'}. \quad \text{(A.9)}$$

Careful calculation of the vertices then gives the results in the main text for the transformed indices,

$$\tilde{\gamma}^1_{mn} = \frac{\lambda}{\sqrt{2}}\delta_{mn}, \qquad \tilde{\gamma}^2_{mn} = \frac{\lambda}{\sqrt{2}}\sigma^{(x)}_{mn}, \quad \text{(A.10)}$$

$$\bar{\gamma}^1_{mn} = \frac{\lambda}{\sqrt{2}}\sigma^{(x)}_{mn}, \qquad \bar{\gamma}^2_{mn} = \frac{\lambda}{\sqrt{2}}\delta_{mn}. \quad \text{(A.11)}$$

APPENDIX B

DERIVATION OF THE QUANTUM KINETIC EQUATION

Here, the quantum kinetic equation (QKE) will be derived and the collision integral will be found by considering the electron-phonon interaction. It follows a number of derivations presented in [43, 82–84, 102].

The starting point is the left and right Dyson equations

$$G \circ \left(G_0^{-1} - \Sigma\right) = \mathbb{1}, \tag{B.1}$$

$$\left(G_0^{-1} - \Sigma\right) \circ G = \mathbb{1}, \tag{B.2}$$

which upon subtraction can be written as

$$[G_0^{-1} \circ ; G] = [\Sigma \circ ; G]. \tag{B.3}$$

The matrix form involving G^R, G^A, G^K can then be utilised and taking the Keldysh component gives

$$(G_0^R)^{-1} \circ G^K - G^K \circ (G_0^A)^{-1} = \Sigma^R \circ G^K + \Sigma^K \circ G^A - G^R \circ \Sigma^K - G^K \circ \Sigma^A \tag{B.4}$$

where terms involving $(G_0^K)^{-1} \sim i\delta, \delta \ll 1$ have been ignored and all Green's functions and self-energies are functions of x, x' with $x = (\mathbf{r}, t)$. Both the inverse of the retarded and advanced Green's functions can be expressed as $G_0^{-1} = (i\partial_t - H(\mathbf{r}))\delta(x - x')$, so that the Keldysh component can then be written as

$$[G_0^{-1} \circ G^K] = \Sigma^R \circ G^K + \Sigma^K \circ G^A - G^R \circ \Sigma^K - G^K \circ \Sigma^A. \tag{B.5}$$

The next step is to perform a Wigner transform, which is a transformation to mixed coordinates. If the form of the kinetic equation desired is the same as the Boltzmann equation, Eq. (4.11), then both a spatial and temporal Wigner transform should be taken [43, 82–84]. However in this thesis the desired form is that presented in Eq. (4.16) and derived in [102]. Therefore, only a temporal Wigner transform is required. This takes a function $f(t_1, t_2) \to f(\varepsilon, t)$ by introducing the mixed coordinates $t = \frac{1}{2}(t_1 + t_2)$ and $t' = t_1 - t_2$. The temporal Wigner transform is then defined by

$$f(\varepsilon, t) = \int \mathrm{d}t' \mathrm{e}^{i\varepsilon t'} f\left(t + \frac{t'}{2}, t - \frac{t'}{2}\right), \tag{B.6}$$

which leads to a couple of useful properties and for functions slowly varying with t these become [43, 82, 83]

$$f(t_1, t_2) \circ g(t_1, t_2) \to f(\varepsilon, t) g(\varepsilon, t), \tag{B.7}$$

$$[f(t_1, t_2) \circ g(t_1, t_2)] \to -i(\partial_t f \partial_\varepsilon g - \partial_\varepsilon f \partial_t g), \tag{B.8}$$

$$f(t_1, t_2) g(t_1, t_2) \to \int \frac{\mathrm{d}\omega}{2\pi} f(\varepsilon - \omega, t) g(\omega, t). \tag{B.9}$$

These properties can be used to perform a temporal Wigner transform on Eq. (B.5) to give

$$i\partial_\varepsilon G_0^{-1} \partial_t G^K = \Delta\Sigma G^K - \Sigma^K \Delta G, \tag{B.10}$$

where $\Delta G = G^R - G^A$, $\Delta\Sigma = \Sigma^R - \Sigma^K$ and all functions now depend on $\mathbf{r}, \mathbf{r}', \varepsilon$ and t.

Additionally, the term involving $\partial_t G_0^{-1}$ has been ignored as a slowly varying potential is assumed [84]. The left-hand side can then be evaluated as the derivative of G_0^{-1} gives $\delta(\mathbf{r}-\mathbf{r}')$ and the quasi-equilibrium form of G^K can be used, $G^K = f_\varepsilon(t)(G^R - G^A)$. Then integrating both sides of Eq. (B.10) with respect to the spatial coordinates the form of the kinetic equation in Eq. (4.16) [102] is found

$$\partial_t f_\varepsilon(t) = I[f_\varepsilon(t)] = \frac{1}{2\pi\nu\mathcal{V}} \operatorname{Tr}\big(\Delta\Sigma G^K - \Sigma^K \Delta G\big), \tag{B.11}$$

where the trace represents integration over the spatial variables.

The next task is to evaluate the self-energy to give a more useful form of the collision integral. This involves a consideration of the electron-phonon interaction which is diagrammatically shown in Fig. 4.3. In index notation (where repeated indices are summed over) this diagram can be expressed as

$$\begin{aligned}\Sigma_{ij} &= i\tilde{\gamma}^k_{ij'} G_{j'i'} D_{kk'} \bar{\gamma}^{k'}_{i'j} \\ &= \frac{i}{2}\left(G_{ii'}\sigma^{(x)}_{i'j} D^R + G_{ij} D^K + \sigma^{(x)}_{ij'} G_{j'j} D^A\right).\end{aligned} \tag{B.12}$$

Then the components of the self-energy matrix can be evaluated to give

$$\Sigma^R = \frac{i}{2}\left(G^K D^R + G^R D^K\right), \tag{B.13}$$

$$\Sigma^A = \frac{i}{2}\left(G^K D^A + G^A D^K\right), \tag{B.14}$$

$$\begin{aligned}\Sigma^K &= \frac{i}{2}\left(G^R D^R + G^A D^A + G^K D^K\right) \\ &= \frac{i}{2}\left(G^K D^K + \Delta G \Delta D\right),\end{aligned} \tag{B.15}$$

where in the final line, terms such as $G^R D^A = 0$ have been included. The above expressions for the self-energy are still in terms of real coordinates and don't include the electron-phonon vertices yet. After performing the Wigner transform and including the

vertices the collision integral can be written as

$$I[f] = \frac{i}{4\pi\nu\mathcal{V}} \int \mathrm{d}\mathbf{r}\mathrm{d}\mathbf{r}' \int \frac{\mathrm{d}\omega}{2\pi} \Big[G^K(\mathbf{r},\mathbf{r}',\varepsilon)\hat{g}_\alpha(\mathbf{r}')\Delta G(\mathbf{r}',\mathbf{r},\varepsilon-\omega)D^K(\mathbf{r}',\mathbf{r},\omega)\hat{g}_\beta(\mathbf{r}) \\ + G^K(\mathbf{r},\mathbf{r}',\varepsilon)\hat{g}_\alpha(\mathbf{r}')G^K(\mathbf{r}',\mathbf{r},\varepsilon-\omega)\Delta D(\mathbf{r}',\mathbf{r},\omega)\hat{g}_\beta(\mathbf{r}) \\ - \Delta G(\mathbf{r},\mathbf{r}',\varepsilon)\hat{g}_\alpha(\mathbf{r}')G^K(\mathbf{r}',\mathbf{r},\varepsilon-\omega)D^K(\mathbf{r}',\mathbf{r},\omega)\hat{g}_\beta(\mathbf{r}) \\ - \Delta G(\mathbf{r},\mathbf{r}',\varepsilon)\hat{g}_\alpha(\mathbf{r}')\Delta G(\mathbf{r}',\mathbf{r},\varepsilon-\omega)\Delta D(\mathbf{r}',\mathbf{r},\omega)\hat{g}_\beta(\mathbf{r}) \Big], \tag{B.16}$$

where the explicit time dependence has been dropped. The final step is to insert the quasi-equilibrium forms of the Keldysh components, $G^K(\varepsilon) = f_\varepsilon \Delta G(\varepsilon)$ and $D^K(\omega) = N_\omega \Delta D(\omega)$, and replace the volume with the area, $\mathcal{A}$, to give the final result [23, 102]

$$I[f] = \frac{i}{4\pi\nu\mathcal{A}} \Big\langle \int_{-\infty}^{\infty} \frac{\mathrm{d}\omega}{2\pi} \int \mathrm{d}\mathbf{r}\mathrm{d}\mathbf{r}' \Delta G(\mathbf{r},\mathbf{r}',\varepsilon)\hat{g}_\alpha(\mathbf{r}')\Delta G(\mathbf{r}',\mathbf{r},\varepsilon-\omega) \\ \times \Delta D_{\alpha\beta}(\mathbf{r}'-\mathbf{r},\omega)\hat{g}_\beta(\mathbf{r})[(f_\varepsilon - f_{\varepsilon-\omega})N_\omega + f_\varepsilon f_{\varepsilon-\omega} - 1] \Big\rangle. \tag{B.17}$$

which is that in Eq. (4.17).

APPENDIX C

CALCULATION OF THE DIAGRAMS FOR THE ELECTRON-PHONON COOLING RATE

In this section, additional details of the calculation of the electron-phonon cooling rate included in *Electron-Phonon Decoupling in Two Dimensions* [23] will be presented. The starting point is the quantum kinetic equation, Eq. (4.9)

$$\partial_t f_\varepsilon(t) = I[f], \tag{C.1}$$

with the collision integral [23, 102]

$$I[f] = \frac{i}{4\pi\nu\mathcal{A}}\Big\langle \int_{-\infty}^{\infty} \frac{\mathrm{d}\omega}{2\pi} \int \mathrm{d}\mathbf{r}\mathrm{d}\mathbf{r}' \Delta G(\mathbf{r},\mathbf{r}',\varepsilon)\hat{g}_\alpha(\mathbf{r}')\Delta G(\mathbf{r}',\mathbf{r},\varepsilon-\omega) \tag{C.2}$$
$$\times \Delta D_{\alpha\beta}(\mathbf{r}'-\mathbf{r},\omega)\hat{g}_\beta(\mathbf{r})[(f_\varepsilon - f_{\varepsilon-\omega})N_\omega + f_\varepsilon f_{\varepsilon-\omega} - 1]\Big\rangle.$$

The Fourier transform of the phonon propagator,

$$\Delta D_{\alpha\beta}(\mathbf{r}'-\mathbf{r},\omega)=\frac{1}{\mathcal{A}}\sum_{\mathbf{q}}\mathrm{e}^{i\mathbf{q}\cdot(\mathbf{r}'-\mathbf{r})}\Delta D_{\alpha\beta}(\mathbf{q},\omega), \tag{C.3}$$

can be used and after recalling that the phonons aren't affected by the impurities, the collision integral is given by

$$I[f]=\frac{i}{4\pi\nu\mathcal{A}}\int_{-\infty}^{\infty}\frac{\mathrm{d}\omega}{2\pi}\sum_{\mathbf{q}}F_{\alpha\beta}(q)\Delta D_{\alpha\beta}(\mathbf{q},\omega)[(f_{\varepsilon}-f_{\varepsilon-\omega})N_{\omega}+f_{\varepsilon}f_{\varepsilon-\omega}-1], \tag{C.4}$$

with

$$F_{\alpha\beta}(q)=\frac{1}{\mathcal{A}}\int\mathrm{d}\mathbf{r}\mathrm{d}\mathbf{r}'\mathrm{e}^{-i\mathbf{q}\cdot\mathbf{r}}\Delta G(\mathbf{r},\mathbf{r}',\varepsilon)\hat{g}_{\alpha}(\mathbf{r}')\mathrm{e}^{i\mathbf{q}\cdot\mathbf{r}'}\Delta G(\mathbf{r}',\mathbf{r},\varepsilon-\omega)\hat{g}_{\beta}(\mathbf{r}). \tag{C.5}$$

The phonon propagator is a standard result and the derivation will not be provided here, with the result being given by [40, 86, 102]

$$\Delta D_{\alpha\beta}(\mathbf{q},\omega)=\sum_{j}\Delta D^{(j)}_{\alpha\beta}(\mathbf{q},\omega)=-\sum_{j}\frac{i\pi\eta^{(j)}_{\alpha\beta}}{\rho_{2d}\omega_{j}(q)}\left[\delta\left(\omega-\omega_{j}(q)\right)-\delta\left(\omega+\omega_{j}(q)\right)\right] \tag{C.6}$$

with $\eta^{(l)}_{\alpha\beta}=q_{\alpha}q_{\beta}/q^{2}$, $\eta^{(t)}_{\alpha\beta}=\delta_{\alpha\beta}-q_{\alpha}q_{\beta}/q^{2}$ for longitudinal and transverse phonons respectively, and the phonon dispersion is given by $\omega_{j}(q)=u_{j}q$ for $q<q_{0}$ and zero otherwise, where q_{0} is the cutoff Debye momentum. The density of the material forming the 2d film is denoted by ρ_{2d}. By substituting the result in Eq. (C.6) into Eq (C.4) and manipulating the δ-functions allows the collision integrals to be written as

$$I[f]=-2\int\mathrm{d}\omega K(\omega)[(f_{\varepsilon}-f_{\varepsilon-\omega})N_{\omega}+f_{\varepsilon}f_{\varepsilon-\omega}-1], \tag{C.7}$$

with

$$K(\omega)=-\frac{\mathrm{sgn}(\omega)}{2}\frac{1}{(2\pi)^{2}}\sum_{j}\frac{\beta_{j}}{2\nu^{2}\varepsilon_{\mathrm{F}}^{2}}F_{\alpha\beta}(q)\eta^{(j)}_{\alpha\beta}\Big|_{q=\frac{|\omega|}{u_{j}}} \tag{C.8}$$

and $\beta_j = \dfrac{\nu\varepsilon_{\mathrm{F}}^2}{2\rho_{2d}u_j^2}$. The remaining task is to calculate $F_{\alpha\beta}(q)$ and then evaluate $K(\omega)$. For the case of transverse phonons, this involves consideration of the diagrams in Fig. 4 of *Electron-Phonon Decoupling in Two Dimensions* [23]. The first of these diagrams can be expressed as

$$F^{(1)}_{\alpha\beta}(q) = \frac{1}{\mathcal{A}^3}\sum_{\mathbf{p},\mathbf{k_1},\mathbf{k_2}} \Delta G(\mathbf{p},\varepsilon)(-iU(\mathbf{k_1})\mathbf{k}_\mathbf{1}^\alpha)\Delta G(\mathbf{p}-\mathbf{k_1}-\mathbf{q},\varepsilon-\omega)(-iU(\mathbf{k_2})\mathbf{k}_\mathbf{2}^\beta), \quad \text{(C.9)}$$

which after performing disorder averaging and shifting variables becomes

$$F^{(1)}_{\alpha\beta}(q) = \frac{1}{2\pi\nu\tau}\frac{1}{\mathcal{A}^2}\sum_{\mathbf{p},\mathbf{p}'} \Delta G(\mathbf{p},\varepsilon)\Delta G(\mathbf{p}'-\mathbf{q},\varepsilon-\omega)(\mathbf{p}-\mathbf{p}')^\alpha(\mathbf{p}-\mathbf{p}')^\beta. \quad \text{(C.10)}$$

The following results for the integrals can then be used

$$\frac{1}{\mathcal{A}}\sum_{\mathbf{p}} \Delta G(\mathbf{p},\varepsilon) = -2\pi i\nu, \quad \text{(C.11)}$$

$$\frac{1}{\mathcal{A}}\sum_{\mathbf{p}} \Delta G(\mathbf{p},\varepsilon)\mathbf{p} = 0, \quad \text{(C.12)}$$

$$\frac{1}{\mathcal{A}}\sum_{\mathbf{p}} \Delta G(\mathbf{p},\varepsilon)\mathbf{p}^\alpha\mathbf{p}^\beta = -2\pi i\nu p_{\mathrm{F}}^2\frac{\delta_{\alpha\beta}}{2}, \quad \text{(C.13)}$$

to give for the transverse phonons

$$F^{(1)}_{\alpha\beta}(q)\left(\delta_{\alpha\beta} - \frac{q_\alpha q_\beta}{q^2}\right) = -\frac{2\pi\nu p_{\mathrm{F}}^2}{\tau}. \quad \text{(C.14)}$$

Following this, the second diagram with the modified vertex must be considered. Since sums of the form

$$\frac{1}{\mathcal{A}}\sum_{\mathbf{p}} G^R(\mathbf{p},\varepsilon)G^R(\mathbf{p}-\mathbf{q},\varepsilon-\omega) = 0, \quad \text{(C.15)}$$

as well as the corresponding one involving G^A, then the vertex must have different Green's functions on the incoming and outgoing vertices. Through simple calculation, it is found that if G^R enters the vertex and G^A leaves then the vertex is $\Gamma_1 = \mathbf{p}/\tau$ and if G^A enters

and G^R leaves then the vertex has a form $\Gamma_2 = -\mathbf{p}/\tau$. Then the diagram can be expressed (after some careful algebra) as

$$F^{(2)}_{\alpha\beta}(q)\left(\delta_{\alpha\beta} - \frac{q_\alpha q_\beta}{q^2}\right) = \frac{p_{\mathrm{F}}^2}{\tau^2}\frac{1}{\mathcal{A}}\sum_{\mathbf{p}} G^R(\mathbf{p},\varepsilon)G^A(\mathbf{p}-\mathbf{q},\varepsilon-\omega)(1-\cos^2\theta) + \text{c.c.}. \quad \text{(C.16)}$$

The sum can be converted to an integral via

$$\frac{1}{\mathcal{V}}\sum_{\mathbf{p}} = \int \frac{pdpd\theta}{(2\pi)^2} \approx \frac{\nu}{2\pi}\int_{-\infty}^{\infty} d\xi \int_0^{2\pi} d\theta, \quad \text{(C.17)}$$

after which the integrals can be performed to give in the dirty limit ($ql \ll 1$)

$$F^{(2)}_{\alpha\beta}(q)\left(\delta_{\alpha\beta} - \frac{q_\alpha q_\beta}{q^2}\right) = -\frac{2\pi\nu p_{\mathrm{F}}^2}{\tau}\left(-1 + \frac{(ql)^2}{4}\right). \quad \text{(C.18)}$$

The two diagrams can then be combined to give the complete result for transverse phonons

$$F^{(2)}_{\alpha\beta}(q)\left(\delta_{\alpha\beta} - \frac{q_\alpha q_\beta}{q^2}\right) = -\frac{2\pi\nu p_{\mathrm{F}}^2}{\tau}\frac{(ql)^2}{4}. \quad \text{(C.19)}$$

Then, the substitution of this result into Eq. (C.8), gives the expression for $K(\omega)$,

$$K(\omega) = \frac{\beta_t \,\mathrm{sgn}(\omega)}{8k_{\mathrm{F}}l}(ql)^2. \quad \text{(C.20)}$$

that appears in Eq. (16) in *Electron-Phonon Decoupling in Two Dimensions* [23]. From this point the calculation proceeds as described in the manuscript to calculate the cooling rate. For longitudinal phonons all diagrams in Fig. 4.4 contribute and can be calculated in a similar manner to those shown here, remembering to include the diffuson, described by Eq. (3.60), where necessary.

APPENDIX D

DERIVATION OF THE CURRENT FORMULA FOR TRANSPORT THROUGH A QUANTUM DOT

In this section, the current formula shown in Eq. (5.13) will be derived. This follows the work presented in [85, 136, 146]. The current going from the lead α to the dot is given by

$$I_\alpha = -e\langle \dot{N}_\alpha \rangle = -ie\langle [H, N_\alpha] \rangle, \tag{D.1}$$

where the number operator for the leads is given by $N_\alpha = \sum_k c^\dagger_{k,\alpha} c_{k,\alpha}$. The Hamiltonian of the system, written in terms of the creation and annihilation operators for the dot $(d^\dagger, d)$ and leads, $(c^\dagger, c)$, is given by $H = H_\mathrm{d} + H_\ell + H_\mathrm{T}$ with,

$$H_\mathrm{d} = \sum_n \varepsilon_n d^\dagger_n d_n + \frac{1}{2} E_\mathrm{c} \left(\hat{N} - N_\mathrm{g} \right)^2, \tag{D.2}$$

$$H_\ell = \sum_{k,\alpha} \left(\varepsilon_k - \mu_\alpha \right) c^\dagger_{k,\alpha} c_{k,\alpha}, \tag{D.3}$$

$$H_\mathrm{T} = \sum_\alpha H^{(\alpha)}_\mathrm{T} = \sum_{\alpha,k,n} \left(t_\alpha c^\dagger_{k,\alpha} d_n + \mathrm{h.c.} \right). \tag{D.4}$$

Only the latter of these doesn't commute with the number operator, meaning that

$$I_\alpha = -ie\langle[H_{\mathrm{T}}^{(\alpha)}, N_\alpha]\rangle. \tag{D.5}$$

After the substitution of the relevant Hamiltonian into this expression, the use of fermionic anticommutation relations gives,

$$I_\alpha = ie\sum_{k,n} t_\alpha\langle c_{k,\alpha}^\dagger d_n\rangle - t_\alpha^*\langle d_n^\dagger c_{k,\alpha}\rangle = 2e\mathrm{Re}\left[t_\alpha\sum_{k,n} G_{\alpha,k,n}^<(t,t)\right], \tag{D.6}$$

where $G_{\alpha,k,n}^<(t,t') = i\langle c_{k,\alpha}^\dagger(t')d_n(t)\rangle$.

In order to make further progress, $G_{\alpha,k,n}^<(t,t')$ needs to be calculated. Consider the contour-ordered Green's function

$$G_{\alpha,k,n}(t,t') = -i\langle T_C d_n(t)c_{k,\alpha}^\dagger(t')\rangle = -i\Big\langle T_C\left(S\tilde{d}_n(t)\tilde{c}_{k,\alpha}^\dagger(t')\right)\Big\rangle, \tag{D.7}$$

where in the last line, the interaction representation (denoted by the tilde's) has been used by introducing the S-matrix,

$$\begin{aligned} S &= T_C \mathrm{e}^{-i\int_C \mathrm{d}t_1 \tilde{H}_{\mathrm{T}}(t_1)} \\ &= T_C\sum_{m=0}^{\infty}\frac{(-i)^m}{m!}\left[\int_C \mathrm{d}t_1\sum_{\alpha',k',m'}\left(t_{\alpha'}\tilde{c}_{k',\alpha'}^\dagger(t_1)\tilde{d}_{m'}(t_1) + t_{\alpha'}^*\tilde{d}_{m'}^\dagger(t_1)\tilde{c}_{k',\alpha'}(t_1)\right)\right]^m. \end{aligned} \tag{D.8}$$

Upon substitution into the Green's function, the $m = 0$ term doesn't contribute as it contains an average $\langle T_C\tilde{d}_n(t)\tilde{c}_{\alpha,k}^\dagger(t')\rangle = 0$. Therefore the Green's function can be expressed as

$$\begin{aligned} G_{\alpha,k,n}(t,t') = -i\Bigg\langle T_C\sum_{m=0}^{\infty}\frac{(-i)^{m+1}}{(m+1)!}\Bigg[\int_C \mathrm{d}t_1\sum_{\alpha',k',m'}\Big(t_{\alpha'}\tilde{c}_{k',\alpha'}^\dagger(t_1)\tilde{d}_{m'}(t_1) \\ + t_{\alpha'}^*\tilde{d}_{m'}^\dagger(t_1)\tilde{c}_{k',\alpha'}(t_1)\Big)\Bigg]^{m+1}\tilde{d}_n(t)\tilde{c}_{k,\alpha}^\dagger(t')\Bigg\rangle. \end{aligned} \tag{D.9}$$

To have a non-zero average upon using Wick's theorem there needs to be a matching number of creation and annihilation operators of each variety (i.e. for the dot and the leads separately). One factor of the term in the square brackets is sufficient to provide this and as there are $m+1$ ways of taking this factor, the Green's function becomes

$$G_{\alpha,k,n}(t,t') = -i\int_C \mathrm{d}t_1 \sum_{\alpha',k',m'} t^*_{\alpha'}\Big\langle T_C(-iS)\tilde{d}^\dagger_{m'}(t_1)\tilde{c}_{k',\alpha'}(t_1)\tilde{d}_n(t)\tilde{c}^\dagger_{k,\alpha}(t')\Big\rangle. \tag{D.10}$$

All of the 'difficult' physics encapsulated by the S-matrix can at this point be put into the Green's function for the dot, whilst keeping the Green's functions for the leads simple. To do this the Green's functions for the dot and lead can be defined as

$$G_{n,m} = -i\langle T_C d_n(t)d^\dagger_m(t')\rangle = -i\langle T_C S\tilde{d}_n(t)\tilde{d}^\dagger_m(t')\rangle, \tag{D.11}$$

$$g_{k,\alpha} = -i\langle T_C \tilde{c}_{k,\alpha}(t)\tilde{c}^\dagger_{k,\alpha}(t')\rangle. \tag{D.12}$$

Then, performing Wick's theorem on Eq. (D.10) leads to

$$G_{\alpha,k,n}(t,t') = \sum_m \int_C \mathrm{d}t_1 t^*_\alpha G_{n,m}(t,t_1)g_{k,\alpha}(t_1,t') \tag{D.13}$$

following which analytic continuation can be performed to return to real time and to give the Green's function contained in the expression for the current (Eq. (D.6)),

$$G^<_{\alpha,k,n}(t,t') = \sum_m \int_{-\infty}^{\infty} \mathrm{d}t_1 t^*_\alpha \left[G^R_{n,m}(t,t_1)g^<_{k,\alpha}(t_1,t') + G^<_{n,m}(t,t_1)g^A_{k,\alpha}(t_1,t')\right]. \tag{D.14}$$

The expression for the current in Eq. (D.6) contains the Green's function evaluated at equal times and therefore the current, after Fourier transforming, is given by

$$I_\alpha = 2e|t_\alpha|^2 \int \frac{\mathrm{d}\varepsilon}{2\pi}\mathrm{Re}\left[\sum_{k,m,n}\left(G^R_{n,m}(\varepsilon)g^<_{k,\alpha}(\varepsilon) + G^<_{n,m}(\varepsilon)g^A_{k,\alpha}(\varepsilon)\right)\right]. \tag{D.15}$$

If the density of states is constant on a scale of the charging energy, E_c, then it can be

assumed that it is a constant in this work and therefore the sum over momenta can be expressed as an integral, $\sum_k = \nu_\alpha \int \mathrm{d}\xi_{k,\alpha}$. Then, defining $\Gamma_\alpha = 2\pi\nu_\alpha |t_\alpha|^2$, the current becomes

$$I_\alpha = 2e\Gamma_\alpha \int \frac{\mathrm{d}\varepsilon}{2\pi}\frac{\mathrm{d}\xi_{k,\alpha}}{2\pi}\mathrm{Re}\left[\sum_{m,n}\left(G^R_{n,m}(\varepsilon)g^<_{k,\alpha}(\varepsilon) + G^<_{n,m}(\varepsilon)g^A_{k,\alpha}(\varepsilon)\right)\right]. \tag{D.16}$$

To proceed further expressions for the Green's functions of the leads can be inserted,

$$g^<_{k,\alpha}(\varepsilon) = 2\pi i f_\alpha(\xi_{k,\alpha})\delta(\varepsilon - \xi_{k,\alpha}), \tag{D.17}$$

$$g^A_{k,\alpha}(\varepsilon) = \frac{1}{\varepsilon - \xi_{k,\alpha} - i\delta} = P\left(\frac{1}{\varepsilon - \xi_{k,\alpha}}\right) + i\pi\delta(\varepsilon - \xi_{k,\alpha}), \tag{D.18}$$

where in the last equality the Sokhotski–Plemelj formula has been used and P represents the principal value. In addition to these, it can be noted that $G^<_{n,m}(\varepsilon)$ is imaginary as can be seen by looking at the quasi-equilibrium approximation, $G^<(\varepsilon) = if(\varepsilon)A(\varepsilon)$, where the spectral function, $A(\varepsilon)$ is real. Using all this information, a few manipulations can be performed to show that [85, 136]

$$I_\alpha = ie\Gamma_\alpha \int \frac{\mathrm{d}\varepsilon}{2\pi}\,\mathrm{Tr}\left[G^<(\varepsilon) + f_\alpha(\varepsilon)\left(G^R(\varepsilon) - G^A(\varepsilon)\right)\right], \tag{D.19}$$

where the trace can be ignored for resonant level coupling, that is $\Gamma \ll \Delta$, as transport involves a single level so the Green's functions become scalar functions. To get the above expression into the form of Eq. (5.13), the weak coupling to the leads allows for the use of the ansatz [25, 26],

$$G^<(\varepsilon) = 2\pi i \sum_{N,n} p_N F_N(\varepsilon_n)\delta(\varepsilon - \varepsilon_n - \Omega_{N-1}), \tag{D.20}$$

$$G^>(\varepsilon) = -2\pi i \sum_{N,n} p_N (1 - F_N(\varepsilon_n))\delta(\varepsilon - \varepsilon_n - \Omega_N), \tag{D.21}$$

and along with the identity $G^R - G^A = G^> - G^<$, the current going from the dot to the

lead (which is a minus sign different from the previous expressions) is given by,

$$I_\alpha = e\Gamma_\alpha \sum_N p_N \sum_n \Big(F_N(\varepsilon_n)\,[1 - f(\varepsilon_n - \mu_\alpha + \Omega_{N-1})] - [1 - F_N(\varepsilon_n)]\, f(\varepsilon_n - \mu_\alpha + \Omega_N) \Big). \tag{D.22}$$

This is the result of Eq. (5.13).

BIBLIOGRAPHY

[1] H. L. Stormer, D. C. Tsui, and A. C. Gossard. The fractional quantum Hall effect. *Rev. Mod. Phys.*, 71:S298–S305, 1999.

[2] H. L. Stormer. Nobel Lecture: The fractional quantum Hall effect. *Rev. Mod. Phys.*, 71:875–889, 1999.

[3] P. A. Lee and A. D. Stone. Universal Conductance Fluctuations in Metals. *Phys. Rev. Lett.*, 55:1622–1625, 1985.

[4] B. L. Altshuler. Fluctuations in the extrinsic conductivity of disordered conductors. *Pis'ma Zh. Eksp. Teor. Fiz.*, 41(12):530, 1985. [*JETP Lett.*, 41(12):648, 1985].

[5] P. A. Lee, A. Douglas Stone, and H. Fukuyama. Universal conductance fluctuations in metals: Effects of finite temperature, interactions, and magnetic field. *Phys. Rev. B*, 35:1039–1070, 1987.

[6] B. L. Altshuler and A. G. Aronov. Zero bias anomaly in tunnel resistance and electron-electron interaction. *Solid State Communications*, 30(3):115–117, 1979.

[7] A. Kamenev and Y. Gefen. Zero-bias anomaly in finite-size systems. *Phys. Rev. B*, 54:5428–5437, 1996.

[8] I. L. Aleiner, P. W. Brouwer, and L. I. Glazman. Quantum effects in Coulomb blockade. *Phys. Rep.*, 358(5):309–440, 2002.

[9] D. V. Averin and K. K. Likharev. A correlated transfer of single electrons and Cooper pairs in systems of small tunnel junctions. In B.L. Altshuler, P.A. Lee, and R.A. Webb, editors, *Mesoscopic Phenomena in Solids*, volume 30 of *Modern Problems in Condensed Matter Sciences*, pages 173–271. Elsevier, Amsterdam, 1991.

[10] M. H. Devoret H. Grabert. *Single Charge Tunneling: Coulomb Blockade Phenomena In Nanostructures*. NATO Science Series B. Springer, New York, 2013.

[11] A. Lagendijk, B. van Tiggelen, and D. S. Wiersma. Fifty years of Anderson localization. *Physics Today*, 62(8):24–29, 2009.

[12] B. Kramer and A. MacKinnon. Localization: theory and experiment. *Reports on Progress in Physics*, 56(12):1469, 1993.

[13] E. Abrahams, editor. *50 Years Of Anderson Localization*. World Scientific Publishing Company, Singapore, 2010.

[14] Y. Imry. *Introduction to Mesoscopic Physics*. Mesoscopic physics and nanotechnology. Oxford University Press, Oxford, 2nd edition, 2002.

[15] R. Nandkishore and D. A. Huse. Many-Body Localization and Thermalization in Quantum Statistical Mechanics. *Annual Review of Condensed Matter Physics*, 6(1):15–38, 2015.

[16] D. A. Abanin, E. Altman, I. Bloch, and M. Serbyn. Colloquium: Many-body localization, thermalization, and entanglement. *Rev. Mod. Phys.*, 91:021001, 2019.

[17] D. A. Abanin and Z. Papić. Recent progress in many-body localization. *Annalen der Physik*, 529(7):1700169, 2017.

[18] S. Datta. *Electronic Transport in Mesoscopic Systems*. Cambridge Studies in Semiconductor Physics and Microelectronic Engineering. Cambridge University Press, Cambridge, 1995.

[19] J. H. Davies. *The Physics of Low-dimensional Semiconductors: An Introduction*. Cambridge University Press, Cambridge, 1997.

[20] D.M. Basko, I.L. Aleiner, and B.L. Altshuler. Metal–insulator transition in a weakly interacting many-electron system with localized single-particle states. *Annals of Physics*, 321(5):1126–1205, 2006.

[21] F. Alet and N. Laflorencie. Many-body localization: An introduction and selected topics. *Comptes Rendus Physique*, 19(6):498–525, 2018.

[22] I. V. Gornyi, A. D. Mirlin, and D. G. Polyakov. Interacting Electrons in Disordered Wires: Anderson Localization and Low-T Transport. *Phys. Rev. Lett.*, 95:206603, 2005.

[23] G. McArdle and I. V. Lerner. Electron-phonon decoupling in two dimensions. *Scientific Reports*, 11(1):24293, 2021.

[24] B. L. Altshuler, Y. Gefen, A. Kamenev, and L. S. Levitov. Quasiparticle lifetime in a finite system: a nonperturbative approach. *Phys. Rev. Lett.*, 78:2803–2806, 1997.

[25] G McArdle, R Davies, I V Lerner, and I V Yurkevich. Coulomb staircase in an asymmetrically coupled quantum dot. *Journal of Physics: Condensed Matter*, 35(47):475302, aug 2023.

[26] G. McArdle, R. Davies, I. V. Lerner, and I. V. Yurkevich. Coulomb blockade in a non-thermalized quantum dot. 2023. arXiv:2306.07122 [cond-mat.mes-hall].

[27] D. M. Basko, I. L. Aleiner, and B. L. Altshuler. Possible experimental manifestations of the many-body localization. *Phys. Rev. B*, 76:052203, 2007.

[28] A. A. Abrikosov. *Fundamentals of the Theory of Metals*. Elsevier Science Publishers, Amsterdam, The Netherlands, 1988.

[29] C. W. J. Beenakker and H. van Houten. Quantum Transport in Semiconductor Nanostructures. In Henry Ehrenreich and David Turnbull, editors, *Semiconductor Heterostructures and Nanostructures*, volume 44 of *Solid State Physics*, pages 1–228. Academic Press, 1991.

[30] J. J. Lin and J. P. Bird. Recent experimental studies of electron dephasing in metal and semiconductor mesoscopic structures. *Journal of Physics: Condensed Matter*, 14(18):R501, 2002.

[31] T. Ihn. *Semiconductor Nanostructures: Quantum states and electronic transport*. Oxford University Press, Oxford, 2009.

[32] A. Stern, Y. Aharonov, and Y. Imry. Phase uncertainty and loss of interference: A general picture. *Phys. Rev. A*, 41:3436–3448, 1990.

[33] B. L. Altshuler, A. G. Aronov, and D. E. Khmelnitsky. Effects of electron-electron collisions with small energy transfers on quantum localisation. *Journal of Physics C: Solid State Physics*, 15(36):7367, 1982.

[34] T. Ando, A. B. Fowler, and F. Stern. Electronic properties of two-dimensional systems. *Rev. Mod. Phys.*, 54:437–672, 1982.

[35] M. J. Manfra. Molecular Beam Epitaxy of Ultra-High-Quality AlGaAs/GaAs Heterostructures: Enabling Physics in Low-Dimensional Electronic Systems. *Annual Review of Condensed Matter Physics*, 5(1):347–373, 2014.

[36] L. P. Kouwenhoven, C. M. Marcus, P. L. McEuen, S. Tarucha, R. M. Westervelt, and N. S. Wingreen. Electron Transport in Quantum Dots. In L. L. Sohn, L. P. Kouwenhoven, and G. Schön, editors, *Mesoscopic Electron Transport*, pages 105–214. Springer Netherlands, Dordrecht, 1997.

[37] H. van Houten and C. Beenakker. Quantum Point Contacts. *Physics Today*, 49(7):22–27, 1996.

[38] T. Heinzel. *Mesoscopic Electronics in Solid State Nanostructures*. John Wiley & Sons Ltd, Germany, 2006.

[39] D. Pines and P. Nozières. *The theory of quantum liquids. Vol.1, Normal Fermi liquids*. W.A. Benjamin, New York, 1966.

[40] A. A. Abrikosov, L. P. Gor'kov, and I. E. Dzyaloshinskii. *Methods of Quantum Field Theory in Statistical, Physics*. Pergamon Press, New York, 1965.

[41] A. F. Ioffe and A. R. Regel. Non-crystalline, amorphous, and liquid electronic semiconductors. *Progress in semiconductors*, 4:237–291, 1960.

[42] D. E. Khmel'nitskii. Localization and coherent scattering of electrons. *Physica B*, 126(1):235 – 241, 1984.

[43] J. Rammer. *Quantum Field Theory of Non-equilibrium States*. Cambridge University Press, Cambridge, 2007.

[44] H. Bruus and K. Flensberg. *Many-body quantum theory in condensed matter physics: an introduction*. Oxford graduate texts. Oxford University Press, Oxford, 2004.

[45] P. W. Anderson. Absence of Diffusion in Certain Random Lattices. *Phys. Rev.*, 109:1492–1505, 1958.

[46] E. Abrahams, P. W. Anderson, D. C. Licciardello, and T. V. Ramakrishnan. Scaling Theory of Localization: Absence of Quantum Diffusion in Two Dimensions. *Phys. Rev. Lett.*, 42:673–676, 1979.

[47] J. Cardy. *Scaling and Renormalization in Statistical Physics*. Cambridge Lecture Notes in Physics. Cambridge University Press, Cambridge, 1996.

[48] K. Slevin and T. Ohtsuki. Critical exponent for the Anderson transition in the three-dimensional orthogonal universality class. *New Journal of Physics*, 16(1):015012, 2014.

[49] N. F. Mott. Review Lecture: Metal-Insulator Transitions. *Proceedings of the Royal Society of London. Series A, Mathematical and Physical Sciences*, 382(1782):1–24, 1982.

[50] Y. Imry. Transport at low temperature in amorphous magnetic metals (invited). *Journal of Applied Physics*.

[51] Y. Imry and Z. Ovadyahu. Transition to a microscopic diffusion regime and dimensional crossover in a disordered conductor. *Journal of Physics C: Solid State Physics*, 15(11):L327, 1982.

[52] N. F. Mott. The mobility edge since 1967. *Journal of Physics C: Solid State Physics*, 20(21):3075, 1987.

[53] N. F. Mott. Conduction in non-crystalline systems. 1. Localized electronic states in disordered systems. *Philos. Mag.*, 17(150):1259, 1968.

[54] N. F. Mott and E. A. Davis. Conduction in non-crystalline systems. 2. Metal-insulator transition in a random array of centres. *Philos. Mag.*, 17(150):1269, 1968.

[55] N. F. Mott. Conduction in non-Crystalline systems. 4. Anderson localization in a disordered lattice. *The Philosophical Magazine: A Journal of Theoretical Experimental and Applied Physics*, 22(175):7–29, 1970.

[56] A. L. Efros and B. I. Shklovskii. Coulomb gap and low temperature conductivity of disordered systems. *Journal of Physics C: Solid State Physics*, 8(4):L49, 1975.

[57] L. Fleishman and P. W. Anderson. Interactions and the Anderson transition. *Phys. Rev. B*, 21:2366–2377, 1980.

[58] A. M. Finkel'shtein. Influence of Coulomb interaction on the properties of disordered metals. *Zh. Eksp. Teor. Fiz.*, 84:168, 1983. [*Sov. Phys. JETP*, 57(1):97, 1983].

[59] J. M. Deutsch. Quantum statistical mechanics in a closed system. *Phys. Rev. A*, 43:2046–2049, 1991.

[60] M. Srednicki. Chaos and quantum thermalization. *Phys. Rev. E*, 50:888–901, 1994.

[61] J. M Deutsch. Eigenstate thermalization hypothesis. *Reports on Progress in Physics*, 81(8):082001, 2018.

[62] L. D'Alessio, Y. Kafri, A. Polkovnikov, and M. Rigol. From quantum chaos and eigenstate thermalization to statistical mechanics and thermodynamics. *Advances in Physics*, 65(3):239–362, 2016.

[63] D. A. Huse, R. Nandkishore, and V. Oganesyan. Phenomenology of fully many-body-localized systems. *Phys. Rev. B*, 90:174202, 2014.

[64] M. Serbyn, Z. Papić, and D. A. Abanin. Local Conservation Laws and the Structure of the Many-Body Localized States. *Phys. Rev. Lett.*, 111:127201, 2013.

[65] M. Headrick. Lectures on entanglement entropy in field theory and holography. 2019. arXiv:1907.08126 [hep-th].

[66] M. Serbyn, Z. Papić, and D. A. Abanin. Universal Slow Growth of Entanglement in Interacting Strongly Disordered Systems. *Phys. Rev. Lett.*, 110:260601, 2013.

[67] F. Alet and N. Laflorencie. Many-body localization: An introduction and selected topics. *Comptes Rendus Physique*, 19(6):498–525, 2018.

[68] D. J. Luitz, N. Laflorencie, and F. Alet. Many-body localization edge in the random-field Heisenberg chain. *Phys. Rev. B*, 91:081103, 2015.

[69] W. De Roeck, F. Huveneers, M. Müller, and M. Schiulaz. Absence of many-body mobility edges. *Phys. Rev. B*, 93:014203, 2016.

[70] J. Z. Imbrie. On Many-Body Localization for Quantum Spin Chains. *Journal of Statistical Physics*, 163(5):998–1048, 2016.

[71] W. De Roeck and F. Huveneers. Stability and instability towards delocalization in many-body localization systems. *Phys. Rev. B*, 95:155129, 2017.

[72] A. Morningstar, L. Colmenarez, V. Khemani, D. J. Luitz, and D. A. Huse. Avalanches and many-body resonances in many-body localized systems. *Phys. Rev. B*, 105:174205, 2022.

[73] D. M. Long, P. J. D. Crowley, V. Khemani, and A. Chandran. Phenomenology of the Prethermal Many-Body Localized Regime. 2022. arXiv:2207.05761 [cond-mat.dis-nn].

[74] E. Altman and R. Vosk. Universal Dynamics and Renormalization in Many-Body-Localized Systems. *Annual Review of Condensed Matter Physics*, 6(1):383–409, 2015.

[75] R. Vosk, D. A. Huse, and E. Altman. Theory of the Many-Body Localization Transition in One-Dimensional Systems. *Phys. Rev. X*, 5:031032, 2015.

[76] A. C. Potter, R. Vasseur, and S. A. Parameswaran. Universal Properties of Many-Body Delocalization Transitions. *Phys. Rev. X*, 5:031033, 2015.

[77] K. Agarwal, S. Gopalakrishnan, M. Knap, M. Müller, and E. Demler. Anomalous Diffusion and Griffiths Effects Near the Many-Body Localization Transition. *Phys. Rev. Lett.*, 114:160401, 2015.

[78] R. K. Panda, A. Scardicchio, M. Schulz, S. R. Taylor, and M. Žnidarič. Can we study the many-body localisation transition? *Europhysics Letters*, 128(6):67003, feb 2020.

[79] M. Schreiber, S. S. Hodgman, P. Bordia, H. P. Lüschen, M. H. Fischer, R. Vosk, E. Altman, U. Schneider, and I. Bloch. Observation of many-body localization of interacting fermions in a quasirandom optical lattice. *Science*, 349(6250):842–845, 2015.

[80] H. P. Lüschen, P. Bordia, S. S. Hodgman, M. Schreiber, S. Sarkar, A. J. Daley, M. H. Fischer, E. Altman, I. Bloch, and U. Schneider. Signatures of Many-Body Localization in a Controlled Open Quantum System. *Phys. Rev. X*, 7:011034, 2017.

[81] J. Choi, S. Hild, J. Zeiher, P. Schauß, A. Rubio-Abadal, T. Yefsah, V. Khemani, D. A. Huse, I. Bloch, and C. Gross. Exploring the many-body localization transition in two dimensions. *Science*, 352(6293):1547–1552, 2016.

[82] A. Altland and B. D. Simons. *Condensed Matter Field Theory*. Cambridge University Press, Cambridge, 2nd edition, 2010.

[83] A. Kamenev. *Field Theory of Non-Equilibrium Systems*. Cambridge University Press, Cambridge, 2011.

[84] J. Rammer and H. Smith. Quantum field-theoretical methods in transport theory of metals. *Rev. Mod. Phys.*, 58:323–359, 1986.

[85] H. Haug and A.-P. Jauho. *Quantum kinetics in transport and optics of semiconductors*. Springer, Berlin, 1998.

[86] G. D. Mahan. *Many-particle physics*. Physics of solids and liquids. Kluwer Academic/Plenum Publishers, New York, 3rd edition, 2000.

[87] J. Schwinger. Brownian Motion of a Quantum Oscillator. *Journal of Mathematical Physics*, 2(3):407–432, 1961.

[88] L. V. Keldysh. Diagram technique for nonequilibrium processes. *Zh. Eksp. Teor. Fiz.*, 47:1515–1527, 1964. [*Sov. Phys. JETP*, 20(4):1018, 1965].

[89] A. I. Larkin and Yu. N. Ovchinnikov. Nonlinear conductivity of superconductors in the mixed state. *Zh. Eksp. Teor. Fiz.*, 68:1915, 1975. [*Sov. Phys. JETP*, 41(5):960, 1975].

[90] P. L. Gor'kov, A. Larkin, and D. E. Khmel'nitskii. Particle Conductivity in a Two-Dimensional Random Potential. *Pis'ma Zh. Eksp. Teor. Fiz.*, 30(4):248, 1979. [*JETP Lett.*, 30:228, 1979].

[91] G. Sambandamurthy, L. W. Engel, A. Johansson, E. Peled, and D. Shahar. Experimental Evidence for a Collective Insulating State in Two-Dimensional Superconductors. *Phys. Rev. Lett.*, 94:017003, 2005.

[92] F. Ladieu, M. Sanquer, and J. P. Bouchaud. Depinning transition in Mott-Anderson insulators. *Phys. Rev. B*, 53:973–976, 1996.

[93] V. M. Vinokur, T. I. Baturina, M. V. Fistul, A. Yu. Mironov, M. R. Baklanov, and C. Strunk. Superinsulator and quantum synchronization. *Nature*, 452(7187):613–615, 2008.

[94] T. Levinson, A. Doron, I. Tamir, G. C. Tewari, and D. Shahar. Direct determination of the temperature of overheated electrons in an insulator. *Phys. Rev. B*, 94:174204, 2016.

[95] A. Doron, I. Tamir, T. Levinson, M. Ovadia, B. Sacépé, and D. Shahar. Instability of Insulators near Quantum Phase Transitions. *Phys. Rev. Lett.*, 119:247001, 2017.

[96] T. I. Baturina, A. Yu. Mironov, V. M. Vinokur, M. R. Baklanov, and C. Strunk. Localized Superconductivity in the Quantum-Critical Region of the Disorder-Driven Superconductor-Insulator Transition in TiN Thin Films. *Phys. Rev. Lett.*, 99:257003, 2007.

[97] M. Ovadia, B. Sacépé, and D. Shahar. Electron-Phonon Decoupling in Disordered Insulators. *Phys. Rev. Lett.*, 102:176802, 2009.

[98] M. V. Fistul, V. M. Vinokur, and T. I. Baturina. Collective Cooper-Pair Transport in the Insulating State of Josephson-Junction Arrays. *Phys. Rev. Lett.*, 100:086805, 2008.

[99] K. B. Efetov, M. V. Feigel'man, and P. B. Wiegmann. Comment on "Superinsulator and Quantum Synchronization". 2008. arXiv:0804.3775 [cond-mat.supr-con].

[100] K. B. Efetov, M. V. Feigel'man, and P. B. Wiegmann. Comment on "Collective Cooper-Pair Transport in the Insulating State of Josephson-Junction Arrays". *Phys. Rev. Lett.*, 102:049701, 2009.

[101] B. L. Altshuler, V. E. Kravtsov, I. V. Lerner, and I. L. Aleiner. Jumps in Current-Voltage Characteristics in Disordered Films. *Phys. Rev. Lett.*, 102:176803, 2009.

[102] V. I. Yudson and V. E. Kravtsov. Electron kinetics in isolated mesoscopic rings driven out of equilibrium. *Phys. Rev. B*, 67:155310, 2003.

[103] M. Y. Reizer and A. V. Sergeev. Electron-phonon interaction in impure metals and superconductors. *Zh. Eksp. Teor. Fiz.*, 90(3):1056, 1986. [*Sov. Phys. JETP*, 63(3):616, 1986].

[104] A. Sergeev and V. Mitin. Electron-phonon interaction in disordered conductors: Static and vibrating scattering potentials. *Phys. Rev. B*, 61:6041–6047, 2000.

[105] E. Cuevas and V. E. Kravtsov. Two-eigenfunction correlation in a multifractal metal and insulator. *Phys. Rev. B*, 76:235119, 2007.

[106] M. V. Feigel'man and V. E. Kravtsov. Electron-phonon cooling power in Anderson insulators. *Phys. Rev. B*, 99:125415, 2019.

[107] S. Kasirer and Y. Meir. Hysteresis and jumps in the $I-V$ curves of disordered two-dimensional materials. *Phys. Rev. B*, 105:134508, 2022.

[108] M. Ovadia, D. Kalok, I. Tamir, S. Mitra, B. Sacépé, and D. Shahar. Evidence for a Finite-Temperature Insulator. *Scientific Reports*, 5(1):13503, 2015.

[109] I. Tamir, T. Levinson, F. Gorniaczyk, A. Doron, J. Lieb, and D. Shahar. Excessive noise as a test for many-body localization. *Phys. Rev. B*, 99:035135, 2019.

[110] A. Haug and D. Shahar. Excess noise in the anomalous metallic phase in amorphous indium oxide. 2023. arXiv:2305.15931 [cond-mat.supr-con].

[111] J. M. Ziman. *Principles of the Theory of Solids*. Cambridge University Press, Cambridge, 2nd edition, 1972.

[112] N. G. Ptitsina, G. M. Chulkova, K. S. Il'in, A. V. Sergeev, F. S. Pochinkov, E. M. Gershenzon, and M. E. Gershenson. Electron-phonon interaction in disordered metal films: The resistivity and electron dephasing rate. *Phys. Rev. B*, 56:10089–10096, 1997.

[113] Y. Gul, S. N. Holmes, C. Cho, B. Piot, M. Myronov, and M. Pepper. Two-dimensional localization in GeSn. *Journal of Physics: Condensed Matter*, 34(48):485301, 2022.

[114] G. Auton. (Private communication), 2023.

[115] Y. Alhassid. The statistical theory of quantum dots. *Rev. Mod. Phys.*, 72:895–968, 2000.

[116] I. L. Kurland, I. L. Aleiner, and B. L. Altshuler. Mesoscopic magnetization fluctuations for metallic grains close to the Stoner instability. *Phys. Rev. B*, 62:14886–14897, 2000.

[117] I. O. Kulik and R. I. Shekhter. Kinetic phenomena and charge discreteness effects in granulated media. *Zh. Eksp. Teor. Fiz.*, 68:623, 1975. [*Sov. Phys. JETP*, 41(2):308, 1975].

[118] C. W. J. Beenakker. Theory of Coulomb-blockade oscillations in the conductance of a quantum dot. *Phys. Rev. B*, 44:1646–1656, 1991.

[119] D. V. Averin and K. K. Likharev. Coulomb blockade of single-electron tunneling, and coherent oscillations in small tunnel junctions. *Journal of Low Temperature Physics*, 62(3):345–373, 1986.

[120] Y. Nagamune, H. Sakaki, L. P. Kouwenhoven, L. C. Mur, C. J. P. M. Harmans, J. Motohisa, and H. Noge. Single electron transport and current quantization in a novel quantum dot structure. *Applied Physics Letters*, 64(18):2379–2381, 1994.

[121] M. Amman, R. Wilkins, E. Ben-Jacob, P. D. Maker, and R. C. Jaklevic. Analytic solution for the current-voltage characteristic of two mesoscopic tunnel junctions coupled in series. *Phys. Rev. B*, 43:1146–1149, 1991.

[122] U. Sivan, Y. Imry, and A. G. Aronov. Quasi-particle lifetime in a quantum dot. *Europhys. Lett.*, 28(2):115–120, 1994.

[123] Ya. M. Blanter. Electron-electron scattering rate in disordered mesoscopic systems. *Phys. Rev. B*, 54:12807–12819, 1996.

[124] N. Macé, F. Alet, and N. Laflorencie. Multifractal Scalings Across the Many-Body Localization Transition. *Phys. Rev. Lett.*, 123:180601, 2019.

[125] M. Pino, L. B. Ioffe, and B. L. Altshuler. Nonergodic metallic and insulating phases of Josephson junction chains. *Proceedings of the National Academy of Sciences*, 113(3):536–541, 2016.

[126] M. Pino, V. E. Kravtsov, B. L. Altshuler, and L. B. Ioffe. Multifractal metal in a disordered Josephson junctions array. *Phys. Rev. B*, 96:214205, 2017.

[127] E. J. Torres-Herrera and L. F. Santos. Extended nonergodic states in disordered many-body quantum systems. *Annalen der Physik*, 529(7):1600284, 2017.

[128] P. Jacquod and D. L. Shepelyansky. Emergence of Quantum Chaos in Finite Interacting Fermi Systems. *Phys. Rev. Lett.*, 79:1837–1840, 1997.

[129] A. D. Mirlin and Y. V. Fyodorov. Localization and fluctuations of local spectral density on treelike structures with large connectivity: Application to the quasiparticle line shape in quantum dots. *Phys. Rev. B*, 56:13393–13404, 1997.

[130] I. V. Gornyi, A. D. Mirlin, and D. G. Polyakov. Many-body delocalization transition and relaxation in a quantum dot. *Phys. Rev. B*, 93:125419, 2016.

[131] Y. V. Nazarov and Ya. M. Blanter. *Quantum Transport: Introduction to Nanoscience*. Cambridge University Press, Cambridge, 2009.

[132] D. V. Averin and A. N. Korotkov. Influence of discrete energy spectrum on correlated single-electron tunneling via a mezoscopically small metal granule. *Zh. Eksp. Teor. Fiz.*, 97:1661–1673, 1990. [*Sov. Phys. JETP*, 70(5):937, 1990].

[133] N. Sedlmayr, I. V. Yurkevich, and I. V. Lerner. Tunnelling density of states at Coulomb-blockade peaks. *Europhys. Lett.*, 76(1):109–114, 2006.

[134] T. Phoenix. Noise and the full counting statistics of a coulomb blockaded quantum dot, PhD Thesis, 2010.

[135] D. M. Larsson. Noise in coulomb blockaded quantum dots and kondo systems, PhD Thesis, 2010.

[136] A.-P. Jauho, N. S. Wingreen, and Y. Meir. Time-dependent transport in interacting and noninteracting resonant-tunneling systems. *Phys. Rev. B*, 50:5528–5544, 1994.

[137] H. Pothier, S. Guéron, Norman O. Birge, D. Esteve, and M. H. Devoret. Energy distribution function of quasiparticles in mesoscopic wires. *Phys. Rev. Lett.*, 79:3490–3493, 1997.

[138] M. J. M. de Jong and C. W. J. Beenakker. *Shot Noise in Mesoscopic Systems*, pages 225–258. Springer Netherlands, Dordrecht, 1997.

[139] C. Beenakker and C. Schönenberger. Quantum Shot Noise. *Physics Today*, 56(5):37–42, 2003.

[140] R. Landauer. Mesoscopic noise: Common sense view. *Physica B: Condensed Matter*, 227(1):156–160, 1996. Proceedings of the Third International Symposium on New Phenomena in Mesoscopic Structures.

[141] Ya. M. Blanter and M. Büttiker. Shot noise in mesoscopic conductors. *Physics Reports*, 336(1):1–166, 2000.

[142] S. Feng, P. A. Lee, and A. D. Stone. Sensitivity of the Conductance of a Disordered Metal to the Motion of a Single Atom: Implications for $\frac{1}{f}$ Noise. *Phys. Rev. Lett.*, 56:1960–1963, 1986.

[143] L. S. Levitov and M. Reznikov. Counting statistics of tunneling current. *Phys. Rev. B*, 70:115305, 2004.

[144] O. Agam, N. S. Wingreen, B. L. Altshuler, D. C. Ralph, and M. Tinkham. Chaos, Interactions, and Nonequilibrium Effects in the Tunneling Resonance Spectra of Ultrasmall Metallic Particles. *Phys. Rev. Lett.*, 78:1956–1959, 1997.

[145] Z. Lenarčič, E. Altman, and A. Rosch. Activating Many-Body Localization in Solids by Driving with Light. *Phys. Rev. Lett.*, 121:267603, 2018.

[146] Y. Meir and N. S. Wingreen. Landauer formula for the current through an interacting electron region. *Phys. Rev. Lett.*, 68:2512–2515, 1992.